Diploma Thesis

An Atom-Ion Quantum Gate

Universität Ulm
Fakultät für Naturwissenschaften
Institut für Quanteninformationsverarbeitung
Hauke Doerk-Bendig, hauke.do.b@gmail.com, 2008

Supervisor/Referee:	Prof. Dr. Tommaso Calarco, Universität Ulm
Co-Supervisor:	Dr. Zbigniew Idziaszek, Universität Warschau
Referee:	apl. Prof. Dr. Reinhold Walser, Universität Ulm

Eidesstattliche Erklärung

Hiermit versichere ich, die vorliegende Arbeit selbständig, ohne fremde Hilfe und ohne Benutzung anderer als der von mir angegebenen Quellen angefertigt zu haben. Die Arbeit wurde noch keiner Prüfungsbehörde in gleicher oder ähnlicher Form vorgelegt.

Hauke Doerk-Bendig (Matrikelnummer 515594), 13. November 2008

Abstract

Quantum information processing with ultracold neutral atoms is quite promising, due to the long decoherence times, and the ability to precisely prepare them in the Mott insulator phase of an optical lattice. Ultracold ions, prepared in the ground state of a trapping potential, can be individually addressed with lasers and, because of tight trapping potentials, can be rapidly transported. In accordance with ongoing experiments we propose to unite atoms and ions in one setup to combine their advantages. A possible setup for quantum computation consists of a register of atom-qubits stored in an optical lattice with a movable ion carrying information and creating long distance entanglement between the atoms. The basic ingredient for this scheme is the ability to perform controlled atom-ion interaction in traps. We investigate the controlled collisions between a single trapped atom and a single trapped ion.

We model the atom-ion interaction by the long-range $1/r^4$ polarization potential combined with a quantum-defect parameter as a boundary condition at the origin. The quantum-defect parameter represents the phase accumulated by the wavefunction at small distances. The essential parameters for the quantum-defect theory are the singlet and triplet scattering lengths. These quantities are not yet known but can in principle be measured in upcoming experiments. Typical cases are discussed in this thesis. In general a Multichannel Quantum-Defect Theory (MQDT) is needed for describing the system. For specific scattering lengths we formulate an effective single channel model.

The goal of this work is to realize a two-qubit phase gate and therefore provide the basic ingredient of quantum computation for the system under consideration. For one realistic combination of singlet and triplet scattering length an adiabatic quantum gate process is calculated numerically. This process is optimized and accelerated with the help of optimal control techniques.

Danksagung

Ich danke meinen Betreuern Tommaso Calarco und Zbigniew Idziaszek dafür, dass sie meine Diplomarbeit und auch Reisen nach Warschau und Innsbruck ermöglicht haben. Viele wichtige Ideen sind im Gespräch mit den beiden entstanden.

Danken möchte ich auch Michael Murphy, Simone Montagero, Max Hettrich und Jens Baltrusch dafür, dass sie mir geholfen haben, meine Texte in verständlichere Sprache zu verwandeln. Meinen Kollegen im Institut danke ich dafür, dass sie so nette Kollegen sind und allen anderen Beteiligten danke ich für ihre freundliche Hilfe.

Bei meinen Eltern möchte ich mich für die finanzielle Unterstützung während des Studiums bedanken.

Ganz besonderer Dank gilt meiner Frau Marion Bendig. Sie hat mich in den letzten, arbeitsreichen Monaten nicht nur bei der Strukturierung und Formulierung der Arbeit, sondern auch moralisch unterstützt, und vor allem ertragen.

Contents

List of Figures

List of Tables

1 Introduction

During the last few decades, techniques were developed that allow preparation and manipulation of single ultracold atoms and ions in the laboratory. Single atoms are stored and laser-cooled in dipole traps [1]. Arrays of atoms can be prepared in optical lattices [2] in a Mott insulator phase and evaporative cooling is used to reach the vibrational ground state. Similar techniques are being pursued in the context of atom chips [3, 4]. External electromagnetic fields can be used to control the atomic two-particle interaction. Magnetic fields are widely used in the context of Feshbach resonances, that allow to manipulate the interaction strength. Pure electric fields are interesting for experiments, since they are already available in most of the mentioned setups. Single ions and arrays of ions can be confined in Paul or Penning traps [5] and sideband laser cooling allows to prepare them in the ground state of these trapping potentials. The coulomb potential prevents ions from approaching each other, so that interaction of ions must take place via an auxiliary collective mode.

Ultracold ions as well as neutral atoms confined in traps and controlled by lasers and external fields allow studies of fundamental aspects of quantum mechanics, but they are promising for applications such as quantum information as well. A combination of ultracold ions and atoms in one setup is currently being explored [6, 7]. Theoretical studies on the interaction properties as well as ongoing experiments open up this new field of research. Atom and ion trapping potentials, although both consisting of electromagnetic fields, do not interfere, since the frequencies typically differ by orders of magnitude.

Atom and ion can be of the same or of different species; one speaks of homonuclear and heteronuclear collisions, respectively. Both have advantages in different respects. One loss mechanism for the heteronuclear atom-ion collision is the radiative charge transfer in which the ion's charge is transferred to the atom and

thereby a photon is emitted. Both particles are lost in this process. In homonuclear systems, the charge transfer leads to a physically equivalent situation and therefore it is not a loss mechanism. A heteronuclear alkali atom plus alkaline earth ion system has the advantage that the level structure is less complicated, since only the two outer electrons are relevant. Examples used in experiment are the homonuclear Yb^+ - Yb system [8] and the heteronuclear Ba^+ Rb system [9].

The combination of ultracold neutral atoms and ions in one experiment on the one hand leads to new insights on the quantum mechanical properties of atom-ion interaction. E.g. trap-induced shape resonances between unbound trap states and molecular states can be observed when changing the distance between atom and ion trap under the precondition that atom and ion are ultracold and close to the trap vibrational ground state [10]. These trap-induced resonances enhance and influence the interaction and can be seen as an alternative to Feshbach resonances. Ideas of sympathetically cooling trapped atoms by a laser-cooled trapped ion or of cooling trapped ions by ultracold atoms exist [11, 12, 13].

On the other hand, in the context of quantum information one can combine the advantages of atoms and ions. Good addressability of single trapped ions with lasers and fast transport due to tight Paul traps are some of the advantages of ions. The possibility to prepare an array of atoms in the Mott insulator phase in an optical lattice is a reason to use atoms as a storage of quantum information. Furthermore, the two-particle interaction of atom and ion is stronger than for two neutral atoms, which allows faster gate operations.

Qubits can be stored in internal degrees of freedom (hyperfine states), and the two particle interaction is made qubit dependent with the help of Feshbach or trap-induced resonances. Single qubit operations on hyperfine states can be performed with laser driven Raman transitions (see e.g. [14, 15]).

The present work deals with heteronuclear atom-ion collisions. The existing multichannel quantum-defect theory for the free ultracold collision of an alkali atom and an alkaline earth ion [7] is specialized to the case of trapping potentials. The central aspect of this thesis is the application of the ultracold controlled atom-ion collision to quantum information processing.

A possible setup for quantum computation is schematically depicted in Fig-

ure 1.1. Atoms are stored in an optical lattice in a Mott insulator phase such that each lattice site is occupied by exactly one atom. One movable ion can be used to entangle the atoms and perform quantum gates. It is also possible to leave one site unoccupied between two atoms in the lattice to enhance the addressability of the atoms with the ion. The basic ingredient of this idea is the controlled and qubit sensitive interaction of a single atom with a single ion. The goal of this thesis is to find a way of realizing a two-qubit phase gate of an atom and an ion. Being equivalent to the CNOT gate, the phase gate is a universal gate for quantum algorithms [16]. Trap-induced shape resonances are used to enhance the interaction; no magnetic field is included in the present approach [1]. This thesis

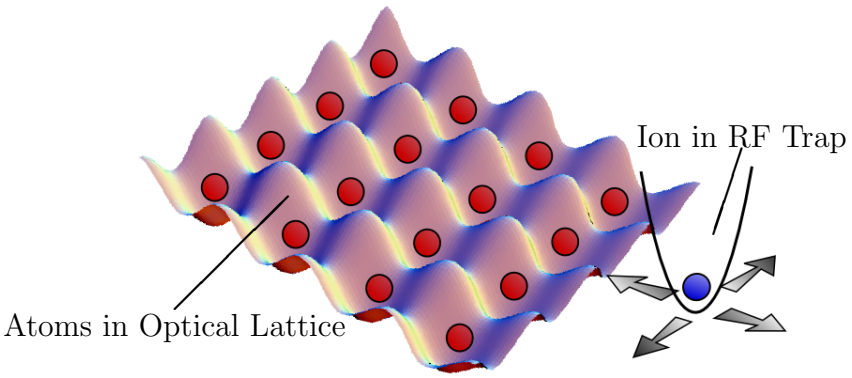

Figure 1.1: Concept for quantum computation with atoms and ions: Atoms are prepared in an optical lattice in Mott insulator phase. A movable ion entangles the atoms and can also be used for sympathetic cooling.

is organized as follows. Chapter 2 introduces important terminology and the encoding of qubits into hyperfine states. Further the basic model for the collision as well as the atom-ion interaction are explained. Chapter 3 describes the formalism of multichannel quantum-defect theory for trapped atom ion collision. A single channel effective model is derived and the numerical solution of the time indepen-

[1] The combination of trap-induced resonances and Feshbach resonances is expected to allow more precise control of the system and will be a subject of future investigations.

dent single channel Schrödinger equation is discussed. The essential parameters to characterize the interaction are the singlet and triplet scattering lengths. They are not yet experimentally accessible and are difficult to calculate *ab initio*. After formulating the general theory, we choose specific isotopes for atom and ion and assume realistic singlet and triplet scattering lengths. These are used in further numerical calculations. Important features of the controlled collision in the considered atom-ion system are discussed in Chapter 4. Finally, Chapter 5 presents the explicit numerical simulation of a two-qubit phase gate using a $^{135}Ba^{+}$ ion and a ^{87}Rb atom. An adiabatic gate process is shown and this process is optimized with the help of optimal control techniques. Chapter 6 summarizes the results and gives an outlook.

In the Appendix A we explain the used numerical algorithms. These are the Numerov method for solving the time independent Schrödinger equation and the Crank-Nicholson method for time evolution. Appendix B explains the optimal control algorithm used for the gate process.

2 Quantum Computing with Atom-Ion Collision

This diploma thesis builds on the investigations of controlled atom-ion collision in [10]. The goal is the application of the relatively strong atom-ion interaction for quantum information, especially to realize a two-qubit phase gate with a single atom and a single ion. This work makes use of several simplifications and assumptions that reduce the complexity of the calculations. In doing so the principle of an atom-ion quantum gate can be demonstrated. Because we have to assume typical singlet and triplet scattering lengths, the calculated numerical values may not describe a real physical system. The calculations performed serve as an example of how to solve the system dynamics, once the correct parameters are known.

2.1 Model for Trapped Atom-Ion Collision

As a first approach to controlled atom-ion collisions we consider a single atom and a single ion. Both are guided by effective trapping potentials. The trap for the atom could be realized with optical tweezers or optical lattices [1, 2]. The ion could be trapped in a Paul trap using radio-frequency (RF) electric fields [5]. Atom and ion are assumed to be cooled to the vibrational ground state and therefore harmonic traps provide a good approximation to the real trapping potential.[1] The controlled collision of an atom and an ion guided by movable trapping potentials is illustrated in Figure 2.1. The effective Hamiltonian of the system is composed of the kinetic energy terms $\mathbf{p}_\nu/2m_\nu$ for $\nu = i$ (ion) and $\nu = a$ (atom) and the harmonic trapping potentials $\frac{1}{2}m_\nu\omega_\nu^2(\mathbf{r}_\nu - \mathbf{d}_\nu)^2$ centered at $\mathbf{d}_\nu$, and the atom-ion

[1] Future work will have to deal with anharmonicities and other effects like micromotion.

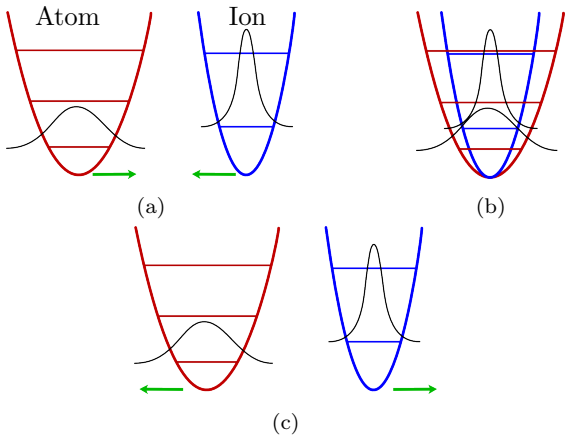

Figure 2.1: Schematic drawing of the controlled collision of a single atom and a single ion, whose center-of-mass wavepackets are guided by time dependent traps. Different phases of the process are shown: (a) initially the atom and the ion are prepared in the vibrational ground state; (b) collision (overlap of the wavepackets); (c) after trap separation, the goal is to obtain the atom and the ion in their vibrational ground state again.

interaction potential $V(r)$.

$$H = \frac{\mathbf{p}_i^2}{2m_i} + \frac{\mathbf{p}_a^2}{2m_a} + \frac{1}{2}m_i\omega_i^2(\mathbf{r}_i - \mathbf{d}_i)^2 + \frac{1}{2}m_a\omega_a^2(\mathbf{r}_a - \mathbf{d}_a)^2 + V(|\mathbf{r}_i - \mathbf{r}_a|). \quad (2.1)$$

Different trap geometries can be considered. In the laboratory, atomic traps (e.g. optical lattices) can be made spherically symmetric. Ion traps are usually cigar shaped, but in principle can also be built spherically symmetric. In this work we assume spherically symmetric traps for both atom and ion. The trapping frequencies are set to be equal, i.e. $\omega_i = \omega_a = \omega$, so that relative motion decouples from center-of-mass motion. Thereby the dimension of the problem is reduced from six to three. This is not the most general choice, but it captures the most important features of the system [2].

We introduce relative coordinates $\mathbf{r} = \mathbf{r}_i - \mathbf{r}_a$ and $\mathbf{R}_{\mathrm{COM}} = (m_i\mathbf{r}_i + m_a\mathbf{r}_a)/(m_i + m_a)$. For simplicity, we choose the coordinate frame such that the vector of trap

[2] Different geometries like cigar shaped traps will be a subject of future work.

separation $\mathbf{d} = \mathbf{d}_i - \mathbf{d}_a = d\,\mathbf{e}_z$ points in the z direction. In conclusion the relative Hamiltonian takes the form

$$H_{\mathrm{rel}}^{(d)} = -\frac{\hbar^2}{2\mu}\Delta_r + \frac{1}{2}\mu\omega^2(x^2+y^2) + \frac{1}{2}\mu\omega^2(z-d)^2 + V(r), \tag{2.2}$$

where $\mu = m_i m_a/(m_i + m_a)$ is the reduced mass of the atom-ion system and the momentum operator $\mathbf{p} = -i\hbar\nabla_r$ is substituted. The Laplace operator $\Delta = \nabla_r^2$ is introduced. It is useful to remark that the Hamiltonian can be written as $H_{\mathrm{rel}}^{(0)}$ for $d = 0$ plus some extra terms containing the dependence on d:

$$H_{\mathrm{rel}}^{(d)} = H_{\mathrm{rel}}^{(0)} + \frac{1}{2}\mu\omega^2 d^2 - \mu\omega^2\, d\, z. \tag{2.3}$$

2.2 Atom-Ion Interaction

The attraction or repulsion of two atoms (or an atom and an ion) can be described by an effective potential that depends on the relative distance of the atomic cores. The potential for the interaction between an ion and an atom can be understood in the following way. The ion charge polarizes the electron cloud of the atom and the induced dipole and the charge then attract each other.

The Born-Oppenheimer approximation allows to separate the motion of the electrons from the motion of the atom cores, since the electrons move on a much faster time scale. Assuming that the core distance is fixed, the potential energy is obtained by solving the time independent Schrödinger equation for all electrons in the system. This procedure can be repeated for all core distances and the resulting energy curve is called a Born-Oppenheimer potential. Figure 2.2 schematically shows the corresponding effective potential.

With the help of perturbation theory one can find that the long range part of this potential for atom and ion in their electronic ground state is proportional to $-1/r^4$:

$$\lim_{r\to\infty} V(r) = -\frac{C_4}{r^4}. \tag{2.4}$$

The interaction constant $C_4 = \alpha_{\mathrm{pol}} e^2/2$ is proportional to the electric dipole polarizability α_{pol} of the atom in the electronic ground state (S-state). The $1/r^4$ law is only valid if the the atom is in an S-state. As soon as excited electronic states

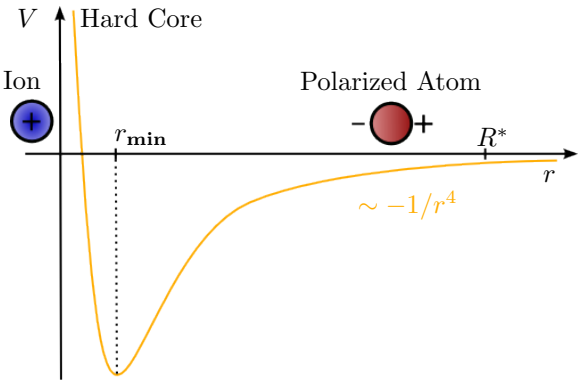

Figure 2.2: Schematic depiction of the atom-ion polarization potential with a hard core at $r = 0$ and the long range $\sim 1/r^4$ part. No trapping potential is drawn, so in the limit of $r \to \infty$ the potential approaches the molecular dissociation energy threshold. The characteristic range of the interaction is given by R^* (see text for details). r_{min} denotes the location of the potential minimum.

(P, D,...) are populated, the Born-Oppenheimer potential substantially changes its shape, because permanent higher order electric moments play a role.
One can define a characteristic length scale R^* of the polarization potential by equating the potential to the kinetic energy:

$$\frac{\hbar^2}{2\mu(R^*)^2} = \frac{C_4}{(R^*)^4} \qquad \Rightarrow \qquad R^* = \sqrt{\frac{2C_4}{\hbar^2}}, \tag{2.5}$$

where μ is the reduced mass of the two-body system. R^* can be interpreted as the range of the potential. A characteristic energy scale

$$E^* = \frac{\hbar^2}{2\mu(R^*)^2} \tag{2.6}$$

can also be defined. This energy defines the height of the centrifugal barrier for $l = 1$ (see e.g. Equation (3.5) and Figure 3.1). For particles of relative kinetic

energy much smaller than E^*, only the part of the incoming wavefunction corresponding to $l = 0$ (S-wave) is affected by the interaction, because for components corresponding to higher l the interaction potential is screened by the centrifugal barrier. Example values of characteristic energies for different atom-ion combinations are given in Table 2.1.

2.2.1 Pseudopotential Approximation

The pseudopotential approximation includes all scattering information in a single parameter: the s-wave scattering length a_s. Effectively, the complicated scattering potential $V(r)$ is replaced by a δ-function

$$V(r) \to V_0 \delta(r), \tag{2.7}$$

where $V_0 \sim a_s$. The pseudopotential approximation very much simplifies the integration of Schrödinger's equation. In neutral atom collisions the pseudopotential model has been applied very effectively. In traps like optical lattices, the effective description of the interaction by the scattering length enters the Bose-Hubbard model [17, 2].

However, the pseudopotential description can only be valid if the range of the potential is very short in comparison to other relevant length scales, so that the interaction can be described by a δ-function. In harmonic traps, this scale is given by the oscillator length $l_\nu = \sqrt{\hbar/\omega_\nu m_\nu}$ of the trapped particles, with $\nu = i, a$. Neutral atoms interact on short range, with a van der Waals-like interaction potential $V_{\text{neutral}} \sim 1/r^6$, and the range of the neutral atom potential is very small in comparison to typical trap scales. In contrast the range of the atom-ion $1/r^4$ potential can be comparable to or even larger than the trap scale. Therefore, assuming typical trapping frequencies of 10 to 100kHz the pseudopotential is not applicable in atom-ion collisions. Characteristic scales for different atom-ion combinations are given in Table 2.1. Only in the special situation of a small interaction constant C_4 combined with weak traps can the range R^* be much smaller than the harmonic oscillator length, so that a pseudopotential description can be applied. A small C_4 is obtained for small atom polarizability and light particles, and a weak trap has a small trapping frequency ω. As a criterion we introduce a dimensionless

Atom-Ion System	$R^*(a_0)$	$l_0(a_0)$	$E^*(\mu\mathrm{K})$
$^{135}\mathrm{Ba}^+ + {}^{87}\mathrm{Rb}$	5544	826	0,0533
$^{40}\mathrm{Ca}^+ + {}^{87}\mathrm{Rb}$	3989	1178	0,198
$^{40}\mathrm{Ca}^+ + {}^{23}\mathrm{Na}$	2081	1572	1,37

Table 2.1: Characteristic length and energy scale for example systems. Oscillator lengths are calculated with $\omega = 2\pi \times 100\mathrm{kHz}$.

parameter

$$\alpha = \left(\frac{R^*}{l_0}\right)^4 = \left(\frac{\hbar\omega}{2E^*}\right)^2 \tag{2.8}$$

that compares the characteristic range of the potential to the trap scale, and which can also be obtained by comparing the oscillator ground state energy to the characteristic energy of atom-ion interaction. The parameter α depends on the mass μ of the colliding particles and the trapping frequency ω that is assumed to be the same for both particles. The relative harmonic oscillator length is $l_0 = \sqrt{\hbar/\mu\omega}$. In the case of weak traps and weak interaction, α is small and for $\alpha \ll 1$ a pseudopotential approximation is applicable. Under these circumstances, the Schrödinger equation can be solved analytically, which can help in understanding certain aspects of the system (see [18]).

Weak interactions and weak traps are, however, not interesting for quantum information, because gates would be slow. Fast gates require strong interaction and tight traps. In this case α is big ($\alpha \gg 1$), because the interaction range is comparable or larger than the trap scale. Since the pseudopotential approximation does not hold in this case, one has to include the explicit shape of the interaction potential and solve Schrödinger's equation numerically. In this thesis, a multichannel quantum-defect theory is used for this purpose.

2.3 Basics of the Physics of Atomic Collisions

For a better understanding of the following sections a basic introduction to the physics of cold collisions is given here. In particular the term 'scattering channel' is explained, since it is used throughout this thesis.

Name	Notation	Definition
Interaction constant	C_4	$\alpha_{\mathrm{pol}} e^2/2$
Characteristic range of the polarization potential	R^*	$\sqrt{2C_4/\hbar^2}$
Characteristic Energy of the polarization potential	E^*	$\hbar^2/(2\mu(R^*)^2)$
Relative oscillator length	l_0	$\sqrt{\hbar/\mu\omega}$
Parameter of atom-ion collision in traps	α	$(R^*/l_0)^4 = (\hbar\omega/(2E^*))^2$

Table 2.2: Terminology of constants and parameters used throughout this thesis.

For two colliding particles the time independent Schrödinger equation

$$\left(\frac{p_1^2}{2m_1} + \frac{p_2^2}{2m_2} + V(r_1, r_2)\right) \Psi_{12}(r_1, r_2) = E\Psi_{12}(r_1, r_2) \tag{2.9}$$

with the scattering potential V is studied. In general collision problems the potential only depends on the relative distance of the colliding particles $r = r_1 - r_2$, so that $V \equiv V(r)$. The collision of two charged particles is described by the Coulomb potential $V(r) = q_1 q_2/r$, for example.

The properties of the collision of two atoms strongly depends on the spin states of the colliding particles. In the following we specify to the collision of hydrogen like atoms that only have one unpaired electron. The state of the atoms is then determined by the angular momenta of the two nuclei and of the two outer electrons. We assume that both electrons are in an S-state in which the orbital angular momentum of the electrons vanish; then their angular momenta are solely determined by their spin. Now the nuclei approach each other. The Pauli exclusion principle states that, if the electron spins are in a symmetric state (triplet configuration) it is not allowed that both electrons occupy the ground state. That means that one electron must be excited. This leads to repulsion, because the excitation of one electron costs energy. However, in an antisymmetric (singlet) spin configuration, both electrons can remain in the ground state, which results in a different interaction between the atoms. At small distances between the nuclei, one has to include the full electron cloud in the calculation in order to predict the

values of singlet and triplet scattering properties. The collision potential strongly depends on the symmetry of the electron spin configuration at small distances.

It is convenient to describe the quantum state of the incoming particles in the basis of hyperfine states. Hyperfine states are characterized by the total angular momentum $\mathbf{f}_\nu = \mathbf{i}_\nu + \mathbf{s}_\nu$ and its projection m_{f_ν} for particle $\nu \in \{1, 2\}$, where $\mathbf{i}_\nu$ denotes the nuclear spin and $\mathbf{s}_\nu$ is the electron spin. The hyperfine basis is often called the asymptotic basis, since it diagonalizes the Hamiltonian of the scattering particles at large distances ($r \to \infty$) where the interaction potential is negligible. In the ultracold regime the hyperfine splitting is much larger than the kinetic energy of the particles. Taking into account the angular momentum l of relative motion and its projection m_l, the full set of quantum numbers describing the incoming state $\beta = \{f_1, m_{f_1}, f_2, m_{f_2}, l, m_l\}$ is called a scattering channel.

At short distance the eigenstates of the system are not given by the asymptotic channels, since the electron clouds overlap and electronic interaction dominates the hyperfine energies. The spin eigenbasis at small distances is called the *is* basis. It is characterized by the total nuclear spin $\mathbf{i} = \mathbf{i}_1 + \mathbf{i}_2$ and the total electron spin $\mathbf{s} = \mathbf{s}_1 + \mathbf{s}_2$, where $\mathbf{s}$ can take the values 0 and 1, corresponding to singlet and triplet states respectively. Additionally this basis is characterized by the total angular momentum $\mathbf{f} = \mathbf{f}_1 + \mathbf{f}_2$, its projection m_f on the axis of quantization, and the angular momentum $\mathbf{l}$ of relative motion and its projection m_l. The full set of quantum numbers describing a channel in *is* representation is then $\gamma = \{f_1, m_{f_1}, f_2, m_{f_2}, l, m_l\}$. A unitary transformation between the two representation is called frame transformation and will be used in Section 3.2.2.

Figure 2.3 schematically shows potential curves for the collision of an $i = 3/2$ alkali atom with an $i = 3/2$ alkaline earth ion for the $m_{f_1} + m_{f_2} = 3$ subspace. On large distances the potential curves are associated to the hyperfine basis states, whereas at small distances the potential curves are associated to the *is* basis. A hyperfine state β can be written as a linear combination of *is* states. This linear combination is different for each hyperfine state and therefore the scattering properties depend on the incoming channel. The dissociation energy (the potential value for $r \to \infty$) is determined by the hyperfine energy of the channel. The long range behavior of the potential is the same for all channels: $\sim 1/r^6$ for neutral

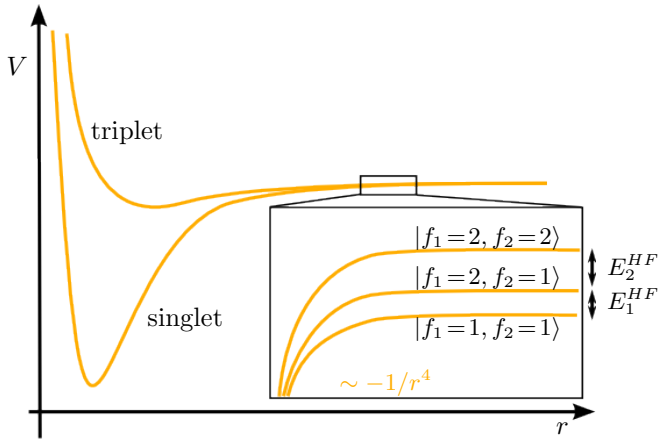

Figure 2.3: Schematic depiction of scattering potentials for the collision of an $i_1 = 3/2$ alkali atom with an $i_2 = 3/2$ alkaline earth ion. At small distances the potentials can be associated to singlet and triplet spin configuration. The eigenbasis is the *is* basis. At large distances the curves are associated to the hyperfine basis. The zoom shows the hyperfine splitting and the asymptotic $\sim -1/r^4$ behavior of the curves. For clarity, the state $|f_1=1, f_2=2\rangle$ is omitted, since the potential curve nearly is the same as for the $|f_1=2, f_2=1\rangle$) state. In this example the singlet potential is deeper than the triplet potential, but it could also be the other way around. In the special case of the collision of two ^{87}Rb atoms the potential curves lie on top of each other.

atoms and $\sim 1/r^4$ for atom-ion collision. Reference [19] is recommended for further reading about atomic collisions.

2.4 Qubit States

For the application in quantum information, qubit states $|0\rangle$ and $|1\rangle$) need to be encoded in internal states of both atom and ion. It is not possible to use

electronic states for that purpose (e.g. $|0\rangle \equiv$ S-state and $|1\rangle \equiv$ P-state), because electronic excitation leads to a substantial change of the interaction potential (c.f. Section 2.2), which is undesirable for controlling the collision. Instead, specific hyperfine states are chosen to build the computational basis (see Figure 2.4). Single qubit operations can then be performed without exciting the electron in the shell. As described in Section 2.3, the hyperfine states are labeled with the quantum numbers (f_ν, m_{f_ν}). The qubit states of the atom(a) and ion(i) are e.g.

$$\begin{aligned} |0\rangle_{i/a} &= |f_{i/a} = 1, m_{f_{i/a}} = 1\rangle, \\ |1\rangle_{i/a} &= |f_{i/a} = 2, m_{f_{i/a}} = 2\rangle. \end{aligned} \tag{2.10}$$

The corresponding 2-qubit states then are

$$\begin{aligned} |00\rangle_{i,a} &= |f_i = 1, m_{f_i} = 1, f_a = 1, m_{f_a} = 1\rangle, \\ |01\rangle_{i,a} &= |f_i = 1, m_{f_i} = 1, f_a = 2, m_{f_a} = 2\rangle, \\ |10\rangle_{i,a} &= |f_i = 1, m_{f_i} = 1, f_a = 2, m_{f_a} = 2\rangle, \\ |11\rangle_{i,a} &= |f_i = 2, m_{f_i} = 2, f_a = 2, m_{f_a} = 2\rangle. \end{aligned} \tag{2.11}$$

Note that by this choice of qubit encoding the interaction is intrinsically qubit dependent, since in the ultracold regime the collision properties strongly depend on the spin state in which atom and ion are prepared initially.

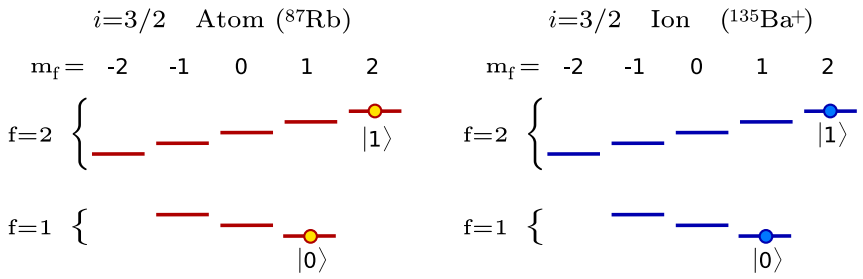

Figure 2.4: Hyperfine states of an ion and an atom with nuclear spins $i_i = 3/2$ and $i_a = 3/2$. The qubit states $|0\rangle_{i,a}$ and $|1\rangle_{i,a}$ are specific hyperfine states.

2.5 Enhancement of the Interaction by Resonances

We use resonances to enhance and control the qubit dependent interaction. Two major types of resonances are discussed: magnetic field induced Feshbach resonances and trap-induced shape resonances. In later sections, only trap-induced shape resonances are used, but one can always keep Feshbach resonances in mind as another possibility. In general, a resonance of two states ψ_1 and ψ_2 is possible, if the states are coupled by any kind of interaction. This happens, if the Hamiltonian matrix element $H_{12} = \langle\psi_1|H|\psi_2\rangle$ does not vanish. In the case of atom-ion collision, the coupling is caused by the interaction potential. The resonance then occurs where the energy levels of the two states cross when varying some external parameter. Such a situation is depicted in Figure 2.5. For simplicity, let the energy E_1 of one state be constant, while the energy $E_2(t)$ of the second state depends on time. At some point t_0, both energies are equal, i.e. $E_1 = E_2(t_0)$. Now, since the two states are coupled, the instantaneous eigenstates of the system are not ψ_1 and ψ_2, but some linear combination of both. The energy levels of these new eigenstates form an avoided crossing. By this avoided crossing, the eigenenergies keep their order, which means the lower energy level remains low and the higher level remains the higher one at all times. Crossing would mean changing this order. As a consequence an energy gap ΔE is formed at the avoided crossing. The stronger the coupling is, the bigger the gap.

The theorem of adiabaticity states that during a very slow process (compared to inherent time scales of the system), the quantum numbers of a state do not change. If the eigenstates are numbered by their energy in ascending order, this order is preserved in an adiabatic process. Details on adiabaticity can be found in [20]; a proof is given in [21]. If now the crossing point (at $t = t_0$) is passed slowly, the system always stays in the adiabatic eigenstate, which means that ψ_1 evolves to ψ_2' and vice versa. In Figure 2.5 the solid lines are followed. During a very fast passage of the energy level crossing the system has no time to follow the adiabatic eigenstates. This results in an evolution of ψ_1 to ψ_1' and ψ_2 to ψ_2' and is called diabatic (or nonadiabatic) passage. The probability P_{na} of the nonadiabatic

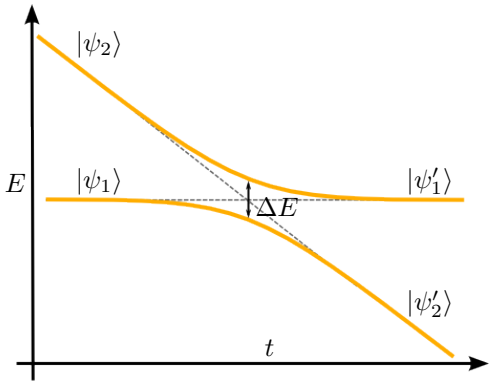

Figure 2.5: Schematic drawing of an avoided crossing of the energy levels of two states $|\psi_1\rangle$ and $|\psi_2\rangle$. The energy splitting ΔE is related to the matrix element $H_{12} = \langle\psi_1|H|\psi_2\rangle$.

passage can be estimated with the Landau-Zener formula

$$P_{\mathrm{na}} = \exp\left(-2\pi \frac{|H_{12}|^2}{\hbar|\partial(E_1(t) - E_2(t))/\partial t|}\right), \tag{2.12}$$

where $|E_1(t) - E_2(t)|$ is the difference of the slopes of the diabatic energy levels (dashed lines in Figure 2.5) and H_{12} is the coupling matrix element. For further reading about this formula we recommend [22]. The formula specified on trapped atom-ion collision is given and applied in Section 4.3.

Resonances to Molecular Bound States

The interaction potential of Figure 2.2 supports discrete bound states that are located around r_{min} and have an energy below the dissociation energy $V(r \to \infty)$. Above the dissociation energy an energy continuum of free space states is supported. This continuum is replaced by discrete trap states if an additional trapping potential is present. We refer to the states below the dissociation energy as (molecular) bound states. States with energy above the dissociation energy are referred to as unbound states or, in the case of a trap, vibrational states or trap states.

Of special interest in ultracold collision are the resonances of unbound states to bound states. Molecules can be formed via an adiabatic transition from a unbound to a molecular state. This is interesting in chemistry and molecular physics. But also the strength of the interaction is enhanced, which is useful in quantum computation. While forming a molecular state, colliding particles are close, and are affected by a much deeper potential then unbound states are.

Feshbach Resonances

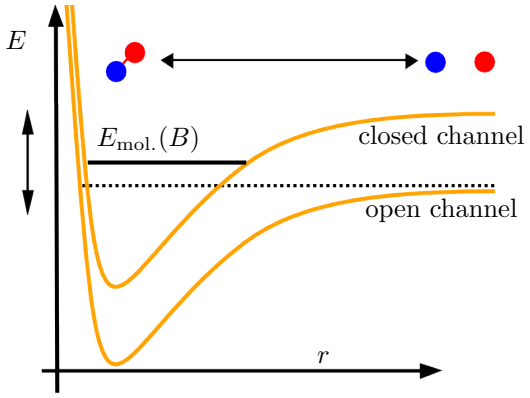

Figure 2.6: Feshbach resonance in a free ultracold gas in which atoms have kinetic energy slightly above molecular dissociation energy (dashed line): Sweeping $E_{\text{mol}}(B)$ with a magnetic field over the dissociation energy of the open channel from above causes the formation of Feshbach molecules in the closed channel. This also works in trapped gases or with only two trapped particles.

The principle of a magnetic Feshbach resonance is to bring the energy of a molecular bound state of one channel to equal the energy of a state prepared in another channel by applying a static external magnetic field.

The magnetic moment of a the atom-ion complex in the electronic ground state is a combination of the magnetic moments due to unpaired electron spins and the

magnetic moments of the nuclear spins. The magnetic moment of one electron is proportional to the spin

$$\mu_{\mathrm{el}} = -g_s \mu_B (\mathbf{s}/\hbar), \tag{2.13}$$

where μ_B is the Bohr magneton and g_s is the Landé factor of the electron. The magnetic moment of the nuclei is obtained equivalently. The potential energy in a magnetic field is proportional to the magnetic moment μ

$$U_{\mathrm{mag}} \sim -\mu \cdot \mathbf{B}. \tag{2.14}$$

Since the magnetic moment depends on the spin configuration and on the Landé factors, the magnetic field energy of unlike channels are different. Especially the energies of two channels β and γ are shifted with respect to each other when B varies.

$$\frac{\partial E_\beta(B)}{\partial B} - \frac{\partial E_\gamma(B)}{\partial B} \neq 0. \tag{2.15}$$

Let E_β be zero and E_γ be larger than E_β by the hyperfine splitting. Atom and ion are prepared in the channel β with small, positive energy. Since the energy E is larger than the dissociation energy E_β, β is referred to as an open channel. Now E can still be smaller than the dissociation energy of channel γ. In this case γ is called a closed channel. In general the potential of channel γ supports bound states corresponding to an energy lower than E_γ. These bound states usually do not have the same energy as the particles prepared in channel β have. By variation of the background magnetic field it is possible to change the relative distance between the potential curves of the two channels β and γ (see Figure 2.6). A molecular bound state of the closed channel γ can now become resonant to an unbound state, since the energy of the molecular state is swept over the energy of the unbound state. The particles can be prepared in channel β in free space or in a trap vibrational state. In both cases, a Feshbach resonance may be applicable. A more detailed review on Feshbach resonances is given in [19].

Trap Induced Shape Resonance

In contrast to Feshbach resonances, for a trap-induced shape resonance only one spin configuration (one channel) is considered and no magnetic field is needed.

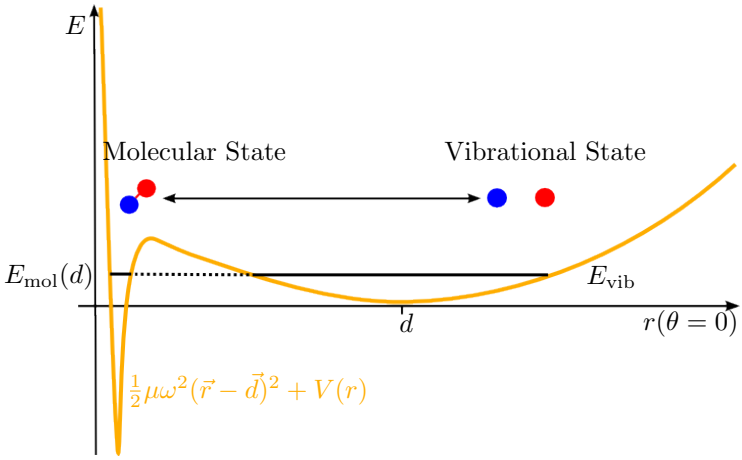

Figure 2.7: Trap-induced shape resonance: The energy of a molecular bound state in the combined potential depends on d. When it becomes equal to a vibrational level, a transfer from a vibrational state (separated particles) to a molecular bound state (connected particles) is possible.

The total potential (here in the relative coordinate r) is depicted in Figure 2.7. The relative distance of the two trap minima is denoted as d. We assume that in the relative coordinate frame the harmonic traps are displaced by d in the z-direction. Around $r = 0$ the interaction potential dominates. This potential supports molecular bound states, which have wavefunctions with a big amplitude at small atom-ion distance. At large r the external trap is dominant, and so here vibrational states in the harmonic potential exist. Vibrational states are localized at larger atom-ion distances. The barrier between the two wells is strongly modified by changing d, and therefore E_{mol} depends on d. Since the harmonic oscillator energy E_{vib} is not changed, one can let the energy of a molecular state cross the energy of a vibrational state by changing the trap displacement. If the level

coupling is strong, one can bring the atom and the ion from a trap vibrational state to a molecular bound state by sweeping d. Since at small relative distances the potential is very deep and the molecular state has a big amplitude there, this procedure enhances interaction.

The position of bound states strongly depends on the spin state of the atom and the ion, and therefore the resonance is dependent on the qubit state. Molecular state energies approximately behave like $E_{\mathrm{mol}}(d) \sim E_{\mathrm{mol}}(0) + \frac{1}{2}\mu\omega^2 d^2$. For further explanations see Equations (2.16) and (2.17) and the corresponding text in the next chapter.

2.6 Energy Spectrum

Many features of the system can be explained with the help of the spectrum of energy levels as a function of the trap displacement d. Such a spectrum is also known as a correlation diagram. In Figure 2.8 we show an example spectrum taken from [10]. Here the harmonic oscillator length is $l_0 \sim 3.48R^*$, which corresponds to $\alpha = 146.046$. At large distances the energy levels are equidistant. This is because the atom and the ion are each localized in their traps and, since these traps are well separated, the interaction is very weak. Therefore one observes harmonic oscillator levels and states that are slightly shifted by the polarization potential. Going to small distances, the oscillator levels meet bound state energies. At these points trap-induced shape resonances occur. They can be seen as avoided crossings in the spectrum. It is possible to use the avoided crossings to form molecular ions. In Chapter 5 we use qubit dependent trap-induced resonances to perform a quantum gate based on the fact that the position of the energy of the molecular state depends on the qubit channel. For larger energies and small d the spectrum has a complicated structure, but in our work we focus on the levels that are near the threshold. When d approaches zero, the interaction term dominates and big resonances appear. The energy of molecular bound states can be approximated with a quadratic function in d (blue, thick curve in Figure 2.8). This can be

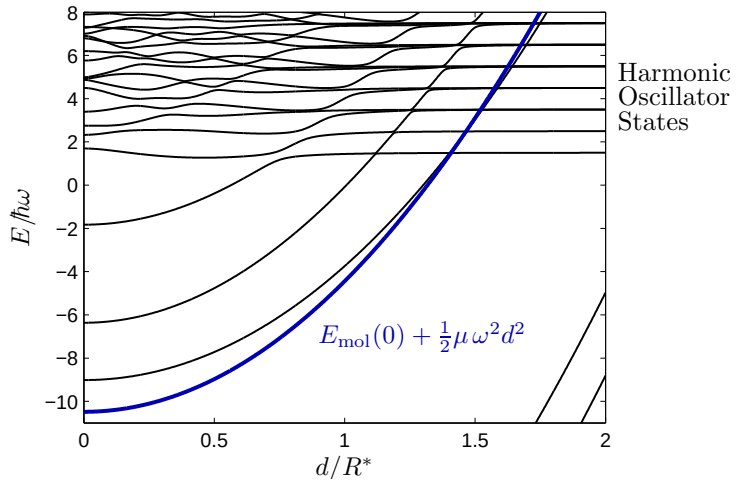

Figure 2.8: Example correlation diagram for $l_0 = 3.48R^*$. The molecular states have an approximately quadratic d-dependence. For large d, energy levels are equidistant, since the problem passes over to two harmonic oscillators without particle interaction. See text for details.

understood by looking at the Hamiltonian Equation (2.3):

$$\begin{aligned} E_{\mathrm{mol}}(d) &= \langle \Psi_{\mathrm{mol}} | H^{(d)} | \Psi_{\mathrm{mol}} \rangle \\ &= E^{(0)}_{\mathrm{mol}} + \frac{1}{2}\mu\omega^2 d^2 - \mu\omega^2 d \int \mathrm{d}^3 r\, \Psi^*_{\mathrm{mol}}\, r\cos\theta\, \Psi_{\mathrm{mol}}, \end{aligned} \tag{2.16}$$

and since molecular states are located in a narrow region around $r = 0$, the last term

$$\int \mathrm{d}^3 r\, \Psi^*_{\mathrm{mol}}(r)\, r\cos\theta\, \Psi_{\mathrm{mol}}(r) \approx 0 \tag{2.17}$$

can be neglected.

3 Quantum Defect Theory for Atom-Ion Collision

3.1 Basic Idea of a Multichannel Quantum-Defect Theory

The long range $1/r^4$ part of the polarization potential is known very well, but the short-range part of the potential is not yet directly experimentally accessible and also cannot yet be calculated precisely,because the number of electrons is quite big for atoms and ions relevant in experiments.

Quantum-defect theory attempts to solve Schrödinger's equation for the scattering problem with a reference potential that has the same long-range behavior as the actual potential, but otherwise can be arbitrary. The short-range scattering information is put into a parameter of the wavefunction, e.g. a phase shift. This quantum-defect parameter weakly depends on energy and remains analytic across the dissociation threshold, i.e. it is well defined for bound states as well as for unbound states. In the ultracold domain the short-range potential depth is orders of magnitude larger than variations of kinetic energy. Therefore the quantum-defect parameter is usually independent of energy. This makes it very useful for predicting the system properties across the threshold.

On the other hand, a molecule can dissociate to a number of channel states that are all included in a multichannel formalism. In this problem of higher dimensions, a set of quantum-defect parameters is needed.

In Section 3.2 a multichannel formalism is specified for atom-ion collision. The following sections describe how an effective single channel model can be extracted from the multichannel formalism. The Schrödinger equation for trapped atom-ion

collisions is solved in the single channel model in Section 3.4.

3.2 Closed Coupled N-Channel Model for Atom-Ion Collisions

This section formulates the multichannel atom-ion scattering problem and derives an equation for determining bound states and energy eigenlevels of the system. For details of the multichannel quantum-defect theory (MQDT) used here for atom-ion collisions we refer the reader to [23, 7]. The methods of the cited paper are developed for the free particle situation and are specified for the situation of an additional harmonic trapping potential, in what follows.

Multichannel Schrödinger Equation

An atom-ion collision is described by a N-channel closed coupled Schrödinger equation:

$$-\frac{\hbar^2}{2\mu}\Delta\mathbf{\Psi}(\mathbf{r}) + (\mathbf{W}(r) + \mathbf{U}(r) - E)\,\mathbf{\Psi}(\mathbf{r}) = 0. \tag{3.1}$$

Here $\mu = m_i m_a/(m_i + m_a)$ denotes the reduced mass, E is the energy, $\mathbf{W}$ is the interaction matrix and $\mathbf{\Psi}$ is the matrix of wavefunction solutions, which has N components, one for each channel of the coupled subspace. N linearly independent solutions are combined to form the matrix $\mathbf{\Psi}$, which is convenient for calculations.

Since the interaction term only depends on the relative distance of the two particles, the relative and center of mass coordinate parts of the Hamiltonian separate for harmonic traps of equal frequency. The center of mass part of the wavefunction is given by harmonic oscillator functions and is irrelevant for the interaction. Therefore, only the relative part is considered here. The equation is named 'coupled' because it describes N coupled channels, and 'closed' because only the subspace of coupled states is included. For example, if the total angular momentum projection $m_f = m_{f_i} + m_{f_a}$ is conserved, all channels with the same m_f can be coupled, and otherwise do not belong to the considered subspace. At large distances the channels differ in their dissociation energy E_i^∞ by the hyperfine splittings, since each channel is a certain spin configuration of the atom-ion

complex. The interaction matrix

$$\mathbf{W}_{ij}(r) \overset{r\to\infty}{\longrightarrow} \left[E_i^\infty - \frac{C_4}{r^4}\right]\delta_{ij} \tag{3.2}$$

is asymptotically diagonal. C_4 is the interaction constant defined in Table 2.2. Mixing of channels only appears at short distance, since at large distance the hyperfine states are eigenstates of the system. The short-range part of $\mathbf{W}$ does not have to be known explicitly for a quantum-defect treatment. $\mathbf{U}$ is the trapping potential

$$\mathbf{U}_{ij} = \frac{1}{2}\mu\omega^2\left(x^2+y^2+(z-d)^2\right)\delta_{ij}, \tag{3.3}$$

which is always diagonal. The coordinate frame is chosen such that the line between the two trap minima lies on the z-axis.

Special Case: $d = 0$

For $d = 0$ the external potential is spherically symmetric and the equations for different relative angular momenta l decouple. One can decompose $\mathbf{\Psi}(\mathbf{r})$ into partial waves,

$$\mathbf{\Psi}(\mathbf{r}) = \sum_l c_l \mathbf{F}_l(r) Y_{l0}(\hat{\mathbf{r}})/r. \tag{3.4}$$

The projection of angular momentum $\mathbf{l}$ on the z axis is denoted by m_l. For simplicity one can set $m_l = 0$, because the Hamiltonian does not depend on the azimuthal coordinate ϕ. The radial wavefunction $\mathbf{F}_l(r)$ of the partial wave l fulfills

$$\left[\left(-\frac{\hbar^2}{2\mu}\frac{\partial^2}{\partial r^2} + \frac{\hbar^2 l(l+1)}{2\mu r^2} + \frac{1}{2}\mu\omega^2 r^2 - E\right)\mathbf{I} + \mathbf{W}(r)\right]\mathbf{F}_l(r) = 0, \tag{3.5}$$

where l is the angular momentum quantum number of the relative motion (also called the partial wave number). The centrifugal barrier $l(l+1)/r^2$ has its origin in the angular part of the Laplacian.

In the calculation, the short-range part of the interaction potential W is mimicked by choosing an appropriate short-range phase φ. This is equivalent to setting $W_{ij} = (E_i^\infty - \frac{C_4}{r^4})\delta_{ij}$. In this case the reference potentials that are necessary to define MQDT functions can be simply related to the diagonal elements of $\mathbf{W}(r)$:

$$V_i^l \equiv E_i^\infty - \frac{C_4}{r^4} + \frac{\hbar^2 l(l+1)}{2\mu r^2}. \tag{3.6}$$

With the reference potentials one can associate a pair of linearly independent solutions that have a WKB-like normalization at small distances:

$$\left.\begin{aligned} f_i^l(r) &\cong k_i^l(r)^{-1/2} \sin \beta_i^l(r) \\ g_i^l(r) &\cong k_i^l(r)^{-1/2} \cos \beta_i^l(r) \end{aligned}\right\} r \sim r_{\min}, \tag{3.7}$$

where $k_i^l = \sqrt{2\mu(E - V_i^l(r))}/\hbar$ is the local wave vector and $\beta_i^l = \int^r k_i^l(x)\,\mathrm{d}x$ is the WKB phase. Here, $r_{\min}$ denotes the typical distance where the minima of the realistic potentials occur (see Figure 2.2) and the semiclassical approximation is applicable. In the present approach this is equivalent to the limit $r \to 0$. The solution of Equation (3.5) can be expressed in terms of the pair functions $\hat{\mathbf{f}}^l(r) = \{\delta_{ij} f_i^l(r)\}$ and $\hat{\mathbf{g}}^l(r) = \{\delta_{ij} g_i^l(r)\}$ giving

$$\mathbf{F}_l(r) = \left[\hat{\mathbf{f}}^l(r) + \hat{\mathbf{g}}^l(r)\mathbf{Y}\right] \hat{\mathbf{A}}. \tag{3.8}$$

Here, $\mathbf{Y}$ is the quantum-defect matrix that represents the effect of the short-range potential, e.g. couplings between the channels. $\mathbf{Y}(\mathbf{E})$ is a function of energy. It is important for MQDT analysis that it remains analytic across the thresholds and generally depends weakly on energy. $\hat{\mathbf{A}}$ is a constant matrix that depends on the boundary conditions at $r \to \infty$. At large distances, the trapping potential dominates, and the physical solution of one channel is

$$\psi_i^l \overset{r\to\infty}{\longrightarrow} D_\nu(\sqrt{2}r/l_0), \tag{3.9}$$

where $D_\nu(z)$ is the parabolic cylinder function with the energy $E = E_i^\infty + \hbar\omega(\nu + 1/2)$, and $l_0 = \sqrt{\hbar/\mu\omega}$ is the harmonic oscillator length. The MQDT functions $\tan \nu_i^l(E)$ and $N_i^l(E)$ relate the solutions Equation (3.7) to Equation (3.9), and can be defined as

$$\psi_i^l = N_i^l(E) \left[\cos \nu_i^l(E) \hat{\mathbf{f}}^l(r) - \sin \nu_i^l(E) \hat{\mathbf{g}}^l(r)\right], \tag{3.10}$$

where $\nu_i^l(E)$ describes a mixing of the pair functions $\hat{\mathbf{f}}$ and $\hat{\mathbf{g}}$ from Equation (3.7). Since for small r the pair functions are combined to the solution for $r \to 0$, ν_i^l is related to the short-range phase $\varphi^l(E)$ (see Section 3.2.1). $\varphi^l(E)$ can be calculated numerically in a single channel model, which is done in Section 3.6.1. An expression for the normalization $N_i^l(E)$ in terms of the short-range phase can also be derived

(see [23]) as

$$N_i^l(E) = 1 \Big/ \left(\frac{\partial \varphi}{\partial E} \right). \tag{3.11}$$

The solution $\mathbf{F}_l(r)$ can be expressed in terms of $\boldsymbol{\psi}^l(r) \equiv \{\delta_{ij}\psi_i^l(r)\}$ as

$$\mathbf{F}_l(r) = \boldsymbol{\psi}^l(r)\mathbf{A}, \tag{3.12}$$

where $\mathbf{A}$ is a constant matrix that is not to be confused with $\hat{\mathbf{A}}$ of Equation (3.8). Comparing Equation (3.8) to Equation (3.12) one gets

$$\left[\cos\boldsymbol{\nu}^l(E)\hat{\mathbf{f}}^l(r) - \sin\boldsymbol{\nu}^l(E)\hat{\mathbf{g}}^l(r)\right]\mathbf{A} = \left[\hat{\mathbf{f}}^l(r) + \hat{\mathbf{g}}^l(r)\mathbf{Y}\right]\hat{\mathbf{A}}, \tag{3.13}$$

where the quantum-defect functions $\boldsymbol{\nu}^l = \nu_i^l\delta_{ij}$ and $\mathbf{N}^l = N_i^l\delta_{ij}$ are written in matrix form. This yields two equations, since the coefficients for $\hat{\mathbf{f}}^l$ and $\hat{\mathbf{g}}^l$ must each be equal. Eliminating $\hat{\mathbf{A}}$ one arrives at

$$\left[\mathbf{Y} + \tan\boldsymbol{\nu}^l(E)\right]\mathbf{N}^l(E)\cos\boldsymbol{\nu}^l(E)\mathbf{A} = 0, \tag{3.14}$$

which has nontrivial solutions $\mathbf{A} \neq 0$, if

$$\left|\mathbf{Y} + \tan\boldsymbol{\nu}^l(E)\right| = 0. \tag{3.15}$$

This is a standard condition for determining bound states in the MQDT approach of [7]. From this condition one can determine eigenenergies in the multichannel case, while the eigenstates are given by Equation (3.12), with $\mathbf{A}$ determined from Equation (3.14). For bound states typically only one vector of $\mathbf{A}$ is nonzero; that vector is denoted as $\mathbf{b}$. This yields eigenfunctions $\mathbf{F}_{ln}(r) = \boldsymbol{\psi}^l(r)\mathbf{b}_n$ where and n enumerates the solutions of the radial equation

$$\left[\left(-\frac{\hbar^2}{2\mu}\frac{\partial^2}{\partial r^2} + \frac{\hbar^2 l(l+1)}{2\mu r^2} + \frac{1}{2}\mu\omega^2 r^2 - E_n\right)\mathbf{I} + \mathbf{W}(r)\right]\mathbf{F}_{ln}(r) = 0. \tag{3.16}$$

Solutions corresponding to different eigenenergies are orthonormal, i.e.

$$\int_0^\infty \mathrm{d}r\mathbf{F}_{ln}(r)^\dagger\mathbf{F}_{ln'}(r) = \delta_{nn'}. \tag{3.17}$$

Generalization to $d \neq 0$

The solutions of Equation (3.1) in the general case of $d \neq 0$ can be expressed as a linear combination of solutions for $d = 0$:

$$\mathbf{F}(\mathbf{r}) = \sum_{ln} c_{ln}\mathbf{F}_{ln}(r)Y_{l0}(\hat{\mathbf{r}}/r). \tag{3.18}$$

One can find the coefficients for this expansion by solving a matrix equation that is obtained by substituting Equation (3.18) in the expansion in the Schrödinger's Equation (3.1). This gives

$$\left(E_{ln} - E + \frac{1}{2}\mu\omega^2 d^2\right) c_{ln} + \mu\omega^2 d \sum_{l'n'} \langle Y_{l0}| \cos\theta |Y_{l'0}\rangle D^{ll'}_{nn'} c_{l'n'}, \tag{3.19}$$

where

$$D^{ll'}_{nn'} = \int_0^\infty \mathrm{d}\, r \mathbf{F}_{ln}(r)^\dagger r \mathbf{F}_{l'n'}(r). \tag{3.20}$$

In the single channel model derived later we use an equivalent procedure to determine the solutions to $d \neq 0$. A more detailed explanation and equations are given in this context in Section 3.5.

For the sake of clarity we summarize the main result of this section. In order to determine eigenenergies and corresponding eigenstates one has to know $\mathbf{Y}$ and $\boldsymbol{\nu}^l(E)$. A convenient way to determine the quantum-defect matrix $\mathbf{Y}$ is described in Section 3.2.2, and uses a frame transformation. The MQDT function $\nu_l(E)$ can be determined by calculating the short-range phase $\varphi(E)$. This is done in Section 3.6.1.

3.2.1 Short-Range Phase, MQDT Function and Scattering Length

Since at small distance for a $1/r^4$ potential the de Broglie wavevector is $k_i^l \sim 1/r^2$ and the WKB phase is $\beta \sim -1/r$, the pair functions of Equation (3.7) take the form

$$\left.\begin{aligned} f_i^l(r) &\cong r \sin -\tfrac{1}{r} \\ g_i^l(r) &\cong r \cos -\tfrac{1}{r} \end{aligned}\right\} r \to 0. \tag{3.21}$$

The same solutions can also be obtained directly by solving the radial equation in the limit $r \to 0$ with energy, trap and centrifugal barrier neglected. Any solution can be written as a linear combination of f and g. In the $r \to 0$ limit of Equation (3.21), Equation (3.10) translates to

$$\begin{aligned} \psi_i^l(r) &\xrightarrow{r\to 0} N_i^l(E) \left[r\, \cos\nu_i^l(E) \sin(-1/r) - r\, \sin\nu_i^l(E) \cos(-1/r)\right] \\ &= -N_i^l(E) \left[r\, \sin(1/r + \nu_i^l(E))\right] \\ &\sim r\, \sin(1/r + \varphi(E)), \end{aligned} \tag{3.22}$$

and therefore the MQDT function $\nu_i^l(E)$ can be interpreted as a energy dependent short-range phase $\varphi(E)$ of the wavefunction.

For our choice of the MQDT functions $\hat{\mathbf{f}}$ $\hat{\mathbf{g}}$ of Equations (3.7), the asymptotic solutions of Equation (3.21) become valid for all distances for the s-wave ($l = 0$) in free space ($\omega = 0$) at energy $E = 0$. On the other hand, the zero energy scattering solution asymptotically behaves like

$$\Psi(r) \overset{r\to\infty}{\longrightarrow} 1 - a/r. \tag{3.23}$$

The linear combination of Equation (3.22) has the asymptotic behavior

$$\begin{aligned} \Psi(r) = \frac{\psi^{l=0}(r)}{r} &\overset{r\to\infty}{\longrightarrow} N\left[\frac{\cos\varphi}{r} - \sin\varphi\right] \\ &= \tilde{N}\left[1 - \frac{-\cot\varphi}{r}\right]. \end{aligned} \tag{3.24}$$

Therefore one can relate the short-range phase φ to the s-wave scattering length

$$a = -\cot\varphi, \tag{3.25}$$

which is a measurable physical quantity given by the system.

3.2.2 Parametrization of $\mathbf{Y}$ at Small Distance and Frame Transformation

In the ultracold regime, energy variations are much smaller than the depth of the real potential at $r = r_{\min}$ and therefore it is justified to neglect the energy dependence of $\mathbf{Y}(\mathbf{E})$ and set $\mathbf{Y}(E) \cong \mathbf{Y}$. It is then sufficient to determine $\mathbf{Y}$ at one energy. It is convenient to express $\mathbf{Y}$ in terms of few parameters, for example scattering lengths using a frame transformation. For application, we consider the collision of an alkali atom with an alkaline earth ion, which are in their electronic ground states. As described in Section 2.3, the asymptotic channel states are characterized by the hyperfine quantum numbers (f_i, m_{f_i}) and (f_a, m_{f_a}) for the ion and the atom respectively, and by the angular momentum quantum number l and m_l of relative motion of the atom and the ion. The asymptotic channel states are labeled with $\beta = \{f_i, f_a, m_{f_i}, m_{f_a}, l, m_l\}$. The eigenbasis at short distances according to the LS coupling scheme is characterized by the total electron spin

$\mathbf{s} = \mathbf{s}_i + \mathbf{s}_a$, the total nuclear spin $\mathbf{i} = \mathbf{i}_i + \mathbf{i}_a$ and additionally by the total hyperfine angular momentum $\mathbf{f} = \mathbf{i} + \mathbf{s}$ and its projection m_f on the axis of quantization. Here, $\mathbf{s}_i$, $\mathbf{s}_a$ denote the electron spin of ion and atom respectively, and $\mathbf{i}_i$, $\mathbf{i}_a$ are the nuclear spins of the ion and the atom involved. In the is basis the channels are labeled by $\gamma = \{i, s, f, m_f, l, m_l\}$. The unitary transformation

$$U_{\beta\gamma} = (f_1 f_2 m_{f_1} m_{f_2} | isfm_f) \tag{3.26}$$

from β to γ is called a frame transformation. It can be expressed in terms of Clebsh-Gordan coefficients and Wigner 9j-symbols (see e.g.[24]). Here, for simplicity, the quantum numbers l and m_l are omitted, because they are not transformed.

The quantum-defect matrix is determined at a distance, where it is diagonal in is representation. Mixing of the asymptotic channels typically arises in the core region of the atom-ion complex, where the real potential starts to deviate from the $1/r^4$ law. This distance is denoted as r_0 and is of the order of a few a_0 (Bohr radii). At $r \gtrsim r_0$ the exchange interaction is negligible. On the other hand, for $r \ll R^*$ one can safely ignore the centrifugal potential and hyperfine splitting. The long range atom-ion interaction provides a separation of length scales: $r_0 \ll R^*$. In the region where $r_0 \lesssim r \ll R^*$ the real potential is of the form $W_{ij} \cong -C_4/r^4 \delta_{ij}$ and therefore is equal to the reference potentials as defined in Equation (3.6) (with hyperfine energy and centrifugal barrier neglected). The wavefunction is given by a linear combination of the pair functions of Equation (3.7). The short-range phase corresponding to the linear combination is related to a scattering length according to Equations (3.24) and (3.25) in Section 3.2.1. Since in the specified regime the channels in the is representation are not mixed, the quantum-defect matrix takes the diagonal form

$$Y^{(is)}_{\gamma\gamma'} = \delta_{\gamma\gamma'} \left[a_{s(\gamma)}\right]^{-1}. \tag{3.27}$$

Here, $s(\gamma)$ is the total spin in the channel γ, which can take the values $s(\gamma) = 0, 1$ corresponding to singlet a_s and triplet a_t scattering lengths, respectively. In the asymptotic hyperfine channel representation, $\mathbf{Y}$ is generally not diagonal and can now be determined with the frame transformation $U_{\beta\gamma}$, giving

$$Y_{\beta\beta'} = U_{\beta\gamma} Y^{(is)}_{\gamma\gamma'} U_{\gamma'\beta'}. \tag{3.28}$$

An example can be found in Section 3.6.3.

3.3 Single Channel Equations

A single channel picture assumes that either there is only one channel, or no couplings to other scattering channels exist. In other words the colliding particles do not change their spin states. The matrices of the multichannel formalism reduce to scalars in that case. The Equation equivalent to (3.1) reads

$$-\frac{\hbar^2}{2\mu}\Delta\Psi(\mathbf{r}) + \left(W + \frac{1}{2}\mu\omega^2\left(x^2+y^2+(z-d)^2\right) - E\right), \Psi(\mathbf{r}) = 0 \tag{3.29}$$

where the long range part of the interaction potential W is

$$W(r) \overset{r\to\infty}{\longrightarrow} E_i^\infty - \frac{C_4}{r^4}. \tag{3.30}$$

Setting the dissociation energy E^∞ to zero removes this energy offset in W. It is sufficient for all problems in this thesis to solve the Schrödinger equation for $d = 0$ and use the resulting wavefunctions to decompose the solutions for $d \neq 0$. In that case, both traps lie on top of each other and the problem becomes spherically symmetric. Equivalently to Equation (3.4), a partial wave expansion of Ψ is performed

$$\Psi(\mathbf{r}) = \sum_l c_l \psi_l(r) Y_{l0}(\hat{\mathbf{r}})/r, \tag{3.31}$$

where Y_{lm} are spherical harmonics. The factor $1/r$ is introduced to remove the first order derivative of the Laplacian in spherical coordinates. The corresponding radial part of the wavefunction $\psi_l(r)$ fulfills

$$-\frac{\partial^2}{\partial r^2}\psi_l(r) + \frac{2\mu}{\hbar^2}\left(\frac{\hbar^2}{2\mu}\frac{l(l+1)}{r^2} + \frac{1}{2}\mu\omega^2 r^2 + W(r) - E\right)\psi_l(r) = 0. \tag{3.32}$$

In terms of quantum-defect theory one replaces the real interaction potential $W(r)$ by a reference potential $V(r)$ that produces the correct asymptotics. Here,

$$V(r) = -\frac{C_4}{r^4} \tag{3.33}$$

is chosen, which is divergent for $r \to 0$. Equation (3.32) becomes

$$-\frac{\partial^2}{\partial r^2}\psi_l(r) + \frac{2\mu}{\hbar^2}\left(\frac{\hbar^2}{2\mu}\frac{l(l+1)}{r^2} + \frac{1}{2}\mu\omega^2 r^2 + V(r) - E\right)\psi_l(r) = 0. \tag{3.34}$$

Two linearly independent solutions can be associated to the reference potential, equivalent to Equation (3.7). In the limit of $r \to 0$ these functions are chosen as

$$\left.\begin{aligned} \hat{f}(r) &\cong r \sin 1/r \\ \hat{g}(r) &\cong r \cos 1/r \end{aligned}\right\} r \to 0. \tag{3.35}$$

A solution of Equation (3.34) can be expressed in terms of the reference functions

$$\psi_l(r) = \tilde{N}\left[\hat{f}(r) + \hat{g}(r)\tan\varphi_0\phi\right] = N\, r\, \sin(1/r + \varphi 0), \tag{3.36}$$

and in the limit

$$\psi_l(r) \overset{r\to\infty}{=} N\, r\, \sin(1/r + \varphi_0). \tag{3.37}$$

Here, N and $\tilde{N}$ are normalization constants. Comparing this to Equation (3.8), the quantum-defect matrix is now replaced by a single parameter φ_0: $\mathbf{Y} \hat{=} \tan\varphi_0$. By Equation (3.37) the short-range part of the real potential is replaced by a boundary condition for the wavefunction at the origin that fixes the short-range phase φ. The condition determining bound states (Equation (3.15)) becomes simply

$$\varphi(E) = \varphi_0. \tag{3.38}$$

The energy dependent short-range phase must match the quantum-defect parameter.

3.4 Solving the Radial Single Channel Equation for $d = 0$

This section assumes that a given quantum defect parameter, the short-range phase φ_0, sets a boundary condition for the solution $\psi_l(r)$ of the radial Schrödinger Equation (3.34). This quantum-defect parameter is independent of energy, but can depend on the partial wave l. In the characteristic units R^* and E^* (see Table 2.2) the dimensionless form of the radial Schrödinger equation for $d = 0$ is:

$$-\frac{\partial^2}{\partial r^2}\psi_{nl}(r) + \left(\frac{l(l+1)}{r^2} + \alpha r^2 - \frac{1}{r^4} - E_n\right)\psi_{nl}(r) = 0. \tag{3.39}$$

This equation is solved numerically using the renormalized Numerov method. On a given grid the ratio $R_i = \psi_{i+1}/\psi_i$ is calculated instead of determining ψ_i directly,

which suppresses numerical errors. Details of the Numerov method can be found in Section A.1 and in [25]. The second order linear differential equation can be brought to the standard form for the Numerov method (see Equation (A.1))

$$\left[\frac{\partial^2}{\partial r^2} + Q(r)\right]\psi(r), \tag{3.40}$$

with

$$Q(r) = -\left(\frac{l(l+1)}{r^2} + \alpha r^2 - \frac{1}{r^4} - E\right). \tag{3.41}$$

3.4.1 Discussion of the Numerical Solution of the Schrödinger Equation with a $-1/r^4$ Potential

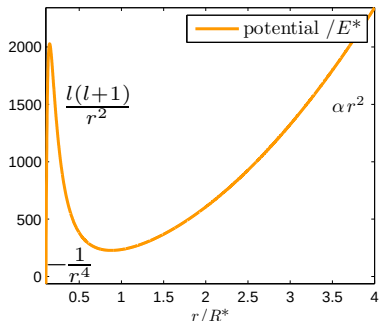

Figure 3.1: Example potential for $l = 9$ and $\alpha = 146.046$ with long range trap part, centrifugal barrier and short-range interaction potential. The height of the centrifugal barrier is given by $l^2(l+1)^2/4E^*$.

There are several features of $Q(r)$ to be discussed. First, there is the diverging negative potential for $r \to 0$ that does not allow numerical solving of Schrödinger's equation up to $r = 0$. One must stop at a minimum distance called $r_{\min}$. Since the wavefunction oscillates very fast where the potential is very deep, an extremely fine grid is needed at small r. Secondly, the centrifugal barrier becomes important for large angular momenta. Its height is given by $l^2(l+1)^2/4$ in units of E^*. For energies well below this height the wavefunctions show a harmonic-oscillator-like structure; they are localized on the right of the centrifugal barrier. However, bound states localized on the left are possible but rather rare. In addition they

are only weakly coupled to the harmonic oscillator part, because the tunneling through the centrifugal barrier is very weak for large l.

While solving the Schrödinger equation in position representation, one should always go in the direction of increasing wavefunction amplitude. In particular in a classically forbidden region like the high centrifugal barrier, the unphysical solution of the Schrödinger equation would otherwise grow exponentially and would gain in amplitude due to numerical errors. The stable implementation of the Numerov method (see Appendix A.1) iterates from both sides always going out of a forbidden region and in the direction of increasing wavefunction amplitude. The left hand and right hand solutions are matched at a point r_M in the middle of the classically allowed region. The Numerov method uses a grid in r-space; the minimum value is $r_{\min}$ and the maximum value is $r_{\max}$, which must be finite. Iteration at $r_{\max}$ starts with $\psi(r_{\max} + h = 0)$ and $\psi(r_{\max}) \neq 0$. $r_{\max}$ must be chosen big enough to make the error produced by this procedure sufficiently small. At $r_{\min}$, the asymptotic solution including the quantum-defect parameter φ_0 is used to start the iteration. Therefore $r_{\min}$ must be chosen small enough to make sure that the asymptotic solution is accurate. Formulas to calculate start and end point of the grid are given in Section 3.4.2.

Typical wavefunctions are depicted in Figure 3.2, Figure 3.1 shows an example potential $Q(r)$. The wavefunctions oscillate very fast at small r where the $1/r^4$ term dominates, and shows slower oscillations for r on the right side of the centrifugal barrier. The wavefunction $\psi(r)$ decays exponentially for large r, because here the harmonic trap term αr^2 dominates. For large l and energies below the centrifugal barrier the wavefunction looks almost like a harmonic oscillator function, slightly shifted by the interaction potential. Computational effort is minimized by adapting the grid used to the specific problem. In the method we use, the number of grid points per oscillation is monitored and kept larger than a certain lower bound K. An estimation of the oscillation period is given by the local de Broglie wave length:

$$\lambda(r) = 2\pi/k(r), \tag{3.42}$$

where

$$k(r) = \sqrt{|E - V(r)|} = \sqrt{|Q(r)|} \tag{3.43}$$

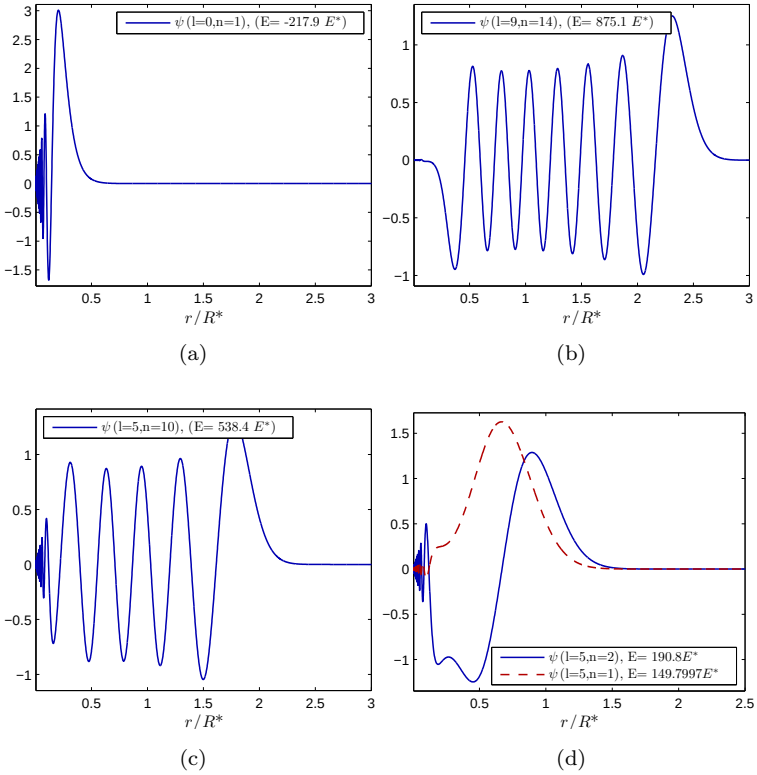

Figure 3.2: Plots showing different types of wavefunctions for $d = 0$: Molecular bound state (a), vibrational states with energy below (b) and above (c) the centrifugal barrier. In (b) the molecular part on the left of the centrifugal barrier is strongly suppressed. Also, hybrid states (d) are possible; they correspond to bound states in the centrifugal barrier ($E > 0$).

is the local de Broglie wave number. The grid is created starting from the right, at $r_{\max}$, with a starting step size $h = h_{max}$ that should be sufficiently small. Going to $r_{\min}$, the step size h is halved as soon as $K \times h > \lambda(r)$. $Q(r)$ in Equation (3.43) is evaluated with a typical value for the angular momentum $l = l_0$ and an energy $E = E_0$, e.g. $l_0 = 0$ and $E_0 = 70\hbar\omega$ (the particular choice is unimportant). The resulting grid is used to generate all the functions that are needed. Typically

$K = 20$ grid points per oscillation period is sufficient, but $K \approx 100$ is safer, because the same grid is used for all functions.

In Appendix A.1.4 and A.1.5 where the Numerov method is explained, step doubling and step halving for a Numerov iteration is introduced. The derived formulas are used for the calculation of the wavefunctions on the given grid.

3.4.2 Choice of $r_{\max}$ and $r_{\min}$

The maximum value of r is chosen such that the interaction potential is negligible with respect to the trapping potential at $r = r_{\max}$. For lower energies this can be estimated as

$$\frac{1}{r_{\max}^4 \alpha r_{\max}^2} \ll 1, \text{ or} \qquad r_{\max} = \sqrt[6]{\frac{1}{\alpha\epsilon}}. \tag{3.44}$$

Here, $\epsilon \ll 1$ gives the approximate numerical accuracy. For higher energies one also must make sure that $E \ll \alpha r_{\max}^2$, because the Numerov method requires $r_{\max}$ to be far into the classically forbidden region, where the wavefunction decays exponentially and has a very small amplitude. At the inner boundary $r = r_{\min}$, the asymptotic differential equation of Bessel type must hold. That is

$$\begin{gathered}\left(\frac{l(l+1)}{r_{\min}^2} - \frac{1}{r_{\min}^4 + \alpha r_{\min}}\right) \gg E, \\ \text{or} \\ \left(\frac{l(l+1)}{r_{\min}^2} - \frac{1}{r_{\min}^4 + \alpha r_{\min}}\right) = E/\epsilon.\end{gathered} \tag{3.45}$$

We set $\epsilon = 10^{-6}$ for the calculations in this thesis.

3.4.3 Asymptotic Behavior of the Wavefunctions

For simplicity we first focus on the special case $l = 0$, when there is no centrifugal barrier. In the asymptotic limit of $r \to 0$, the trap and energy term can be neglected and the radial differential equation becomes of the form

$$\left[\frac{\partial^2}{\partial r^2} + \frac{1}{r^4}\right] \psi(r) = 0. \tag{3.46}$$

The two linearly independent solutions of this second order differential equation are $\psi_1 \sim r\cos(1/r)$ and $\psi_2 \sim r\sin(1/r)$. This is also the asymptotic form of the pair

functions in Equation (3.7) associated with the $1/r^4$ potential of quantum-defect theory of atom-ion collision, as discussed in Section 3.2. A particular solution is then determined by the quantum-defect parameter φ_0:

$$\psi(r) = \tilde{N} r \left(\cos(\varphi_0) \sin\left(\frac{1}{r}\right) + \sin(\varphi_0) \cos\left(\frac{1}{r}\right) \right) = \tilde{N} r \sin\left(\frac{1}{r} + \varphi_0\right). \quad (3.47)$$

Including the centrifugal barrier for $l \geq 0$ the asymptotic differential equation is the Bessel equation

$$\left[\frac{\partial^2}{\partial r^2} + \frac{1}{r^4} - \frac{l(l+1)}{r^2} \right] \psi(r) = 0, \quad (3.48)$$

whose two linearly independent solutions are given by the spherical Bessel functions $\psi_1 \sim \sqrt{r}\, \mathrm{J}_{l+1/2}(1/r)$ and $\psi_2 \sim \sqrt{r}\, \mathrm{Y}_{l+1/2}(1/r)$. The asymptotic wavefunction

$$\psi_{\mathrm{asymp}}(r) = N\sqrt{r} \left(\mathrm{J}_{l+1/2}\left(\frac{1}{r}\right) + \tan(\delta) \mathrm{Y}_{l+1/2}\left(\frac{1}{r}\right) \right) \quad (3.49)$$

contains the short-range phase in the coefficients of a linear combination of those functions. The mixing angle δ is connected to the short-range phase φ_0. In the limit $r \to 0$, $\psi_{\mathrm{asymp}}(r)$ must approach $Nr \sin(1/r + \varphi_0)$, since in this limit the centrifugal barrier becomes negligible and the differential Equation (3.48) becomes Equation (3.46). This constraint fixes δ to equal $(-\varphi_0 - l\pi/2)$. Including the centrifugal barrier in the asymptotic solution allows larger values of r_{min} which saves computing time and memory usage, since one has to resolve less of the very fast oscillations at a small r.

3.4.4 Determination of Eigenenergies

The solution of the radial Schrödinger equation in our model has to fulfill a boundary condition at $r = 0$ given by the short-range phase. This boundary condition has an influence on the eigenenergies as well. Eigenenergies are searched for between a minimal energy E_{min} and a maximal energy E_{max}. To make sure that enough states are found, E_{max} is about $80\hbar\omega$. E_{min} should be sufficiently negative to allow several bound states for lower l. For a given partial wave l a trial energy E is set and Equation (3.39) is solved. As described in Section 3.4, first a backwards integration starts from a large initial r_{max}. Because of the exponential decay of the wavefunction one can set $\psi(r_{\mathrm{max}} + h)$ to zero, while $\psi(r_{\mathrm{max}}) \neq 0$.

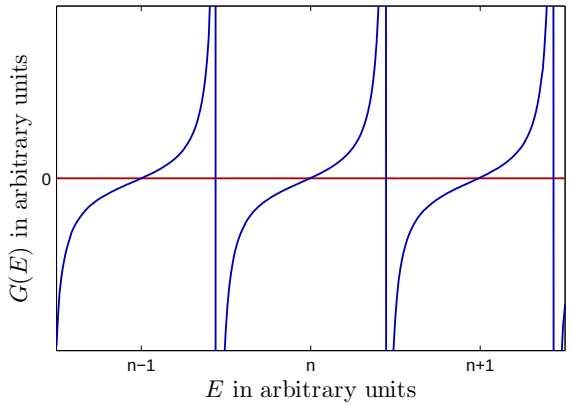

Figure 3.3: Typical aspect of the help function G defined in Equation (3.50). The function passes the roots n, $n-1$ and $n+1$ with positive slope. Between the roots G has poles. This figure was created with an angular momentum of $l = 10$.

With the resulting end condition $\tilde{R}_{N+1} = \infty$, the Numerov formula is iterated to a certain matching point r_M in the classically allowed region and then stopped. Then, the left hand side of the wavefunction is calculated starting at $r_{\min} = r_0$ with the initial condition given by the asymptotic solution of Equation (3.49), $R_0 = \psi_{\text{asymp}}(r_1)/\psi_{\text{asymp}}(r_0)$. Iteration of the Numerov formula goes up to the chosen matching point where left and right solution are fitted. While in principle the choice of r_M is arbitrary, it is advantageous to use the first maximum/minimum of the wavefunction, seen from the right side. At this point the Numerov ratio $\tilde{R}_n$ first becomes smaller than one in the backwards iteration.

A help function $G(E)$ matching the left- and right-hand solution is defined as

$$G(E) = \frac{1}{\tilde{R}_{M+1}} - R_M = \left(\frac{\psi(r_M + h)}{\psi(r_M)}\right)_{\text{right}} - \left(\frac{\psi(r_M + h)}{\psi(r_M)}\right)_{\text{left}}. \tag{3.50}$$

G is zero if right and left hand solutions are the same, which is the case if and only if E is an eigenvalue of the Hamiltonian $H^{(0)}_{\text{rel}}$ for a fixed short-range phase. A typical form for G is depicted in Figure 3.3. It has poles between each root, where the left hand solution becomes zero. If defined as in Equation (3.50), $G(E)$ always passes a root with positive slope, and at the poles it jumps from plus to

minus.

The roots of G are located roughly with sweep over energy, which detects sign changes of G. If in addition the slope is positive, a root must lie in between the values of different sign, and one can apply standard root finding routines. The routine we use begins with three bisection iterations and then finds the root with a high precision of nine digits with the faster secant method. The secant method can be unstable, so if it starts to diverge, some more bisections are performed, since bisection cannot fail. It is important to note that the precision of nine digits is not the computational accuracy of all our algorithms, because the G function we calculate is much less accurate (the goal is 10^{-6} relative error tolerance). These two rootfinding routines can be found in [26] with example implementations in the C programming language. The special choice of r_M has its advantage in the fact that the roots of G are located in the middle between two poles with this choice. Choosing a different r_M can cause the root to come close to a pole. A root in the vicinity of a pole is not that easy to handle, since typically the secant method diverges in this case. Details of this procedure can be read in [25].

3.5 Solution for the General Case $d \neq 0$ in a Single Channel Model

In this section we find the eigenenergies and wavefunctions for the general case $d \neq 0$. In doing so we obtain the energy spectrum of the relative Hamiltonian showing the eigenergies of the system as a function of the trap displacement d. This spectrum is very useful to understand the dynamics of the controlled collision, since trap induced shape resonances can be seen as avoided crossings in the spectrum. For the sake of clarity we rewrite the Hamiltonian of Equation (2.3):

$$H_{\mathrm{rel}}^{(d)} = H_{\mathrm{rel}}^{(0)} - \mu\omega^2 d\, z + \frac{1}{2}\mu\omega^2 d^2. \tag{3.51}$$

3.5.1 Choice of the Basis

The task is to find eigenenergies and eigenfunctions of the relative Hamiltonian for each trap separation d that is of interest. This can be done in position representa-

tion, where the Schrödinger equation is a second order differential equation with three coupled components (x,y and z). However, solving these differential equations is difficult and computationally expensive. It is more convenient to choose an orthonormal basis. For that purpose we use the wave functions $\Psi_{nl}^{(0)}(\mathbf{r})$ for $d = 0$. The eigenfunctions for the general case $d \neq 0$ are decomposed in that basis:

$$\Psi^{(d)}(\vec{r}) = \sum_{nl} c_{nl} \Psi_{nl}^{(0)}(\vec{r}). \tag{3.52}$$

This choice is convenient, since $\Psi_{nl}^{(0)}(\mathbf{r})$ already diagonalizes the part $H_{\mathrm{rel}}^{(0)}$ of Equation (3.51). A wavefunction for $d \neq 0$ is then characterized by a set of coefficients c_{nl}. The task is now shifted to the calculation of basis functions and finding the matrix elements of the Hamiltonian in the chosen basis.
The Hamiltonian is spherically symmetric for $d = 0$. The eigenfunctions can be separated into angular and radial part (see Equation (3.31)), which makes them easier to calculate than functions for $d \neq 0$:

$$\Psi_{nl}^{(0)}(\mathbf{r}) = \psi_{nl}(r) Y_{l0}(\hat{\mathbf{r}})/r.$$

The solutions for the angular part are spherical harmonics $Y_{l,m_l}(\theta, \phi)$, since the interaction potential only depends on the radial coordinate r. It is sufficient to consider the projection of the angular momentum $m_l = 0$, because for our choice of the coordinate frame ($\mathbf{d} = d\hat{\mathbf{e}}_z$) the Hamiltonian does not depend on the azimuthal coordinate ϕ. The radial part of the wavefunction, $\psi_{nl}(r)$, is found by solving the radial equation(see Section 3.4).

As the basis is infinitely large, one has to truncate it at a minimal energy and at a maximal energy. One has to make sure that the basis is large enough to decompose all needed states, especially for large d. In our case, a maximal energy of $E_{\max} = 80\hbar\omega$ is sufficient. For the trap induced shape resonances, one needs some molecular bound states close to threshold ($E = 0$). We use all bound states between $E = 0$ and a minimal negative Energy $E_{\min} = -1000E^*$ (the characteristic energy scale for the bound states is E^*, while the level spacing above the threshold is given by $\hbar\omega$).

3.5.2 Derivation of a Matrix Equation

On order to diagonalize the Hamiltonian for $d \neq 0$ the Schrödinger equation

$$\left(H_{\mathrm{rel}}^{(0)} - \mu\omega^2 dz + \frac{1}{2}\mu\omega^2 d^2\right)\Psi^{(d)}(\mathbf{r}) = E^{(d)}\Psi^{(d)}(\mathbf{r}) \tag{3.53}$$

has to be solved and for that we use the eigenbasis of $H_{\mathrm{rel}}^{(0)}$. The basis functions are characterized by the quantum numbers n and l. We now sort the wavefunctions in ascending order with respect to the energy eigenvalue. We now re-label the eigenfunctions and eigenenergies with the new index k that replaces the quantum numbers n and l, for convenience.

We find a set of equations for determining the eigenenergies $E^{(d)}$ and the vector of coefficients $\{c_k\}$ characterizing the corresponding eigenfunction by substituting Equation (3.52) into Equation (3.51). We use the eigenvalue equation $H_{\mathrm{rel}}^{(0)}\Psi_k^{(0)}(\vec{r}) = E_k^{(0)}\Psi_k^{(0)}(\vec{r})$ to obtain

$$\sum_k c_k \left(E_k^{(0)} - \mu\omega^2 dz + \frac{1}{2}\mu\omega^2 d^2\right)\Psi_k^{(0)}(\vec{r}) = E^{(d)}\sum_k c_k.\Psi_k^{(0)}(\vec{r}). \tag{3.54}$$

We multiply $\Psi_{k'}^0(\vec{r})$ from the left and integrate over r to obtain

$$c_{k'}\left(E_{k'}^{(0)} + \frac{1}{2}\mu\omega^2 d^2\right) + \mu\omega^2 d\sum_k c_k \int \mathrm{d}^3 r\, \Psi_{k'}^*(\vec{r}) z \Psi_k(\vec{r}) = E^{(d)} c_{k'}. \tag{3.55}$$

Now we introduce the dipole matrix element

$$\begin{aligned} M_{k'k} &= \int \mathrm{d}^3 r\, \Psi_{k'}(r)^* z \Psi_k(r) \\ &= \int_0^\infty r^3 R_{nl}^*(r) R_{n'l'}(r)\mathrm{d}r \\ &\quad \times \int_0^{2\pi}\int_0^\pi \cos(\theta)\sin(\theta) Y_{lm}(\theta,\phi)^* Y_{lm}(\theta,\phi)\mathrm{d}\theta\mathrm{d}\phi. \end{aligned} \tag{3.56}$$

Equation (3.55) is a matrix equation that can be written in the form

$$\sum_k H_{k'k} c_k = E^{(d)} c_{k'}, \tag{3.57}$$

where

$$H_{k'k} = \left(E_{k'}^{(0)} + \frac{1}{2}\mu\omega^2 d^2\right)\delta_{k',k} - 2\mu\omega^2 d M_{k'k}, \tag{3.58}$$

or

$$\mathbf{Hc} = E^{(d)}\mathbf{c}, \tag{3.59}$$

where $\mathbf{H}$ is a matrix, $\mathbf{c}$ is an eigenvector and $E^{(d)}$ is an eigenvalue. All linear independent solution vectors $\{\mathbf{c}_j\}$ can be combined to form the matrix $\mathbf{C}$. In doing so Equation (3.59) becomes

$$\mathbf{HC} = \mathbf{E}^{(d)}\mathbf{C}, \tag{3.60}$$

where $\mathbf{E}^{(d)}$ is a diagonal matrix containing the eigenenergies $E_j^{(d)}$. This matrix equation can be solved using standard matrix diagonalization routines in order to obtain $\mathbf{E}^{(d)}$ and $\mathbf{C}$. We can plot all the eigenenergies as a function of d to obtain the energy spectrum (or correlation diagram), in which we observe avoided crossings at the locations of trap-induced shape resonances (see Figure 2.8). The eigenstates for $d \neq 0$ are obtained in terms of a set of coefficients that can be substituted to Equation (3.52) (using also Equation (3.31)) to obtain the wavefunctions in position representation. These coefficients can also be used for the simulation of the time evolution of the system (see Chapter 4).

3.6 Formulation of a Single Channel Model

The advantage of a single channel model is the fact that a scalar wavefunction is to be computed instead of an $N \times N$ matrix of wavefunctions. In this section an effective single channel model is extracted from the multichannel case. The result is an effective short-range phase that can be used in a single channel formalism to obtain the same result as the multichannel formalism would provide.

3.6.1 Short-Range Phase as a Function of Energy

The multichannel formalism described in Section 3.2 is based on quantum-defect theory. The MQDT functions $\tan\nu^l(E)$ and $N^l(E)$ play a central role. As shown in Section 3.2.1 one can define the pair functions in Equation (3.7) in such a way that the function $\nu^l(E)$ equals the short-range phase $\varphi^l(E)$. The normalization function $N^l(E) = 1/(\partial\varphi^l(E)/\partial E)$ can also be related to the short-range phase (see

Equation (3.11)). The short-range phase can be calculated numerically by solving Equation 3.39 in a single channel picture for dense energy points. In the radial equation one can set $E^{\infty} = 0$; the offset is given by the hyperfine splitting energy and can be added later. Energies below zero then correspond to molecular bound states, while energies larger than zero belong to trap vibrational states. We present here a stable way of extracting the short-range phase with the Numerov method. The wavefunction ψ_n must be iterated from $r_{\min}$ to r_M, and from $r_{\max}$ to r_M. This makes it a requirement to fix the short-range phase as an boundary condition for the wavefunction at $r_{\min}$. On the one hand we need to fix a short-range phase on the wavefunction and on the other hand we want to obtain precisely this phase from the calculation. This problem can be solved writing the actual wavefunction $\psi(r)$ as a linear combination of $\psi_1(r)$ and $\psi_2(r)$

$$\psi(r) = c_1\psi_1(r) + c_2\psi_2(r). \tag{3.61}$$

We choose the pair of basis solutions $\psi_{1,2}$ in a way that their asymptotic forms are

$$\psi_{1,2}(r) \xrightarrow{r\to 0} r\sin(1/r + \varphi_{1,2}), \tag{3.62}$$

We fix the short-range phases $\varphi_1 = 0$ and $\varphi_2 = \pi/2$ of these basis functions and obtain the real value by a linear combination of ψ_1 and ψ_2. One behaves as a sine function, the other as a cosine function, at $r \to 0$, which are clearly linearly independent.

The formula of Liouville (see e.g. [27]) states that if two solutions of a linear differential equation are linearly independent at one point r_0, they will be linearly independent on every other point of the considered interval. Therefore ψ_1 and ψ_2 are linearly independent on the right of the centrifugal barrier. In terms of Bessel functions the two solutions become

$$\psi_{1,2}(r) \xrightarrow{r\to 0} \sqrt{r}\left(\cos(-\varphi_{1,2} - l\pi/2)\mathrm{J}_{l+1/2}\left(1/r\right) + \sin(-\varphi_{1,2} - l\pi/2)\mathrm{Y}_{l+1/2}\left(1/r\right)\right), \tag{3.63}$$

and this asymptotic behavior is valid before the sine-like asymptotic form is valid in the limit of $r \to 0$. Those two functions are propagated with the Numerov method to a matching point r_M. Propagating backwards, the solution ψ^+ is found with

the usual initialization $\psi(r_{\max}+h)=0$, $\psi(r_{\max})\neq 0$. In general neither ψ_1 nor ψ_2 match ψ^+. However, a linear combination of ψ_1 and ψ_2 will match the right hand side ψ^+, so that

$$c_1\psi_1(r)+c_2\psi_2(r)=c_3\psi^+(r). \tag{3.64}$$

Evaluating this equation at $r=r_M$ and $r=r_M+h$ and then dividing the two equations allows us to determine the ratio of the coefficients c_2/c_1:

$$C \equiv \frac{c_3\psi^+(r_M)}{c_3\psi^+(r_M+h)}=\frac{c_1\psi_1(r_M)+c_2\psi_2(r_M)}{c_1\psi_1(r_M+h)+c_2\psi_2(r_M+h)}, \tag{3.65}$$

$$\frac{c_2}{c_1} = \frac{\psi_1(r_M+h)}{\psi_2(r_M+h)}\frac{\frac{\psi_1(r_M)}{\psi_1(r_M+h)}-C}{-\frac{\psi_2(r_M)}{\psi_2(r_M+h)}+C}. \tag{3.66}$$

Looking at the asymptotic form of the functions again, c_2/c_1 can be related to the actual short-range phase φ that according to Equations (3.22) and (3.47) characterizes the solution at $r\to 0$ as $\sin(1/r+\varphi)$.

$$\psi(r) = c_1\psi_1(r)+c_2\psi_2(r), \tag{3.67}$$

$$\psi(r) \overset{r\to 0}{\longrightarrow} \sqrt{2/\pi}r\left(c_1\sin(1/r)+c_2\cos(1/r)\right) \tag{3.68}$$

we set $c_1=\cos\delta$ and $c_2=\sin\delta$ to obtain

$$\begin{aligned}\psi(r) &\overset{r\to 0}{\longrightarrow} \sqrt{2/\pi}r\left(\cos\delta\,\sin(1/r)+\sin\delta\,\cos(1/r)\right)\\ &= \sqrt{2/\pi}r\left(\sin(1/r+\delta)\right),\end{aligned} \tag{3.69}$$

$$\varphi = \delta=\arctan(c_2/c_1) \tag{3.70}$$

Note that for the evaluation of $\psi_i(r_M+h)$ in Equation (3.66) both functions should start with the same amplitude at $r_{\min}$, which is secured by using $\cos\delta$ and $\sin\delta$ as coefficients in Equation (3.49) instead of 1 and $\tan\delta$.

The phase φ is given in the interval $[-\pi/2,\pi/2]$. Actually, $\varphi(E)$ is monotonically increasing in E and between two eigenenergies $\phi(E)$ increases by π. Because we calculate the tangent and then apply the arcus tangent, jumps occur at certain energies. One can remove these jumps by adding π to the function on the right side of the jump. If done so, the short-range phase can be plotted as a function of energy like in Figure 3.4. One can observe in Figure 3.4b that for higher partial waves the

phase increases in well defined steps. This can be explained by the height of the centrifugal barrier, which can be estimated as $(l(l+1))^2/4\ E^*$ in the characteristic unit of energy for atom-ion interaction. In the ultracold regime the centrifugal barrier for large l is much higher than typical particle energies (for $l = 10$ it is $3000E^*$). The eigenstates at energies larger than zero are trap states located on the right of the centrifugal barrier. Tunneling through the centrifugal barrier is very weak and therefore the molecular part of the wavefunction is strongly suppressed. The trap part of the wavefunction is not sensitive to the short-range phase, so the eigenenergy does not depend on it. Reversely the phase does not depend on energy. On the other hand, the phase must increase by π between two eigenenergies and this is why the steps occur. The phase is independent of energy on the plateaus between the steps. For energies higher than the centrifugal barrier the steps vanish because the short range part of the wavefunction is no longer suppressed by the barrier. This can be seen for the example of $l = 4$ where the centrifugal barrier is small ($100E^*$).

3.6.2 Choice of Species and Computational Basis

This section addresses the question which atom and ion species are to be used to perform explicit numerical simulations on the system. Our choice of the species of the atom and the ion is motivated by ongoing experiments in Innsbruck using Barium ions and Rubidium atoms for ultracold collisions [9]. We use the isotopes ^{87}Rb and ^{135}Ba$^+$, since their atomic levels have a hyperfine structure and qubit states are to be encoded in hyperfine states. In this section we also choose the computational basis out of the manifold of hyperfine states and motivate the choice. The hyperfine structure of the atom and ion isotopes is depicted schematically in Figure 3.5. Both structures are similar, because the nuclear spins $i_{a,i} = 3/2$ are equal. The hyperfine splitting energies are $E_i^{HF}/h = 7.29 \times 10^9$Hz for Barium and $E_a^{HF}/h = 6.83 \times 10^9$Hz for Rubidium (see e.g.[28] and [19] for isotope information).

Collisions that scatter atom and ion out of the computational basis are a loss mechanism and result in failure of any gate process. Furthermore, if a phase gate is desired, collisions that change the qubit state are to be avoided. We assign the

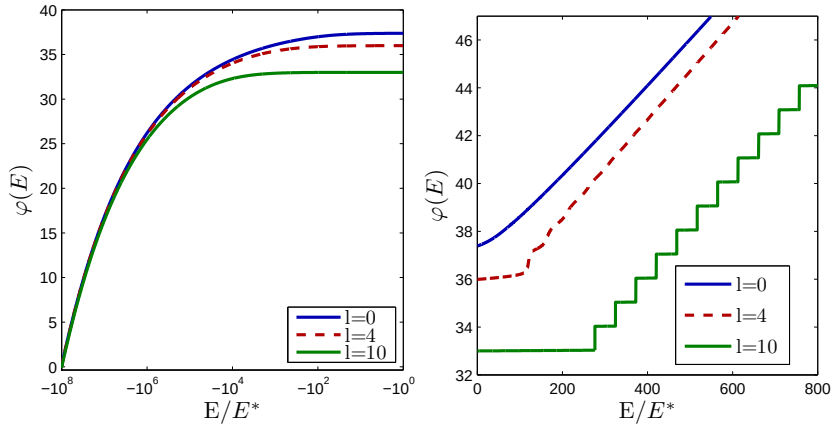

(a) (b)

Figure 3.4: Short-range phase as a function of energy for the partial waves $l = 0$, $l = 4$ and $l = 10$. The energy axis is split into negative (left panel) and positive (right panel). Once the quantum-defect parameter φ_0 is specified, one can find a eigenenergy at $\varphi(E) = \varphi_0 + n\pi$. The bound states level spacing (negative energies) increases exponentially the deeper the state is bound. The level spacing in the trap part of the potential (positive energies) becomes equidistant (harmonic trap). For higher partial waves the energy is independent on the short-range phase, since $\varphi(E)$ shows a step structure.

qubit states $|0\rangle_{i,a}$ and $|1\rangle_{i,a}$ to hyperfine states of atom and ion in such a way that the combined two-qubit computational basis states $|00\rangle_{i,a}, |01\rangle_{i,a}, |10\rangle_{i,a}$ and $|11\rangle_{i,a}$ are each coupled to the smallest possible manifold of non-computational basis states. For that purpose, it is convenient to pick the states with lowest and highest energy in Figure 3.5 for the ion as well as for the atom:

$$\begin{aligned} |0\rangle_{i,a} &= |f_{i,a} = 1, m_{f_{i,a}} = 1\rangle_{i,a} \\ |1\rangle_{i,a} &= |f_{i,a} = 2, m_{f_{i,a}} = 2\rangle_{i,a}. \end{aligned} \tag{3.71}$$

In the present setup, without magnetic field, m_f is the quantum number of the projection of the total spin f on the z axis, which is the axis of trap displacement and the symmetry axis. The total projection quantum number $m_f = m_{f_i} + m_{f_a}$

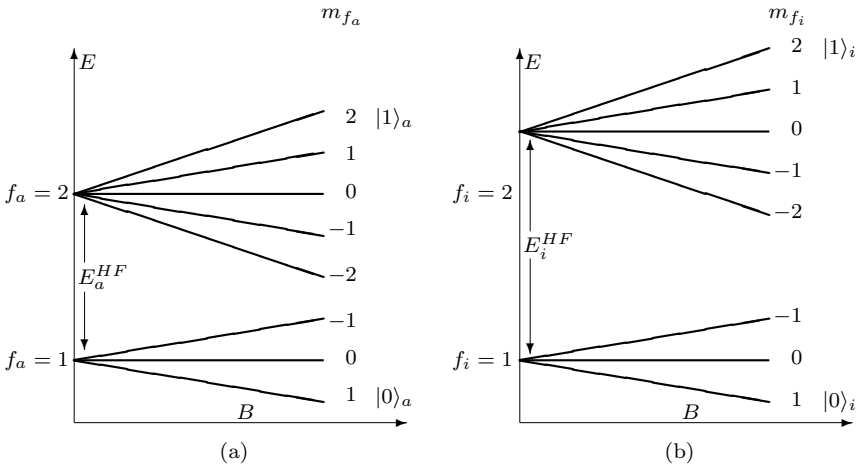

Figure 3.5: Hyperfine structure of the atom (left) and of the ion (right), ^{87}Rb and $^{135}Ba^{+}$ both have a nuclear spin of $i_{a,i} = 3/2$, the hyperfine splitting energies are different.

is conserved, so in principle a channel can be coupled to another channel if their m_f is the same. Two qubit channels are constructed by combining single qubit hyperfine states. We name a channel according to its quantum numbers in the order $|f_i, m_{f_i}, f_a, m_{f_a}\rangle$:

$$\begin{aligned}
|00\rangle &= |f_i{=}1, m_{f_i}{=}1, f_a{=}1, m_{f_a}{=}1\rangle = |1,1,1,1\rangle \qquad m_f = 2 \\
|01\rangle &= |f_i{=}1, m_{f_i}{=}1, f_a{=}2, m_{f_a}{=}2\rangle = |1,1,2,2\rangle \qquad m_f = 3 \\
|10\rangle &= |f_i{=}2, m_{f_i}{=}2, f_a{=}1, m_{f_a}{=}1\rangle = |2,2,1,1\rangle \qquad m_f = 3 \\
|11\rangle &= |f_i{=}2, m_{f_i}{=}2, f_a{=}2, m_{f_a}{=}2\rangle = |2,2,2,2\rangle \qquad m_f = 4.
\end{aligned} \tag{3.72}$$

For this choice of hyperfine qubits the $|11\rangle$ channel is completely isolated because no other channel has a total spin of $m_f = 4$, while the other qubit states can be influenced by other channels.

The channels with $m_f = 2$ (including the $|00\rangle$ computational state) are:

$$\begin{aligned}
&|1,1,1,1\rangle \quad |1,1,2,1\rangle \quad |2,1,1,1\rangle \quad |2,1,2,1\rangle \\
&|1,0,2,2\rangle \quad |2,2,1,0\rangle \quad |2,0,2,2\rangle \quad |2,2,2,0\rangle.
\end{aligned} \tag{3.73}$$

For an ultracold collision of an atom and an ion that are prepared in the incoming

channel $|00\rangle$, all seven other $m_f = 2$ channels are closed. That means the threshold energy of their potentials lies above the threshold of the incoming channel, because of the hyperfine splitting energy (of the atom or the ion or both). This hyperfine splitting is much larger than all kinetic and potential energies considered in an ultracold collision and therefore only bound states of closed channels can influence the dynamics of the open channel by resonances.

For $m_f = 3$ the channels (including the $|01\rangle$ and $|10\rangle$ computational states) are

$$|1,1,2,2\rangle \quad |2,2,1,1\rangle \quad |2,1,2,2\rangle \quad |2,2,2,1\rangle, \tag{3.74}$$

note here that $|01\rangle$ and $|10\rangle$ are in principle coupled. The threshold energy of the $|10\rangle$ potential is shifted by the difference of the hyperfine splittings $E_i^{HF} - E_a^{HF} > 0$ with respect to the $|01\rangle$ threshold. Therefore if atom and ion are prepared in the $|10\rangle$ channel, there is a second open channel. Not only the molecular bound states of this channel, but also vibrational states, can lead to resonances between the two open channels, resulting in possible spin-changing processes. In a spin-changing collision, m_i and m_a change while m_f is conserved. Since vibrational states have a smaller level-spacing than molecular states, it is not unlikely that one vibrational state of the $|01\rangle$ channel hits the energy of any state of the $|10\rangle$ channel. This definitely limits the use of a single channel picture of four non coupled qubit channels, though a single channel model can be applied in the special case of similar singlet and triplet scattering lengths. This model is described in Section 3.7.

3.6.3 Parametrization of the Quantum-Defect Matrix $\mathbf{Y}$

Once the hyperfine states are specified, one can parametrize the quantum-defect matrix at short distances $r_0 \lesssim r \ll R^*$. We explain this by giving the example of the four coupled channels of the $m_f = 3$ subspace for the $^{135}Ba^+$ ion and the ^{87}Rb atom from Section 3.6.2. We begin with Table 3.1, listing the quantum numbers of the states of this subspace. The four states in hyperfine representation are found on the left side and the four states in is representation are on the right side. The hyperfine states are labeled such that β_1, β_2 correspond to the qubit channels $|01\rangle$,$|10\rangle$, respectively. Note that in the is basis, one channel has the total electron spin $s = 0$ and therefore is a singlet state, while the other three channels are triplet

	f_i	m_{f_i}	f_a	m_{f_a}		i	s	f	m_f
β_1)	1	1	2	2	γ_1)	3	0	3	3
β_2)	2	2	1	1	γ_2)	3	1	3	3
β_3)	2	1	2	2	γ_3)	3	1	4	3
β_4)	2	2	2	1	γ_4)	3	1	4	3

Table 3.1: Quantum numbers of the four states of the $m_f = 3$ subspace for $^{135}Ba^+$ ion and ^{87}Rb atom. The left(right) block shows the states in hyperfine (is) representation. Note that the state β_i is not equal to γ_i, but a linear combination of all the γ channels. This linear combination is determined by the frame transformation $U_{\beta\gamma}$.

states with $s = 1$. Accordingly, the quantum-defect matrix in is representation has the form

$$\mathbf{Y}^{(is)} \equiv \begin{pmatrix} a_s^{-1} & 0 & 0 & 0 \\ 0 & a_t^{-1} & 0 & 0 \\ 0 & 0 & a_t^{-1} & 0 \\ 0 & 0 & 0 & a_t^{-1} \end{pmatrix}. \tag{3.75}$$

The frame transformation described in Section 3.2.2 yields the quantum-defect matrix in the hyperfine basis

$$\mathbf{Y} = \mathbf{U}\mathbf{Y}^{(is)}\mathbf{U} = \begin{pmatrix} \frac{3}{8a_s} + \frac{5}{8a_t} & \frac{3}{8a_s} - \frac{3}{8a_t} & -\frac{\sqrt{3}}{8a_s} + \frac{\sqrt{3}}{8a_t} & -\frac{\sqrt{3}}{8a_s} + \frac{\sqrt{3}}{8a_t} \\ \frac{3}{8a_s} - \frac{3}{8a_t} & \frac{3}{8a_s} + \frac{5}{8a_t} & -\frac{\sqrt{3}}{8a_s} + \frac{\sqrt{3}}{8a_t} & -\frac{\sqrt{3}}{8a_s} + \frac{\sqrt{3}}{8a_t} \\ -\frac{\sqrt{3}}{8a_s} + \frac{\sqrt{3}}{8a_t} & -\frac{\sqrt{3}}{8a_s} + \frac{\sqrt{3}}{8a_t} & \frac{1}{8a_s} + \frac{7}{8a_t} & \frac{1}{8a_s} - \frac{1}{8a_t} \\ -\frac{\sqrt{3}}{8a_s} + \frac{\sqrt{3}}{8a_t} & -\frac{\sqrt{3}}{8a_s} + \frac{\sqrt{3}}{8a_t} & \frac{1}{8a_s} - \frac{1}{8a_t} & \frac{1}{8a_s} + \frac{7}{8a_t} \end{pmatrix}. \tag{3.76}$$

We observe that the off-diagonal elements that represent the coupling between the channels are small for similar singlet and triplet scattering lengths. They vanish for $a_s \equiv a_t$.

This procedure is repeated analogously for the $m_f = 2$ subspace, including the $|00\rangle$ channel. The channel $|11\rangle$ is the only state in the subspace $m_f = 4$ and it is a triplet state in is representation. The quantum-defect matrix $\mathbf{Y} = 1/a_t$ in that case is a scalar.

3.7 Single Channel Models for Four Qubit Channels for the Ba^+ Rb System

In this section we present and discuss a single channel model for the collision of a $^{135}Ba^+$ ion and a ^{87}Rb atom with the qubit states specified in Section 3.6.2. The choice of species must be made in order to perform concrete numerical calculations. It does not restrict the applicability of the developed ideas to other systems. One single channel model is created for each qubit channel $|00\rangle$, $|01\rangle$, $|10\rangle$ and $|11\rangle$ as specified in Section 3.6.2. Here, we only consider the special case of $d = 0$ in the calculation of eigenenergies and states. This is justified, since the general solution for $d \neq 0$ can be written as a linear combination of the $d = 0$ states given in Equation (3.18). If a mixing of channel states occurs for $d = 0$, then it is also true for the $d \neq 0$ general case.

The multichannel eigenvalue condition $\left|\mathbf{Y} + \tan \boldsymbol{\nu}^l(E)\right| = 0$ (Equation (3.15)) is solved to find the $d = 0$ eigenenergies of the multichannel problem. The quantum-defect matrix $\mathbf{Y}$ is determined as in Section 3.6.3 where specific short-range phases are assumed. The diagonal elements of the matrix $\boldsymbol{\nu}^l(E) = (\nu_i^l(E)\delta_{ij})$ equal the short-range phase $\nu_i^l(E) = \varphi^l(E - E_i^\infty)$ determined in Section 3.6.1. The energy splitting between the asymptotic channels enters as E_i^∞. The matrix $\mathbf{A}$ is determined by Equation (3.14). $\mathbf{A}$ is given by the null space of $\left[\mathbf{Y} + \tan \nu^l(E)\right]$. Typically, for an eigenvalue E_n determined from Equation (3.15), only a single vector of $\mathbf{A}$ is nonzero and this vector determines the eigenstate. This vector of $\mathbf{A}$ is denoted by $\mathbf{b}_n$ and gives the mixing of the asymptotic hyperfine states. For the case of four channels we give an example

$$\mathbf{b}_n = \begin{pmatrix} 0.9999 \\ 10^{-4} \\ 10^{-10} \\ 10^{-9} \end{pmatrix} \quad \begin{matrix} \} \\ \left.\begin{matrix} \\ \\ \\ \end{matrix}\right\} \end{matrix} \quad \begin{matrix} \rightarrow \text{dominant channel} \\ \\ \\ \rightarrow \text{small admixture of other channels} \end{matrix} \tag{3.77}$$

in which one channel is dominant and therefore decoupled. The other channels disturb the state with a maximal admixture of 10^{-4}. If all states $\{\mathbf{b}_n\}$ have this maximal admixture, a single channel model can be formulated that has the accuracy of 10^{-4}. In this case we determine the short-range phase corresponding

to the energy of the lowest vibrational state with the help of the monotonical function $\varphi^l(E)$ (see Figure 3.4). This phase defines the effective short range phase φ_0^l for the single channel model. If this phase is used in a single channel model as a quantum-defect parameter for the wavefunctions, all multichannel eigenenergies (found with Equation (3.15)) are reproduced by this model with a certain accuracy. The single channel eigenenergies are found at the phases $\varphi_0^l + n\pi$ in the function $\varphi(E)$. Here we assume, that the quantum defect parameter does not depend on energy. We verify this statement by comparing the multichannel eigenenergies with the single channel eigenenergies in the regime we are interested in.

This procedure is repeated for every partial wave, which in general leads to an l-dependent quantum-defect parameter $\varphi_0(l)$. We only need to find $\varphi_0(l)$ up to a certain angular momentum threshold l_0 where the centrifugal barrier becomes much higher than the considered particle energies. For larger l the energies become independent of the short-range phase and we can set the phase to an arbitrary value, still obtaining the correct states and energies. If $\mathbf{b}_n$ on the other hand is not dominated by one channel, for example

$$\mathbf{b}_n = \left.\begin{pmatrix} 0.510 \\ 0.481 \\ 0.009 \\ 10^{-9} \end{pmatrix}\right\} \begin{array}{l} \rightarrow \text{two completely mixed channels} \\ \\ \rightarrow \text{two channels slightly disturb} \end{array} \tag{3.78}$$

then a mixing with other channels takes place and a single channel effective description is excluded.

Two opposite situations for singlet and triplet scattering lengths are discussed in the following. First we assume that a_s and a_t have opposite signs, for example $a_s = -R^*$ and $a_t = R^*$. In the second situation we assume similar a_s and a_t, for example $a_s = 0.8R^*$ and $a_t = 1R^*$. When the singlet and triplet scattering length are equal ($a_s = a_t$), the quantum-defect matrix is diagonal in is representation as well as in the hyperfine basis. No couplings occur and also the eigenenergies and eigenstates are the same for different channels.

3.7.1 Opposite Sign of Singlet and Triplet Scattering Length

We calculate multichannel energies and states for the example $a_s = -R^*$ and $a_t = R^*$. An effective single channel model for the $|00\rangle$ channel can be extracted. The seven closed channels disturb the incoming channel wavefunction with terms of the order of 10^{-5} to 10^{-6} or lower, depending on the partial wave. The $|11\rangle$ channel is decoupled in any case; since $|11\rangle$ is a triplet state in the is basis, the corresponding single channel short-range phase is calculated from $\tan\varphi_0 = -R^*/a_t$, which yields $\varphi_0 = -\pi/4 \hat{=} 3/2\pi$ for all partial waves.

The remaining two computational basis states $|01\rangle$ and $|10\rangle$ are decoupled from the two non-computational basis states of the corresponding $m_f = 3$ subspace, but $|01\rangle$ and $|10\rangle$ are mixed. For the energetically lower lying state $|01\rangle$ the mixing is not very strong ($\sim 10^{-4}$), since the bound states of the higher energetic channel $|10\rangle$ that could influence the states of $|01\rangle$ have a much larger level spacing than the vibrational states. A single channel model for $|10\rangle$ is excluded, since in the energy range considered many vibrational trap states of $|01\rangle$ influence the $|10\rangle$ channel and the two cannot be separated.

In this case one can either perform the full four channel calculation or create an effective two-channel model that includes the couplings between $|01\rangle$ and $|10\rangle$ channels. We do not consider this more complicated case in this thesis. However, the case of opposite scattering lengths is very interesting, since it leads to large differences in the dynamics that can be used for fast gates, and this problem will be addressed in the future.

Controlling the two-channel dynamics simultaneously offers the possibility of a swap gate as well as a phase gate. The corresponding truth tables are

$$\begin{aligned} |00\rangle &\overset{\text{Swap Gate}}{\longrightarrow} |00\rangle \\ |01\rangle &\longrightarrow |10\rangle \\ |10\rangle &\longrightarrow |01\rangle \\ |11\rangle &\longrightarrow |11\rangle, \end{aligned} \tag{3.79}$$

$$\begin{aligned} |00\rangle &\xrightarrow{\text{Phase Gate}} |00\rangle \\ |01\rangle &\longrightarrow |01\rangle \\ |10\rangle &\longrightarrow |10\rangle \\ |11\rangle &\longrightarrow -|11\rangle. \end{aligned} \tag{3.80}$$

The swapping of $|01\rangle$ to $|10\rangle$ states while $|11\rangle$ and $|00\rangle$ remain unchanged is contrasted to the phase gate that isolates the two-qubit states and gives a phase only to the $|11\rangle$ channel. The phase gate in combination with single-qubit transformations is a universal gate for quantum computing. The square root of the swap gate is an entangling two-qubit gate as well [29], and therefore universal in combination with single-qubit gates.

3.7.2 Similar Singlet and Triplet Scattering Lengths

In the situation of similar singlet and triplet scattering lengths one can find an effective model of four isolated channels for the qubit states. Since the channels are isolated one can attempt a two-qubit phase gate (see Equation (3.80)). The admixture of other channels depends on the structure of the levels. The level spacing of the trap states is dependent on the trapping frequency, while the hyperfine splitting energy that shifts the potential curves with respect to each other depends on atom and ion species. If, in the multichannel picture, two states occur that have very similar energy, there is a large possibility that a channel mixing takes place in the corresponding states. On the other hand, if the levels in the multichannel picture are well separated, it is more likely that the corresponding states can each be assigned to isolated channels. This also has to be investigated for the specific example.

The example we choose is $a_s = 0.8R^*$ and $a_t = 1R^*$. The energy dependence of the short-range phase in the energy range typical for ultracold collisions is negligible. The effective phase depends on the partial wave l(see Figure 3.6). the differences between the channels are not large, because a_s and a_t are similar. The $|11\rangle$ channel is decoupled by definition and the $|00\rangle$ channel also decouples, since none of the bound state energies of the seven closed channels meet the levels of

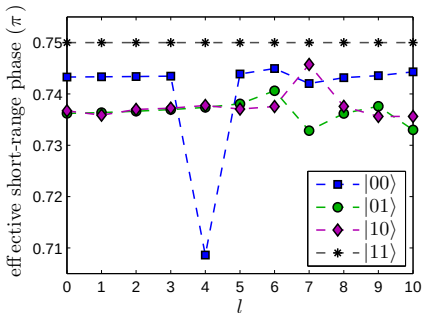

Figure 3.6: Effective single channel short-range phases for $0 \leq l \leq 10$ found for a ^{135}Ba^{+}-^{87}Rb collision in traps with $\omega \approx 2\pi \times 26.9$kHz. The singlet and triplet scattering lengths are assumed as $a_s = 0.8R^*$ and $a_t = 1R^*$. For $l > 10$ the phase is arbitrary in the energy regime $E \lesssim 80\hbar\omega$. The phase for $l = 4$ in the $|00\rangle$ channel differs from the phases for the other partial waves, but indeed produces the respective multichannel energies very accurately.

the open channel. The admixture of the closed channels is of the order of 10^{-6} to 10^{-8}. If the particles are prepared in the $|01\rangle$ channel, all other channels of the $m_f = 3$ subspace are closed. We find a single channel model for the $|01\rangle$ channel, and the maximal disturbance of the $|01\rangle$ states by other channels is of the order of 10^{-4}, which mostly originates from deep bound states of the $|10\rangle$ channel. The single channel model for the $|10\rangle$ channel is the least accurate of the four. The states of the $|10\rangle$ channel are mixed with high vibrational states of the $|01\rangle$ channel typically to the order of 10^{-3}. The maximal admixture found is 1.45×10^{-2} for the state with the energy $E = 118E^*$ of the partial wave $l = 4$. This state is included in the set of basis functions used both for calculation of the energy spectrum in Section 3.5 and for time evolution in Chapters 4 and 5. The admixture of 1.45×10^{-2} gives an estimation of the error of the effective single channel model describing the controlled collision of a ^{135}Ba^{+} ion and a ^{87}Rb atom in $\omega \approx 2\pi \times 26.9$kHz traps. This model is used to demonstrate a phase gate with the given system provided that scattering lengths are similar. The ideas presented here can in principle be applied on any alkali atom plus alkaline earth ion system.

4 Controlled Atom-Ion Collision in a Single Channel Model

4.1 Time Dependent Problem

In this chapter we study the dynamics of the ultracold atom-ion collision in a single channel model. In Chapter 3 the time independent Schrödinger equation was solved in order to find eigenstates and eigenvalues. The problem now becomes time dependent. The time evolution of a state $|\Psi\rangle$ is governed by the time dependent Schrödinger equation

$$i\hbar\frac{\partial}{\partial t}|\Psi(t)\rangle = H(t)\,|\Psi(t)\rangle. \tag{4.1}$$

There are many ways to introduce time dependency in the collision. For example, the trapping frequencies could change in time, or one could apply a time dependent magnetic field $B(t)$ to change the scattering lengths dynamically. In this context Feshbach resonances provide an opportunity to control the outcome of a collision. In this work, the quantity we change in time will be the trap displacement $d(t)$ to make use of trap-induced shape resonances. Since this approach uses inherent features of the system, it is particularly simple and interesting [1].

A quantum gate can be performed by bringing the ion trap close to the atom trap with a certain speed, and by finally separating them again. The distance $d(t)$ between the trapping potentials is the only parameter to be controlled. For an illustration of this controlled collision see Figure 2.1.

[1] It is possible to further control the interaction by additional external (magnetic) fields. This more complicated approach is not followed in this thesis.

4.2 Time Evolution Using a Basis

We decided to use the basis of eigenfunctions for $d = 0$ for time evolution. At r approaching zero the potential becomes very deep, which causes the wavefunctions to oscillate very fast. The required spatial resolution for following these oscillations is too high to reasonably apply time evolution in position or momentum representation. Instead, one set of basis functions $\{|\Psi_k^{(0)}\rangle\}$ is calculated as described in Section 3.4 for $d = 0$. These functions are used to decompose an arbitrary state, which is then characterized by a set of coefficients c_k (see Section 3.5). Schrödinger's equation translates to a set of differential equations for these coefficients. An alternative basis would be an adiabatic one, consisting of the instantaneous (time dependent) eigenstates of the Hamiltonian. One advantage of an adiabatic basis would be that fewer states are required for accurate numerical time evolution, since only the lowest energy states are populated. On the other hand, the differential equations for the coefficients are more complicated, both in the derivation and the final form. Thus we chose the time independent $|\Psi_k^{(0)}\rangle$ basis. The basis functions $|\Psi_k^{(0)}\rangle$ are sorted according to their eigenenergy $E_k^{(0)}$ in ascending order.

In the framework of quantum-defect theory the interaction potential is replaced with $-C_4/r^4$. Since the functions are singular at the origin in this case, they are truncated at a minimal distance $r_{\min}$. If $r_{\min}$ is chosen small enough, the produced error is small, because the radial functions amplitude is proportional to r at small distance. In the effective single channel model developed in Chapter 3, a boundary condition—the short-range phase—is imposed on the wavefunction at $r_{\min}$. Figure 4.1a shows two typical radial functions for $d = 0$. One can see that states corresponding to high energy E_k, e.g. trap states, are localized far away from the origin $r = 0$. States with low or negative energy, e.g. molecular states, have higher probability amplitude at small r.For larger d, the eigenstates are similar to harmonic oscillator states, because the atom and the ion are localized in their separated traps. In Figure 4.1b the trap ground state for $d = 1.5$ is depicted. In the relative coordinate the total wavepacket is then localized around the distance $r = d$. A large number of $d = 0$ basis functions are needed to decompose these

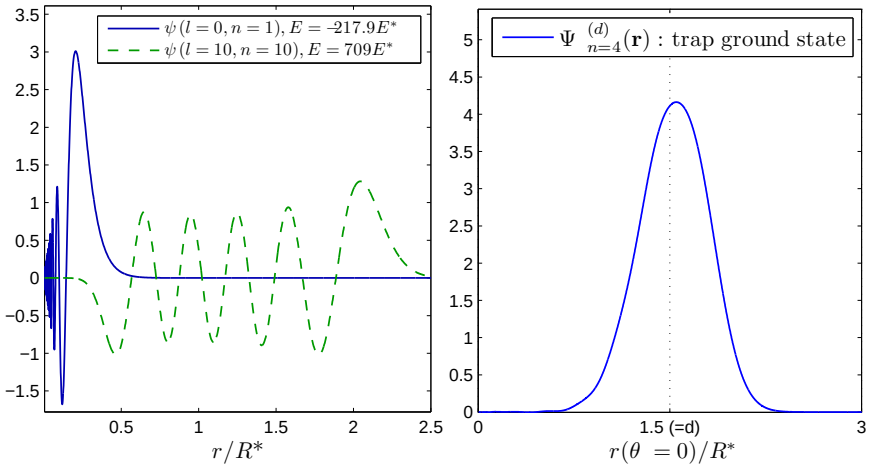

Figure 4.1: Typical radial wavefunctions for $d = 0$ (left panel) and $d > 0$ (right panel). A molecular state is located at small r, a vibrational state reaches to larger r and is similar to a shifted harmonic oscillator state. For large angular momenta the short-range part is suppressed. The wavefunctions of the trap vibrational ground state for $d = 1.5R^*$ (right panel) is located around the trap distance d. For the plot r goes in the z-direction ($\theta = 0$). To decompose the states for large d, many states for $d = 0$ are needed.

harmonic oscillator states for large d with a small truncation error.

4.2.1 Differential Equation for the Coefficients c_k

Since the trap distance $d(t)$ is a function of time, the Hamilton operator becomes time dependent:

$$H^{(d)}_{\mathrm{rel}}(t) = H^{(0)}_{\mathrm{rel}} + \frac{1}{2}\mu\omega^2 d(t)^2 - \mu\omega^2 d(t) z. \tag{4.2}$$

The wavefunction is decomposed in the basis

$$|\Psi(t)\rangle = \sum_k c_k(t)|\Psi^{(0)}_k\rangle. \tag{4.3}$$

We substitute this into Schrödinger's equation, which thereby translates to a coupled differential equation for the coefficients c_k:

$$i\hbar\frac{\mathrm{d}}{\mathrm{d}t}|\Psi(t)\rangle = H_{\mathrm{rel}}^{(d)}(t)|\Psi(t)\rangle,$$
$$i\hbar\sum_k \frac{\mathrm{d}}{\mathrm{d}t}c_k|\Psi_k^{(0)}\rangle = \sum_k c_k H_{\mathrm{rel}}^{(d)}(t)|\Psi_k^{(0)}\rangle,$$

we project on $\langle\Psi_{k'}^{(0)}|$ to obtain

$$i\hbar\frac{\mathrm{d}}{\mathrm{d}t}c_{k'} = \sum_k c_k\left[\left(E_{k'}^{(0)} + \frac{1}{2}\mu\omega^2 d(t)^2\right)\delta_{k',k} - \mu\omega^2 d(t) M_{k'k}\right]. \tag{4.4}$$

Here, $M_{k'k} = \langle\Psi_{k'}^{(0)}|z|\Psi_k^{(0)}\rangle$ is the dipole matrix element (see also Section 3.5). In dimensionless units of E^* and R^* (the time is given in units of $\hbar/E^*$) Equation (4.4) becomes

$$i\frac{\mathrm{d}}{\mathrm{d}t}c_{k'} = \sum_k c_k\left[\left(E_{k'}^{(0)} + \alpha d(t)^2\right)\delta_{k',k} - 2\alpha d(t) M_{k'k}\right], \tag{4.5}$$

with $\alpha = (\hbar\omega/2E^*)^2$. The set of basis functions and therefore also the set of differential equations is infinitely large but will be truncated at a finite value N corresponding to the number of numerically calculated basis functions. The independence of N with respect to the time evolution has to be tested carefully to make sure that the basis is sufficiently large and to exclude the possible influence of truncated functions on the dynamics of the system (see e.g. Appendix A.4). That is, the population of highest-n basis states must (within a certain error bound) vanish for all times.

The farther separated the traps are (the larger d is), the more $|\Psi_k^{(0)}\rangle$ states contribute to the trap ground state, which for our simulations is the initial state for time evolution. Therefore the application of the $d = 0$ basis is limited. Depending on the maximum value of $d(t)$, the size of the basis has to be chosen as small as possible, since the computational effort strongly increases with growing N.

4.3 Features of the Dynamics

4.3.1 The Landau-Zener Formula

The Landau-Zener theory deals with the time dependent Schrödinger equation of two coupled states whose energy levels are crossing. The same situation is called a resonance in Section 2.5. Actually, the levels form an anticrossing or avoided crossing as depicted in Figures 2.5 and 4.2. We consider a situation in which each particle is prepared in the ground state of its trap. We decrease the distance d between the traps with a constant speed and thereby pass an avoided crossing. The Landau-Zener formula

$$P_{\mathrm{na}} = \exp\left(-2\pi \frac{|\langle\Psi_1|H|\Psi_2\rangle|^2}{\hbar|\dot{d}\,\partial E_{12}/\partial d|}\right) \tag{4.6}$$

gives a quantitative statement of the probability of nonadiabatic (also called diabatic) passage of the avoided crossing that depends on the velocity $\dot{d}$, the slope of the adiabatic energy curves $\partial E/\partial d$ and the strength of the coupling given by the matrix element $H_{12} = \langle\Psi_1|H|\Psi_2\rangle$. In the following section we compare the numerical time evolution to the Landau-Zener formula. For the atom-ion system this formula can be specialized in such a way that only quantities directly available from the energy spectrum are used. This is done in [10]. Here, $|\Psi_1\rangle = |\Psi_{\mathrm{vib}}\rangle$ is an unbound diatomic state (vibrational state) and $|\Psi_2\rangle = |\Psi_{\mathrm{mol}}\rangle$ is a molecular state. First, the energy gap $\Delta E = 2\,\langle\Psi_{\mathrm{mol}}|H|\Psi_{\mathrm{vib}}\rangle$ can be related to the coupling matrix element. Since the molecular state is concentrated around $r = 0$, its energy varies approximately as $E_{\mathrm{mol}}(d) = \langle\Psi_{\mathrm{mol}}|H|\Psi_{\mathrm{mol}}\rangle \approx E^{(0)} + 1/2\mu\omega^2 d^2$. Therefore, $\partial E_{\mathrm{mol}}/\partial d = \langle\Psi_{\mathrm{mol}}|\partial H(d)/\partial d|\Psi_{\mathrm{mol}}\rangle \approx \mu\omega^2 d$ can be estimated. With $\partial E_{\mathrm{vib}}/\partial d \approx 0$, Equation (4.6) can be rewritten as

$$P_{\mathrm{na}} = \exp\left(-\frac{\pi}{2}\frac{(\Delta E)^2}{\hbar|\dot{d}|\mu\omega^2 d}\right). \tag{4.7}$$

For further reading about the original Landau-Zener formula and its derivation we recommend [22]. Details on the application on atom-ion collision can be found in [10].

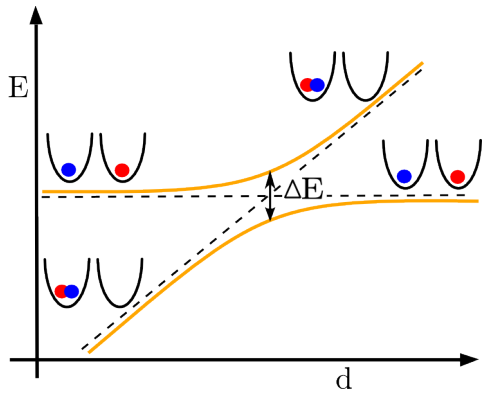

Figure 4.2: Schematic drawing of an avoided crossing of a vibrational state and a molecular state. The coupling strength can be related to the energy splitting ΔE. Starting at the unbound state (separated particles) at large d and decreasing d, in an adiabatic (slow) process we will stay in the adiabatic eigenstate and reach the molecular state (connected particles) at small d along the solid line in the energy diagram. If the same process is executed with a fast speed, we will follow the diabatic curve (dashed line) and reach the unbound trap state at small d. This process is reversible.

4.3.2 Numerical Simulation of the Traverse of an Avoided Crossing

In order to understand the basic features of the dynamics around an avoided crossing, numerical calculations are performed, assuming typical particle masses and trapping frequencies. The dimensionless parameter of the radial equation in our simulation is set to $\alpha = 146.046$. This parameter corresponds to a specific trapping frequency for a given atom-ion pairing, as α is determined by the ratio of characteristic energy of the interaction potential to the oscillator energy of the trap. The required trapping frequencies are realistic for typical trapped particles ($\omega \approx 2\pi\times$27kHz for $^{135}Ba^{+}+^{87}Rb$ and $\omega \approx 2\pi \times$ 100kHz for $^{40}Ca^{+}+^{87}Rb$), even though in the laboratory generally $\omega_i \neq \omega_a$.

In the framework of quantum-defect theory, a short-range phase φ is imposed

on the eigenfunctions as a boundary condition. In the calculations presented in the present section this phase is set to $\varphi = -\pi/4$. This corresponds to a scattering length of $a = 1\,R^*$, according to Equation (3.25). Scattering lengths usually are of the order of R^* (see [7]). The same short-range phase and α correspond to the channel $|11\rangle$ in the two-qubit phase gate presented in Chapter 5.

Using these parameters we investigate a trap-induced shape resonance at $d = 1.119R^*$, marked in the energy spectrum in Figure 4.3a. This particular resonance is chosen because it is reasonably strong (for larger d the resonances get weaker) and on the other hand we still can see the typical behavior of constant energy of the trap vibrational state, which is not so clear in the inner crossing at $d \sim 0.7R^*$. Further, we want to compare the numerical results to the Landau-Zener formula which requires a linear d-dependence of the energy curves. The deviations from a linear slope of the energy curves are not too large.

In the simulated process the trap distance varies linearly in time, going from large to small d. The passage of the resonance is simulated with three different velocities $\dot{d}$: $\dot{d} = 0.01R^*/(\hbar/E^*)$ (slow), $\dot{d} = 0.5R^*/(\hbar/E^*)$ (intermediate) and $\dot{d} = 10R^*/(\hbar/E^*)$ (fast). The characteristic unit of velocity is $R^*/(\hbar/E^*)$. For the $^{135}Ba^+$-^{87}Rb system this unit corresponds to 2.05mm/s, while for lighter particles, it corresponds to larger velocities, e.g. for the Ca^+-Na system $1R^*\hbar/E^* =$ 14.11 mm/s.

For the results presented here we used the Matlab routine *ode45* to solve the differential equations (4.5). The solver *ode45* has a built in relative error tolerance of 10^{-3} and an absolute error tolerance of 10^{-6}, which is sufficient for the sake of demonstration, but can also be adjusted.

Figure 4.3b zooms in on the investigated avoided crossing. Figure 4.3a shows the position of this crossing in the energy spectrum and illustrates the numeration of the energy eigenstates. The adiabatic eigenstates in the spectrum are labeled according to their energy in ascending order with the numbers $n = 1, 2, \ldots, N$. These adiabatic eigenstates change from molecular to unbound states at avoided crossings. For example the state $n = 4$ at $d = 0$ is a molecular bound state with the energy $\approx -2\hbar\omega$, Following the energy curve to larger d, a large avoided crossing with state $n = 5$ is reached at $d \approx 0.7R^*$. On the right side of this

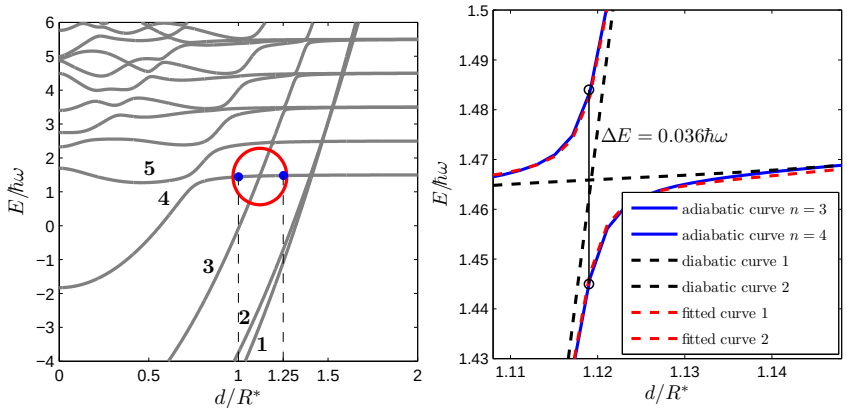

(a) (b)

Figure 4.3: The left panel shows the numbering of the adiabatic energy eigenstates in the energy spectrum for the short-range phase $\varphi = -\pi/4$, the circle marks the avoided crossing depicted in the right panel. Final and initial d for the numerical time evolution are marked. The initial state is $n = 3$ at $d = 1.25R^*$. The energy unit is $\hbar\omega$, where $\omega \approx 2\pi \times 27$kHz for the $^{135}Ba^+ + ^{87}Rb$ system.

crossing, the state $n = 4$ has the character of an unbound trap vibrational state; its energy stays approximately constant with increasing d. For even larger d state $n = 4$ meets state $n = 3$ in a second avoided crossing at $d \approx 1.2$. This avoided crossing is smaller and not resolved in Figure 4.3a and this is the resonance we investigate time evolution at. Passing this crossing, the eigenstate $n = 4$ becomes a molecular state again and $n = 3$ becomes the mentioned unbound diatomic state. This switching from bound to unbound states labeled by $n = 4$ is continued at the following avoided crossings.

We simulate the time evolution between the trap distances $d = 1.25R^*$ and $d = 1R^*$ (see Figure 4.3a). At both edges resonances are as far away as possible, so we expect it to be justified that the influence of resonances at these distances is negligible. We calculated the curvature of the adiabatic energy curves and they came out to be relatively low at $d = 1$ and $1.25R^*$, which affirms our assumption

that at these distances no resonance has a large influence. The initial state

$$|\Psi_{\text{ini}}\rangle = |\Psi_{n=3}^{(d=1.25)}\rangle \tag{4.8}$$

is $n = 3$ at $d = 1.25R^*$, which corresponds to the ground state in the trapping potential, which is an unbound diatomic state. After numerical time evolution the final state

$$|\Psi_{\text{fin}}\rangle = c_{\text{mol}}\,|\Psi_{\text{mol},n=3}^{(d=1)}\rangle + c_{\text{vib}}\,|\Psi_{\text{vib},n=4}^{(d=1)}\rangle + c_{\text{exc}}\,|\Psi_{\text{exc},n=5}^{(d=1)}\rangle + \ldots \tag{4.9}$$

is composed of a molecular state (mol) and a trap vibrational state (vib). Also excited states (exc) may be populated. The results of these simulations are illustrated in Figure 4.4.

We focus on the slow process first. The population of relevant states is shown in Figure 4.4a. Initially, at $d = 1.25R^*$, the trap ground state labeled with $n = 3$ is 100% populated. While sweeping over the resonance, a part of the population is passed over to the crossing molecular bound state. The final state of this slow process at $d = 1R^*$ is composed of the molecular bound state ($|c_{\text{mol}}|^2 = 0.33$) and of the unbound trap state ($|c_{\text{vib}}|^2 = 0.67$). Note that in Figure 4.3b the molecular state is labeled with $n = 4$ on the right and with $n = 3$ on the left side of the crossing and vice versa for the unbound trap state.

In the case of intermediate velocity the resonance is passed in a nonadiabatic way. The final state at $d = 1$ is the unbound trap state labeled with $n = 4$ with the fidelity of $|c_{\text{vib}}|^2 = 0.99$ (see Figure 4.4b). During the process the energy quantum number changes from $n = 3$ to $n = 4$, but the shape of the state does not change much. The quantum state is a trap vibrational state before and after the process.

Higher velocities result in excitations to higher vibrational states, especially $n = 5$ (see Figure 4.4c). At the final distance $d = 1$, $n = 5$ labels the first excited state in the trap. The final state is composed of the vibrational ground state $n = 4$ ($|c_{\text{vib}}|^2 = 0.67$) and of excited states. The first excited state $n = 5$ is populated with $|c_{\text{exc}}|^2 = 0.26$. The molecular state $n = 3$ is only $|c_{\text{mol}}|^2 = 1.3 \times 10^{-4}$ populated in this case.

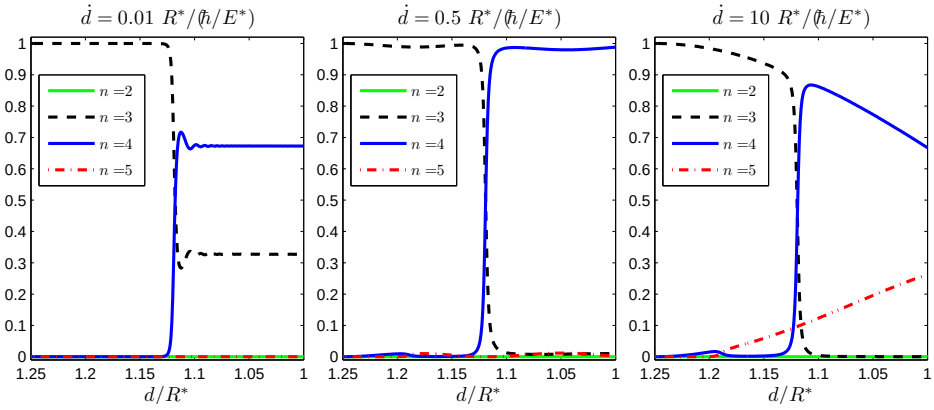

Figure 4.4: (a),(b) and (c) show population of energy eigenstates for a slow, intermediate and fast process, respectively. The initial state is $n = 3$ at $d = 1.25$ (the ground state of the trap). In the slow process some population goes into the molecular state, for intermediate speed the avoided crossing is traversed diabatically, while in a fast process higher vibrational states (especially $n = 5$) are excited.

4.3.3 Comparison of the Numerical Simulation with the Landau-Zener Formula

In this section we compare our numerical results to the predictions of the Landau-Zener Formula. We interpolate the nonadiabatic eigenenergy curves $E_1(d)$ and $E_2(d)$ through the avoided crossing and thereby obtain the crossing point d and the slope $\partial E_{12}/\partial d = \partial(E_1 - E_2)/\partial d$ (see dashed black lines in Figure 4.3b). We model the crossing with the Hamiltonian

$$\tilde{H}^{\Omega}(d) = \begin{pmatrix} E_1(d) & \Omega \\ \Omega^* & E_2(d) \end{pmatrix}. \tag{4.10}$$

where $\Omega = \langle \Psi_{\mathrm{mol}} | H | \Psi_{\mathrm{vib}} \rangle$ describes the coupling of the levels. We diagonalize $\tilde{H}^{\Omega}(d)$ to obtain its eigenvalues that are functions of d including the matrix element Ω as a parameter. We now fit the parameter Ω so that the eigenvalues of $\tilde{H}^{\Omega}$ match the adiabatic eigenenergies found in the spectrum. (see Figure 4.3b). The

$\dot{d}$	P_{na}	numerical result
$0.5\ R^*/(\hbar/E^*)$	0.992	0.988
$0.01R^*/(\hbar/E^*)$	0.702	0.673

Table 4.1: Comparison of Landau-Zener formula to the numerical simulation of the time evolution for the avoided crossing at $d = 1.119R^*$ in the spectrum of Figure 4.3. The comparison of P_{na} for the fast process with $\dot{d} = 10R^*/(\hbar/E^*)$ is not listed because in the numerical time evolution excitations to higher energetic states occur (see text for details).

position of the crossing is found as $d = 1.119R^*$ and the coupling matrix element is $\Omega = 0.43E^*$, which corresponds to an energy splitting of $\Delta E = 0.036\hbar\omega = 0.86E^*$. We use these parameters to calculate the probability of nonadiabatic passage P_{na} with Equation (4.6). This probability is compared with the coefficient $|c_{\mathrm{vib}}|^2$ in Equation (4.9) that gives the part of the final state of numerical time evolution that corresponds to the unbound trap state. The comparison can be made for different velocities $\dot{d}$. Table 4.1 summarizes the results for $\dot{d} = 0.01$ and $\dot{d} = 0.5R^*/(\hbar/E^*)$. For the fast process, a comparison of P_{na} is not possible because a third level becomes excited, which is not included in the Landau-Zener model. In this case we compare the probability of adiabatic traversal of the crossing $1 - P_{\mathrm{na}} = 3.5 \times 10^{-4}$ to the population of the molecular bound state $|c_{\mathrm{mol}}|^2 = 1.34 \times 10^{-4}$. Here, the Landau-Zener formula gives the same order of magnitude. For the velocities $\dot{d} = 0.5$ and $0.01R^*/(\hbar/E^*)$ the results compare well, although the fitted curves do not perfectly match the actual adiabatic curves. The fitting parameter Ω is obtained with and accuracy of 10^{-2}. Since Ω enters Equation (4.6) exponentially, this error can have a significant impact. In the case of $\dot{d} = 0.01R^*/(\hbar/E^*)$ the two results differ by 2%, which can be explained by this inaccuracy. Note also that the Landau-Zener formula is developed for constant $\partial E_{12}(d)/\partial d$, which is not given in our case, since other levels influence the considered avoided crossing.

Because of these inaccuracies, and because it cannot handle more than two levels, the Landau-Zener estimation is not the best choice for treating the relevant crossings and predict dynamics. However, it can help to estimate the relevance of

deep bound states. The energy of molecular bound states is $E_{\mathrm{mol}}(d) \approx E_{\mathrm{mol}}(0) + 1/2\mu\omega^2 d^2$ (see Figure 2.8 and Equations (2.16) and (2.17)). Deeply bound states can cross vibrational states only at large d. A semiclassical theory for estimating the coupling matrix element (and thereby the energy splitting) shows that ΔE decays exponentially with the trap distance (see [10]). In combination with the Landau-Zener formula this proves that resonances with deep bound states have no relevance for dynamics because they occur at large d. It is sufficient to include only the few bound states closest to the threshold in the calculations.

5 Atom-Ion Quantum Gate

In this chapter we simulate a specific gate process for a $^{135}Ba^{+}$ ion and a ^{87}Rb atom. The qubit states are encoded in hyperfine spin states

$$|0\rangle_{i,a} = |f_{i,a}{=}1, m_{f_{i,a}}{=}1\rangle_{i,a}$$
$$|1\rangle_{i,a} = |f_{i,a}{=}2, m_{f_{i,a}}{=}2\rangle_{i,a},$$

which leads to the two-qubit channels

$$|00\rangle = |f_i{=}1, m_{f_i}{=}1, f_a{=}1, m_{f_a}{=}1\rangle = |1,1,1,1\rangle$$
$$|01\rangle = |f_i{=}1, m_{f_i}{=}1, f_a{=}2, m_{f_a}{=}2\rangle = |1,1,2,2\rangle$$
$$|10\rangle = |f_i{=}2, m_{f_i}{=}2, f_a{=}1, m_{f_a}{=}1\rangle = |2,2,1,1\rangle$$
$$|11\rangle = |f_i{=}2, m_{f_i}{=}2, f_a{=}2, m_{f_a}{=}2\rangle = |2,2,2,2\rangle,$$

as defined in Equations (3.71) and (3.72). The dimensionless parameter $\alpha = (\hbar\omega/(2E^*))^2$ in the Hamiltonian Equation (5.3) is chosen as $\alpha = 146,046$. Both the Ba^{+} ion and the Rb atom are guided by traps with $\omega \approx 2\pi \times 26,9\text{kHz}$.

The essential parameters of our calculations are the singlet and triplet scattering lengths a_s and a_t. They can be measured in principle, but this has not been done so far. Our choice of the parameters of $a_s = 0.8R^*$ and $a_t = 1R^*$ allows for the application of an effective single channel model, which is found with the procedure explained in Section 3.7. In this model the isolated qubit channels $|00\rangle$, $|01\rangle$, $|10\rangle$ and $|11\rangle$ are each characterized by an effective short range phase. These four phases are similar, since singlet and triplet scattering lengths are similar. The validity of the single channel model for the $|10\rangle$ channel is estimated as 98.5%. The other channels are described much more accurately by a single channel model. The low validity of one model is due to the fact that for atom and ion being prepared in the $|10\rangle$ channel, a second open channel exists. This channel disturbes the $|10\rangle$ states. The maximal admixture of this second open channel was found in the state

with the angular momentum $l = 4$ and the energy $E \approx 118E^*$ to be 1.45%, so the 98.5% validity is a worst case estimation. Most of the $|10\rangle$ states are more accurate than this. The channels $|00\rangle$, $|01\rangle$ and $|11\rangle$ are the only open channel in their respective m_f-subspaces and therefore the single channel model is more accurate (see Sections 3.6.2 and 3.7).

There are combinations of a_s and a_t for which the channels are coupled and therefore one cannot create an effective single channel model. Such a combination is, for example, $a_s = -R^*$ and $a_t = +R^*$. Here, the two channels $|01\rangle$ and $|10\rangle$ are coupled. In this case one must perform a full multichannel calculation (see Section 3.2) or extract an effective two channel model for the ($|01\rangle$,$|10\rangle$) subspace of the computational basis. This more complicated situation is not considered in this thesis and will be a subject of future investigations. Here, we focus on the case of similar scattering lengths.

5.1 Four Channel Conditional Dynamics

By controlled four channel dynamics we attempt to realize a two-qubit phase gate that has the following truth table

$$\begin{aligned}
|00\rangle &\overset{\text{Interaction}}{\longrightarrow} e^{i\phi_{00}}|00\rangle \overset{U_S}{\longrightarrow} |00\rangle,\\
|01\rangle &\longrightarrow e^{i\phi_{01}}|01\rangle \longrightarrow |01\rangle,\\
|10\rangle &\longrightarrow e^{i\phi_{10}}|10\rangle \longrightarrow |10\rangle,\\
|11\rangle &\longrightarrow e^{i\phi_{11}}|11\rangle \longrightarrow e^{i\phi}|01\rangle.
\end{aligned} \tag{5.1}$$

The first step is the controlled collision of the atom and the ion that leads to different phases for each channel. By the single particle transformation U_S three of these phases can be undone according to [30]. One phase remains on the $|11\rangle$ channel. The transformation U_S acts on the atom and the ion separately and therefore can be applied after the ion is transported away from the atom. The desired phase gate requires the relation of the channels phases to be

$$\phi = \phi_{00} + \phi_{11} - \phi_{01} - \phi_{10}. \tag{5.2}$$

If the gate phase is $\phi = \pi$ or an odd integer multiple of π, the phase gate is equivalent to the CNOT gate. A Hadamard transformation (a single qubit operation),

is to be applied on the target qubit before and after the π-phase gate to obtain the CNOT gate. This, or any equivalent entangling two-qubit gate is a necessary part of a quantum computer. Arbitrary quantum operations can be composed of single qubit rotations and an entangling two-qubit gate. Single qubit operations on a single ion/atom have already successfully been realized in experiment, e.g. with laser driven Raman transitions (see e.g. [14]).

For each of the qubit channels $|00\rangle$, $|01\rangle$, $|10\rangle$ and $|11\rangle$ an effective single channel model is established with the methods described in Section 3.7. Those four channels are then isolated. The equations for time evolution derived in Section 4.2.1 are valid for one channel. In this section we give the Hamiltonian for one channel and compose the full Hamiltonian of four channels. The four channel dynamics is fundamental for the gate process of Sections 5.3,5.5 and 5.6.

We denote $|\Psi^A\rangle$ as the state of relative motion of atom and ion being in the spin state corresponding to the qubit channel $A \in \{00, 01, 10, 11\}$. In contrast $|A\rangle$ denotes the pure spin state of atom and ion. Since the channels are isolated in our model, it is not possible that e.g. $|\Psi^{00}\rangle$ evolves to $|\Psi^{01}\rangle$. It is, however, possible that atom and ion prepared in the channel $|00\rangle$ change their quantum state of motion in $|\Psi^{00}\rangle$, e.g. get excited from the trap vibrational ground state to the first excited state.

The relative Hamiltonian for an atom-ion collision in the qubit channel $|A\rangle$ in dimensionless coordinates is

$$H_A^{(d)} = H_A^{(0)} + \alpha d(t)^2 \mathbf{1} - \alpha d(t)\, z. \tag{5.3}$$

Here, $H_A^{(0)}$ denotes the relative Hamiltonian of atom-ion motion for $d = 0$ trap separation in the case that the particles are prepared in the channel A. We can denote this Hamiltonian of relative motion in its eigenbasis:

$$H_A^{(d)} = \sum_n E_n^{(d),A} |\Psi_n^{(d),A}\rangle\langle\Psi_n^{(d),A}|. \tag{5.4}$$

In the following we will assume an implicit d dependency of the Hamiltonian and its eigenfunctions and suppress '$(\cdot)^{(d)}$' in the notation. The total Hamiltonian for all computational basis channels including external degrees of freedom is

$$H = H_{00} \otimes |00\rangle\langle 00| + H_{01} \otimes |01\rangle\langle 01| + H_{10} \otimes |10\rangle\langle 10| + H_{11} \otimes |11\rangle\langle 11|. \tag{5.5}$$

An arbitrary state of this system can be written down as a linear combination of the four qubit-channels:

$$|\Psi\rangle = \alpha|\Psi^{00}\rangle|00\rangle + \beta|\Psi^{01}\rangle|01\rangle + \gamma|\Psi^{10}\rangle|10\rangle + \delta|\Psi^{11}\rangle|11\rangle. \tag{5.6}$$

Time evolution of this state is given by the time evolution operator:

$$\begin{aligned} |\Psi(t)\rangle &= e^{-i/\hbar \int_0^t H \,\mathrm{d}\tau}|\Psi(0)\rangle \\ &= \alpha e^{-i/\hbar \int_0^t H_{00} \,\mathrm{d}\tau}|\Psi^{00}\rangle|00\rangle + \beta e^{-i/\hbar \int_0^t H_{01} \,\mathrm{d}\tau}|\Psi^{01}\rangle|01\rangle \\ &+ \gamma e^{-i/\hbar \int_0^t H_{10} \,\mathrm{d}\tau}|\Psi^{10}\rangle|10\rangle + \delta e^{-i/\hbar \int_0^t H_{11} \,\mathrm{d}\tau}|\Psi^{11}\rangle|11\rangle. \end{aligned} \tag{5.7}$$

Since the channels are isolated, the time evolution of all four channels leads to a different phase for each channel. It is implied that before the time evolution starts, the particles are prepared in the ground state $|\Psi_{\mathrm{ini}}\rangle$ of their traps (we assume zero temperature). At the end of the process, the particles shall reach this state again, but will have accumulated an individual phase.

Since in our model the channel dynamics are isolated, we can handle the gate process for each channel separately. The requirements for a successful gate are formulated in the following equation for the final state $|\Psi^A_{\mathrm{fin}}\rangle$ of channel $|A\rangle$:

$$|\Psi^A_{\mathrm{fin}}\rangle = e^{i\phi'_A}|\Psi^{\mathrm{A}}_{\mathrm{ini}}\rangle, \tag{5.8}$$

where ϕ'_A is the desired phase to be accumulated. The process phase

$$\phi_A(T) = \arg(\langle\Psi^A_{\mathrm{ini}}|\Psi^A(T)\rangle). \tag{5.9}$$

for one channel $|A\rangle$ is defined as the angle in the complex plane of the overlap of the initial state $|\Psi^A_{\mathrm{ini}}\rangle$ with is the state $|\Psi^A(T)\rangle$ obtained by the actual time evolution at the final time T. The phase $\phi_A(T)$ is a relevant quantity only if the scalar product of the final state at $t = T$ and the initial state has an absolute value close to one, since then $|\Psi^{\mathrm{A}}(T)\rangle \approx \exp(i\phi_{\mathrm{A}})|\Psi^{\mathrm{A}}_{\mathrm{ini}}\rangle = |\Psi^{\mathrm{A}}_{\mathrm{fin}}\rangle$.

We define the fidelity for one channel at zero temperature according to [31] as

$$F_A = \frac{1}{2}\left[1 - |\langle\Psi^A_{\mathrm{ini}}|\Psi^A(T)\rangle|\cos(\pi - \Delta\phi_A)\right] \tag{5.10}$$

where $\Delta\phi_A = \phi_A(T) - \phi'_A$ is the difference between the desired channel phase ϕ'_A and the phase $\phi_A(T)$ obtained by actual time evolution. In the following, we will

according to Equation (5.2) assume that the phases for the channels $|00\rangle$, $|01\rangle$ and $|10\rangle$ are undone perfectly due to single qubit rotations leading to $\Delta\phi_{00} = \Delta\phi_{10} = \Delta\phi_{01} \equiv 0$, while $\Delta\phi^{11}$ is nonzero. The fidelity is $F_A = 1$ for all channels if the overlap of the initial and final state has the absolute value one for each channel and the total gate phase is $\phi = \pi$, computed from the single channel phases with Equation (5.2).

We can then define the gate fidelity as

$$F_{\text{gate}} = \min_A F_A, \tag{5.11}$$

since in our model the channels are decoupled (we neglect spin changing collisions).

5.2 Idea of a Quantum Gate using Trap-Induced Resonances

The initial state for a gate process is the trap ground state at a certain distance $d_{\max}$ (see Figure 4.1b). We consider all avoided crossings and their effect on dynamics for $d < d_{\max}$. There are deeper bound molecular states that cross the ground state level of the trap at $d > d_{\max}$, but since these resonances are very weak they are not relevant, as described in Section 4.3.3. Bringing the atom and the ion to the distance $d_{\max}$ is a transport problem. Since this work rather focuses on controlled atom-ion interaction, we refer to other research projects like [32, 33, 34] that address optimal transport of trapped ions and atoms. Resonances that occur on the way to $d_{\max}$ will be passed diabatically.

During the gate time T the traps will be moved close together to let the particles interact, then separated again to the initial distance. The controlling function is the trap distance $d(t)$ as a function of time.

For the sake of clarity we summarize: a qubit channel denominates a specific spin configuration of the atom and the ion. If the particles are prepared in one of the four channels, many eigenstates of relative motion (molecular and unbound states) exist. Initially the particles are prepared in their trap ground states and this state is denoted as $|\Psi^{\mathrm{A}}_{\mathrm{ini}}\rangle$, where $\mathrm{A} \in \{00, 01, 10, 11\}$ denotes the channel. It is

desired that after the gate process the particles are in the trap ground state again and have picked up a two-qubit phase $\phi_A(T)$ that depends on the channel.

The idea of an adiabatic gate is the following: one starts with the trap ground state $|\Psi_{\text{ini}}\rangle$. The traps are brought together, in a way that the quantum state remains unbound while passing weaker resonances at larger d diabatically. At smaller d, a big resonance is followed adiabatically to reach a molecular state $|\Psi_{\text{mol}}\rangle$. In the energy diagram the curve depicted in Figure 5.1a is followed from $|\Psi_{\text{ini}}\rangle$ to $|\Psi_{\text{mol}}\rangle$ and back again. In this case the accumulated phase for the channel A can be estimated with the potential energy integral

$$\phi^A_{\text{pot}} = -\frac{1}{\hbar}\int_{t_{\min}}^{t_{\max}} E^A(t)\mathrm{d}\,t. \tag{5.12}$$

where $E^A(t)$ is the potential energy curve followed in the process. This integral can be found, for example, in [20]. As seen in Figure 5.1b, the energy spectra are different for all four qubit channels. Consequently the potential energy phase is different for each channel, which provides the possibility of a phase gate (see Equation (5.1)). The differences of the energy curves are not so large, because the scattering lengths are similar. Larger differences in energy would be found if singlet and triplet scattering lengths differed more. In this case the qubit channels would also stronger couple, which would result in spin-changing collisions that are not desired in the phase gate process.

5.3 Adiabatic Quantum Gate

This section presents the results of the numerical simulation of an adiabatic atom-ion quantum gate. We use 300 basis functions, which makes the truncation error for the states smaller than 10^{-4}. We also compare the gate phases to the potential energy phase calculated with the integral of Equation (5.12).

In the following, the shape of $d(t)$ that allows to follow the energy curve depicted in Figure 5.1a is determined. Initial and molecular states are marked in Figure 5.2b. Different velocities are used to compose the desired $d(t)$ function. At $d \approx 1.5$ to $d \approx 1$ the speed is as fast as possible while still avoiding excitations to pass the small resonances diabatically. To follow the big resonance at $d \approx 0.7$,

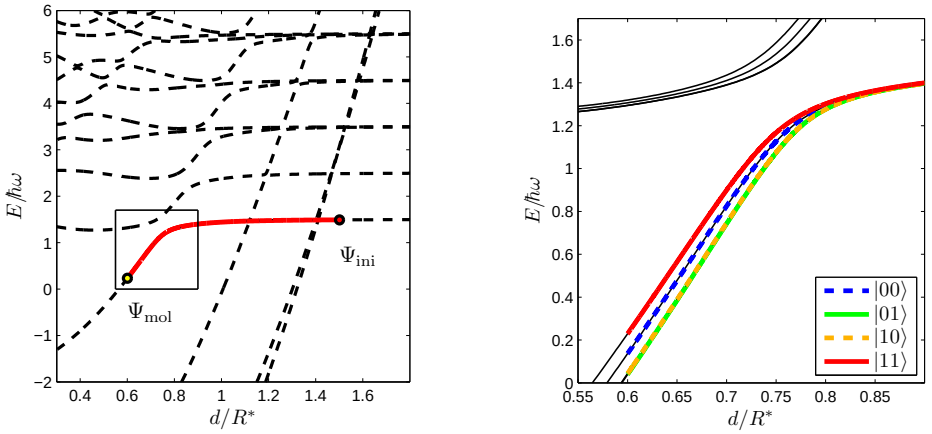

(a) (b)

Figure 5.1: Energy curve followed in the adiabatic process (left panel) for the example of the $|11\rangle$ channel. The different energies of the channels at small d can be seen in the close-up (right panel). The difference between $|01\rangle$ and $|10\rangle$ is not resolved. Larger differences between the energy curves would be found if singlet and triplet scattering lengths differed more.

the speed is reduced. The kinks are rounded to avoid excitations. In our example calculation we change the velocities twice: starting from $\dot{d}_1 = 0.8$, we reduce to $\dot{d}_2 = 0.5$ and finally to $\dot{d}_3 = 0.1\ R^*/(\hbar/E^*)$. The unit $R^*/(\hbar/E^*)$ corresponds to $2,05$mm/s in our case. The same way is followed back to the initial trap separation. The fidelity of the gate came out to be very sensitive on the details of the $d(t)$ function. We found out that a relatively large overlap of the time evolved final state with the initial trap ground state is obtained, if the turning point $d_{\rm min}$ lies behind the resonance. Therefore we chose $d_{\rm min} = 0.6R^*$. The largest difference in energy is found at small values of d. We introduce a time delay at $d_{\rm min}$ and wait until the required gate phase of $\phi = \pi$ is accumulated. In doing so we obtain a $d(t)$ function depicted in Figure 5.2a that corresponds to a process time of $T = 11.959\hbar/E^*$. Most of the time is needed to transfer the molecular state with the speed $\dot{d}_3$. The time delay at $d_{\rm min}$ is short compared to that transfer time. We

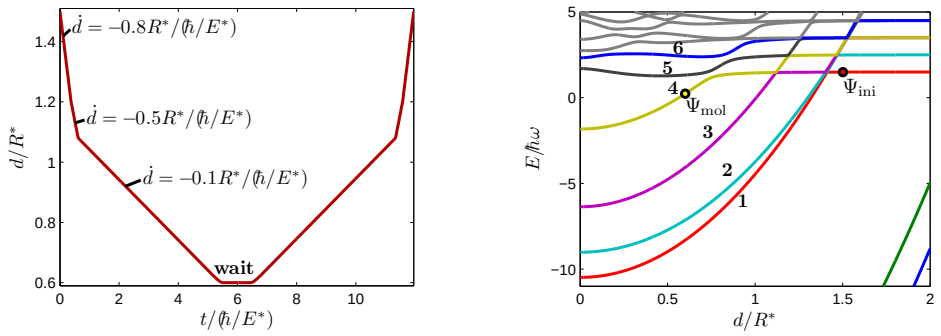

(a) (b)

Figure 5.2: Manually designed $d(t)$ function for the adiabatic process (left panel) and spectrum of the qubit channel $|11\rangle$ (right panel). The spectra for the other three channels look qualitatively similar. Eigenstates are labeled by energy in ascending order.

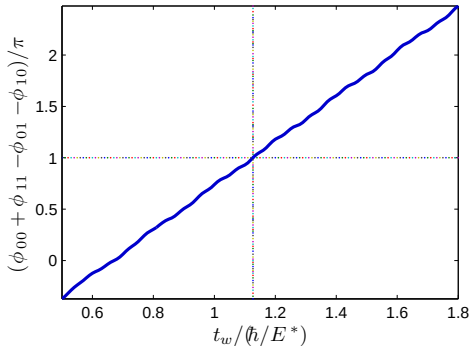

Figure 5.3: Variation of the waiting time t_w to optimize the gate phase ϕ. The desired odd integer multiple of π is reached at $t_w = 1.127\hbar/E^*$.

performed a numerical simulation of time evolution of all four channels based on this $d(t)$. A satisfying result for the gate phase can be obtained by a variation of the waiting time t_w. Figure 5.3 shows the resulting gate phase as a function of the waiting time. As seen in the figure, a phase of π is obtained with a waiting time around $1.127R^*/(\hbar/E^*)$. The adiabatic gate process results in the fidelities and phases summarized in Table 5.1. Equations (5.11) and (5.10) yield a gate fidelity $F = 0.98$, the gate phase is $\phi = 0.998\pi$ obtained with Equations (5.9) and (5.2).

Channel	$F_{A,\mathrm{num}}$	ϕ_{num}	ϕ_{pot}	ϕ_{kin}	$\phi_{\mathrm{kin}} + \phi_{\mathrm{pot}}$
00	0.98652	0.00829π	1.902718π	-0.0552π	1.847536π
01	0.98624	1.12677π	1.024376π	-0.0552π	0.969194π
10	0.98687	1.02621π	0.921919π	-0.0552π	0.866736π
11	0.97909	1.14311π	1.053739π	-0.0552π	0.998556π
Gate:	0.97909	0.99842π	0.951437π	0	0.951437π

Table 5.1: Results of the adiabatic gate process using $d(t)$ shown in Figure 5.2a. The gate time is $T = 11.959\hbar/E^*$. Phases are given modulo 2π. The gate fidelity of $F = 0.98$ is calculated with Equation (5.11) where we use $\Delta\phi_{00} = \Delta\phi_{01} = \Delta\phi_{10} = 0$ and $\Delta\phi_{11} = (1 - 0.998)\pi$. The total gate phase is $\phi = 0.998\pi$ for the numerical (num) time evolution. It consists of the channel phases $\phi_{...} = \phi_{00} + \phi_{11} - \phi_{01} - \phi_{10}$ according to Equation (5.2). Phases resulting from numerical time evolution are compared to the integral of the energy curve and the kinetic energy calculated with Equations (5.12) and (5.13). The results agree up to 15%.

We illustrate the process by plotting in Figure 5.8 the population of the relevant adiabatic eigenstates as a function of time during the process. In this plot we observe that the molecular state is nearly 100% populated at the minimal distance. Small variations of this population show that the process is not entirely adiabatic.

Table 5.1 further compares the numerical calculation of the phases to an estimation given by the adiabatic potential energy integral of Equation (5.12). An additional contribution to the phase of a channel beyond adiabaticity is the kinetic phase

$$\phi^A_{\mathrm{kin}} = \int_{t_{\mathrm{min}}}^{t_{\mathrm{max}}} -\frac{\mu}{2}(\dot{d})^2 \,\mathrm{d}t, \tag{5.13}$$

which is the first correction to the adiabatic phase. It is obtained by taking the expectation value of the kinetic part of the Hamiltonian $\mathbf{p}^2/2\mu$.The kinetic phase is the same for each channel and in the adiabatic limit it vanishes. The results differ slightly from the numerical simulation, which can be explained by excitations to higher levels. The energy integral assumes that the excitations seen in the

numerical simulations do not happen. Since the kinetic phase is small ($\sim 10^{-2}\pi$) but not negligible, the process is not entirely adiabatic.

The fidelities reached with the manually adjusted $d(t)$ function are not very good. We expect that if one would invest more time into manually optimizing the $d(t)$ function, e.g perform more parameter variations, the outcome would be much better. Instead, we decided to optimize the gate with a more sophisticated method and used optimal control techniques, as described in Section 5.5.

5.3.1 A Faster Adiabatic Gate

In this section we try to find a faster adiabatic gate process. Therefore we vary $d_{\min}$ and monitor the gate phase. The results are depicted in Figure 5.4a. A phase of π can be obtained with a minimal distance of $d_{\min} = 0.75R^*$ or smaller, without changing the velocities $\dot{d}_{1,2,3}$. The $d(t)$ function with $d_{\min} = 0.75R^*$ is depicted in Figure 5.4b. The corresponding gate phase is 1.0039π, the process time is $T = 7.83\hbar/E^*$ and the gate fidelity is $F = 0.947$, which is smaller than the fidelity obtained with $d(t)$ of Figure 5.2a. Because of this smaller fidelity we remain with the slower process. Of course we could also apply optimal control techniques (see Section 5.4) in this case in order to increase the fidelity.

5.4 Use of Optimal Control Techniques

Using optimal control techniques we can improve the gate fidelity as well as reduce the gate time. The iterative algorithm we use for optimal control is described in Appendix B. The objective

$$J[\{\Psi^{\mathrm{A}}(T)\}] = \sum_{\mathrm{A}} 2\mathrm{Re}\{\langle\Psi^{\mathrm{A}}_{\mathrm{fin}}|\Psi^{\mathrm{A}}(T)\rangle\}. \tag{5.14}$$

should reach the value $J = 8$ when the final state of time evolution reaches the desired final state. Not only the fidelity, but also phase is included. Here, the objective final states phases are chosen in a way that the gate phase in Equation (5.2) is π. Only this relation of the single channel phases is important for the two-qubit phase gate, because the particular channel phases can be undone by single qubit rotations [30]. The algorithm needs a good initial guess to converge.

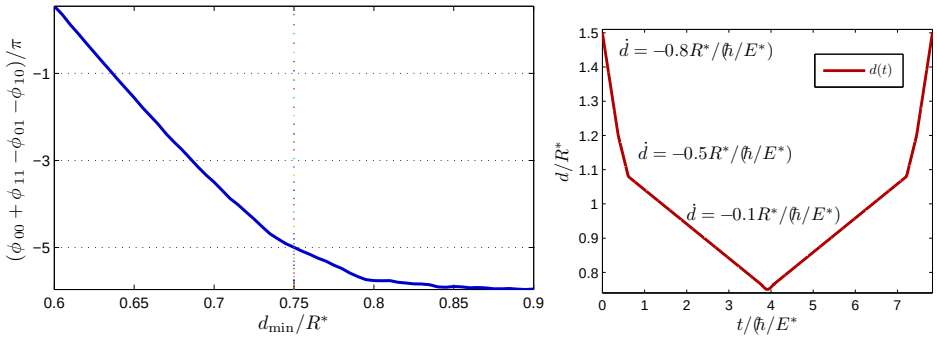

(a) (b)

Figure 5.4: Variation of $d_{\min}$ to find the minimal gate time required for a gate phase of $(2k+1)\pi$. We find that for $d_{min} = 0.75$ a gate phase of $\phi = -3\pi$ is reached. The time for this process is $T = 7.83\hbar/E^*$ only, but the fidelity $F = 0.93$ is less than for the process in Section 5.3.

Our calculations showed that the fidelity can be improved during each iteration step quite well, while the phase is not altered much by the algorithm. That is why a precise parameter variation (e.g. of a time delay at minimal distance) is helpful before starting the optimization algorithm in order to adjust the gate phase to π. For the time evolution we use the Crank-Nicholson method described in Appendix A.3, because the quantum state is available at each time step in this method, which is essential for the optimal control algorithm we use. The required time steps are estimated by comparison to the Matlab routine *ode45* with built-in error estimation.

The following optimization processes are performed and presented in the next sections. In Section 5.5 the fidelity of the adiabatic gate is optimized in order to obtain a reasonable value. In Section 5.6 a fast, non-adiabatic, gate process optimized.

5.5 Optimization of the Adiabatic Gate

The fidelity of the adiabatic process described in Section 5.3 was not desirable, although the phase could be adjusted precisely. In this section the process is optimized. We initialize the optimization algorithm with $d(t)$ as in Figure 5.2a, as the gate phase obtained with this $d(t)$ is very close to π. After 25 iterations with 20000 time steps a satisfying result is reached; the fidelity is $F = 1 - 3.1 \times 10^{-4}$ and the gate phase is $\phi = 1.003\pi$. The population of adiabatic energy eigenstates is depicted in Figure 5.7 for the $|00\rangle$ channel. One can see, that excitation to higher vibrational states during the process is suppressed by the optimal control algorithm.

We use 300 basis functions, which makes the truncation error smaller than 10^{-4}. Because no direct error control is available for the Crank-Nicholson method, the optimized pulse was interpolated with a cubic Hermitian interpolation polynomial and fed in the Matlab routine *ode45* with relative error tolerance of 10^{-5}. The routine produced a gate phase $\phi = 1.003\pi$ and a fidelity $F = 1 - 2.5 \times 10^{-4}$, which agrees very well with the Crank-Nicholson method. These results are summarized in Table 5.2. Note that the single phases comparing both methods differ by up to 0.035π. This phase difference cancels out in the computation of the gate phase. Figure 5.5 depicts the optimized $d(t)$ function. On a large scale it looks like the initial function, but on a small scale some 'wiggles' occur. These small scale modifications can be seen in Figure 5.5b. They have an amplitude of the order of $0.01R^*$ in characteristic units of interaction. This corresponds to 3nm for the Barium$^+$-Rubidium system and for a Ca$^+$-Na system $0.01R^*$ equals $\sim$ 1nm. Both values are quite small and experimentally challenging.

The time scale of the system is given by $\hbar/E^* = (\sqrt{\alpha}/\pi)\, T_{\mathrm{osc}}$, where $T_{\mathrm{osc}} = 2\pi/\omega$ is the oscillator period of the harmonic trap. For the Ba$^+$-Rb collision the total gate time therefore is $T \approx 12\hbar/E^* \approx 1,7$ms. The time scale of the wiggles is $\delta t = 0.05\hbar/E^* \approx 7,2\mu$s.

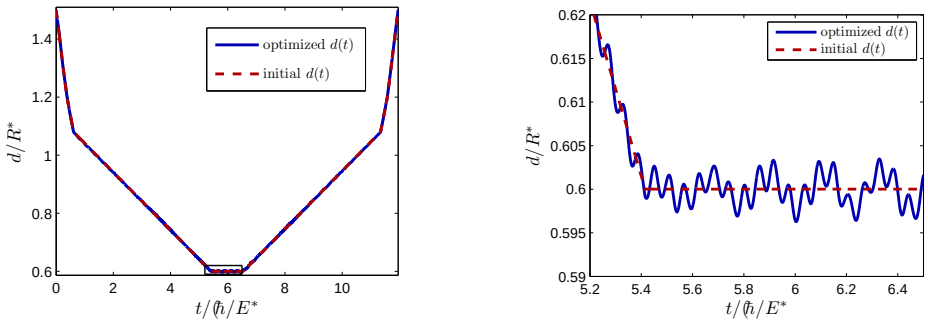

(a) (b)

Figure 5.5: Optimized $d(t)$ function for the adiabatic gate (left panel) and close-up (right panel). The optimized function shows small scale wiggles (amplitude $\approx 0.01R^*$).

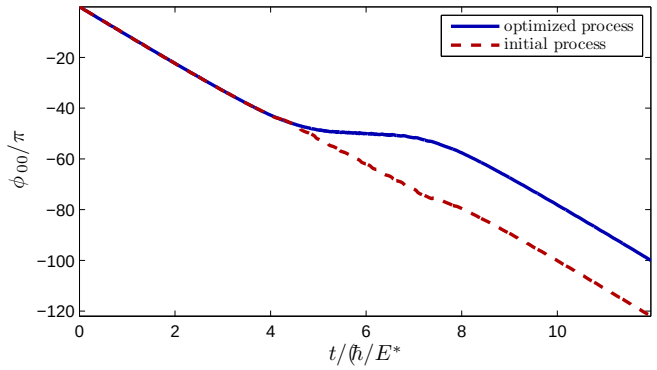

Figure 5.6: Evolution of the phase of channel $|00\rangle$ during initial and optimized adiabatic process. It is remarkable that the phases of all channels are affected by the optimization algorithm in a way that the total gate phase (Equation (5.2)) is not altered much.

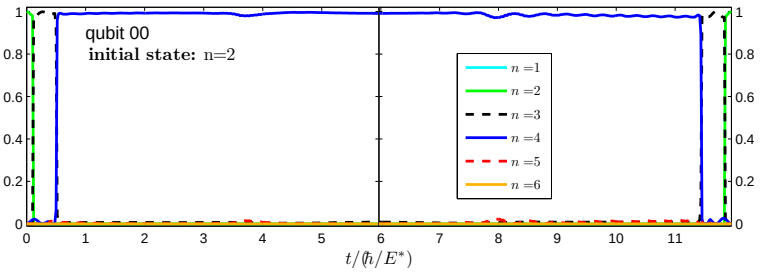

Figure 5.7: Population of energy eigenstates during the optimized gate process, for qubit channel $|00\rangle$. Compared to Figure 5.8 less excitation to higher vibrational states during the process and a fidelity closer to one at the final time can be observed. The curves for the other qubit channels look qualitatively similar.

	Channel	Fidelity	Phase
C-N	$\|00\rangle$	$1 - 7.5 \times 10^{-5}$	1.9987 π
	$\|01\rangle$	$1 - 2.7 \times 10^{-4}$	1.1218 π
	$\|10\rangle$	$1 - 3.1 \times 10^{-4}$	1.0204 π
	$\|11\rangle$	$1 - 7.4 \times 10^{-5}$	1.1467 π
	Gate	$1 - 3.1 \times 10^{-4}$	1.0031 π
ode45	$\|00\rangle$	$1 - 7.5 \times 10^{-5}$	0.0024 π
	$\|01\rangle$	$1 - 1.5 \times 10^{-4}$	1.1254 π
	$\|10\rangle$	$1 - 2.5 \times 10^{-4}$	1.0240 π
	$\|11\rangle$	$1 - 1.3 \times 10^{-4}$	1.1502 π
	Gate	$1 - 2.5 \times 10^{-4}$	1.0032 π

Table 5.2: Results of the optimized adiabatic gate process using $d(t)$ shown in Figure 5.5. The two tables compare the Crank-Nicholson method (CN) used for the optimization and the Matlab routine *ode45* with a relative error tolerance of 10^{-6}. Phases are given modulo 2π. The gate phase is $\phi = 1.003\pi$ and gate fidelity is $1 - 3.1 \times 10^{-4}$ calculated equivalently to Table 5.1 with Equations (5.2) and(5.11).

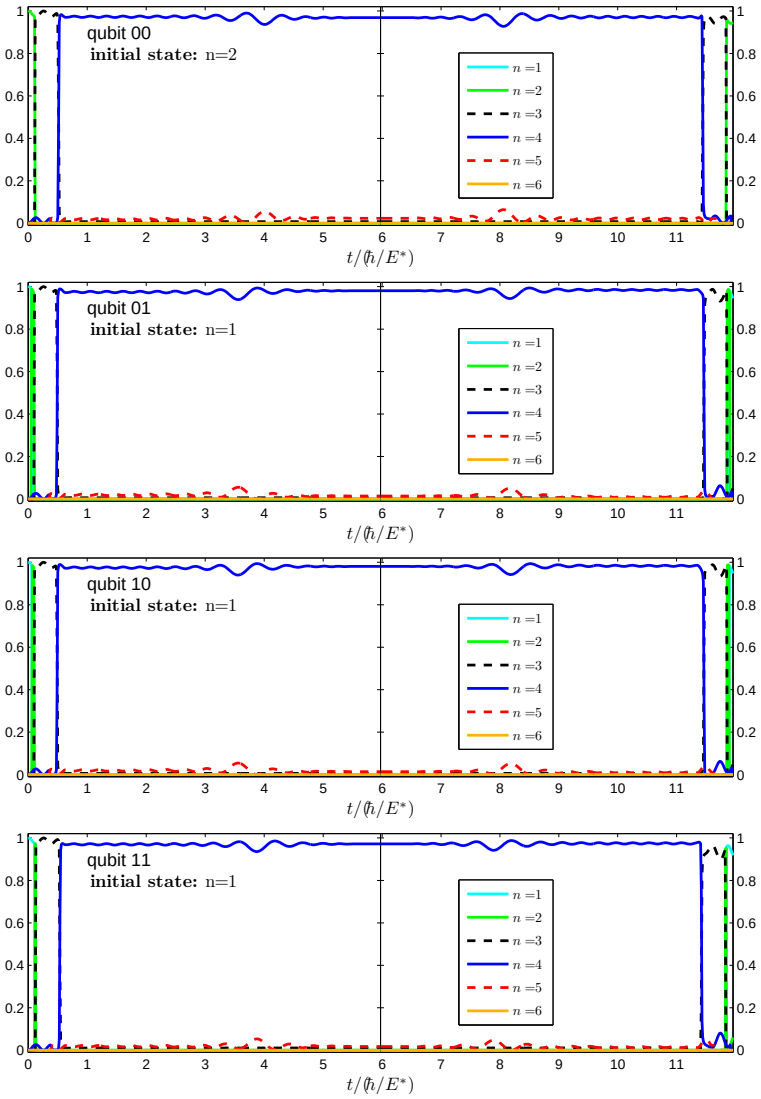

Figure 5.8: Populations as a function time for all four qubit channels during the adiabatic gate process with $d(t)$ of Figure 5.2a. The initial state is the trap ground state. The overall gate time is $T = 11.959\hbar/E^*$. The diabatic passage of the weaker resonances takes place at the beginning and at the end of the process. The quantum state at $d_{\min} = 0.6R^*$ is the molecular state $n = 4$ with a fidelity close to one in each channel.

5.6 Optimized Fast Gate

With the help of optimal control techniques it is possible to reduce the overall gate time, which is desirable for application in quantum computation. Our procedure to find an optimized process realization with short gate time is the following: first we look for an initial $d(t)$ function, that in a short time causes a phase shift of π. A successful initial guess function is the Gaussian $d(t)$ curve that is delayed at the minimal distance $d_{\min}$ by a waiting time depicted in Figure 5.9. This waiting time is varied in a similar way to the parameter variation in Figure 5.3. In general, the resulting channel fidelities are not satisfactory. As a second step we run our optimal control program in order to increase the fidelities.

The process we found in this way uses the total gate time of $T \approx 4.1\hbar/E^*$, which is an improvement by the factor of three with respect to the adiabatic process that needed $T \approx 12\hbar/E^*$. The optimized $d(t)$ function shows larger variations than the adiabatic example of Section 5.5, but also small scale wiggles (see Figure 5.9). Figure 5.11 shows the population of the most important adiabatic eigenenstates during the fast gate process. One can observe that the molecular state at $d_{\min}$, $n = 4$, is only populated between 15% to 40%, depending on the channel. The main part of the phase is accumulated in the molecular state. Due to its small population a larger waiting time at $d_{\min}$ is required than for the adiabatic case. The final fidelities of the process are listed in Table 5.2. The overlap of the initial and final wave functions is good as $\sim 1 - 10^{-6}$, but the gate phase is 1.015π, which is 1.5% inaccurate with respect to the objective phase of π. The gate fidelity is calculated to $F = 1 - 9.5 \times 10^{-4}$ with Equation (5.11). We stopped the optimization at 250 iterations (when this result was reached), because this exceeds the worst-case-estimated accuracy of underlying the single channel model (see Section 3.7) of 98.5%. If the algorithm was given more time, the phase would have been improved more. The convergence of the objective is shown in a log-log plot in Figure 5.10. A further significant improvement could be expected at an additional number of iterations of the order of 100.

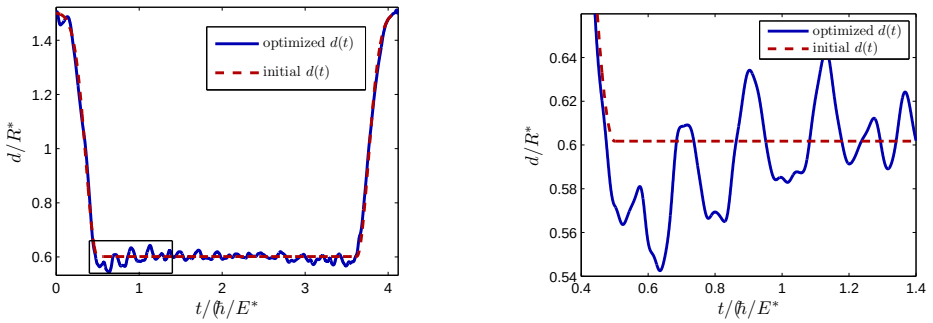

(a) (b)

Figure 5.9: Optimized $d(t)$ function for the non-adiabatic gate (left panel) and zoom-in (right panel). The process time is $4.1\hbar/E^*$ The optimized function shows larger wiggles (amplitude $\approx 0.05R^*$) and smaller ones (amplitude $\approx 0.005R^*$).

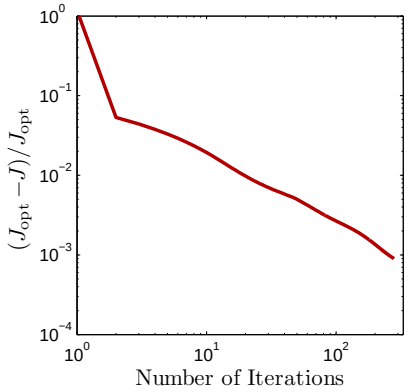

Figure 5.10: Convergence of the optimization algorithm. At 250 iterations the procedure is stopped.

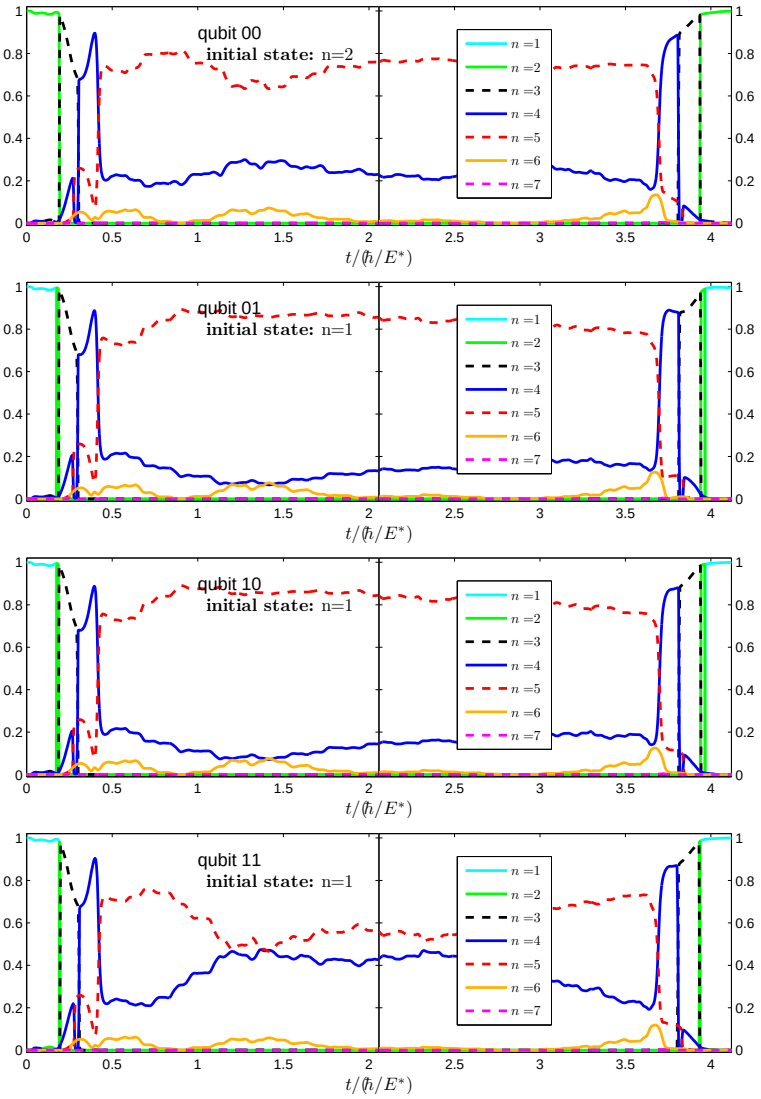

Figure 5.11: Population of the most important adiabatic eigenstates as a function of time for all four qubit channels during the non-adiabatic gate process. The underlying trap separation $d(t)$ depicted in Figure 5.9. The initial state is the trap ground state at maximal distance. The molecular state $n = 4$ at $d_{\min}$ (mid of figure) is only populated between 15% and 40%.

5.7 Limitations of the Current Approach

The present approach for realizing a quantum gate is mainly limited by the fact that the single channel model is, in the worst case, only accurate up to 1.45%. The threshold of gate error tolerance to successfully apply quantum error correction protocols lies between 10^{-3} and 10^{-4}, depending on other parameters [35]. This accuracy is not guaranteed by the present model. It is, however, possible that for a different combination of singlet and triplet scattering lengths the single channel model is more accurate. An N-channel approach can help in cases of strongly coupled channels.

Although the gate time was decreased by a factor of three with the help of optimal control techniques, we expect that one can further decrease it. During the gate process presented in Section 5.6, most of the population does not go to the molecular state, but stays in vibrational states. Since most of the phase is accumulated in the molecular state, the potential advantage of staying in the molecular state is that we may produce shorter gate times. Since the optimal control algorithm as we use it so far is not able to drastically change the populations of the adiabatic eigenstates around the minimal distance, a further optimized gate must choose a different initial guess than the Gaussian function with a time delay. It is promising to split the optimization into parts: first, the goal is to evolve the initial state at $d_{\max}$ to a molecular state in the shortest time possible; second the gate phase is to be accumulated and third the initial state is to be obtained again in short time. With this procedure it should be possible to reach the quantum speed limit given by the difference of the energy curves of the molecular states of the four channels.

The further optimization of the gate time as well as the enhancement of the accuracy of the collision model will be part of future investigations.

6 Conclusions & Future Work

In this work we analyzed the spin-state-dependent interaction between a single atom and a single ion guided by external trapping potentials. We applied our insight on this system in order to realize a two-qubit quantum gate process and thereby provide the basic ingredient for quantum computation with atoms and ions combined in one setup. This work was motivated by recently opened experimental possibilities combining magneto-optical traps or optical lattices for atoms, and RF electromagnetic fields for ions. These experiments are currently established in several groups worldwide [9, 8].

We started our description of controlled interaction of an atom and an ion by formulating a multichannel quantum-defect theory for trapped particles, analogous to the free-space case discussed in [7]. This step was necessary because the short-range part of the atom-ion molecular potentials are not yet available. We introduced a set of two parameters—the singlet and triplet scattering lengths—to model this short-range interaction. These parameters can be measured in upcoming experiments and then substituted into our equations.

A remarkable feature of the system is trap-induced shape resonances that couple molecular bound states to unbound trap states. Quasistatic eigenenergy curves show these resonances as avoided crossings. They can be used to form ultracold trapped molecular complexes and thereby allow full control of cold chemical reactions. It is also possible to substitute the single atom with a single nonpolar molecule and study its interaction with a single ion.

In this work we reduced the multichannel formalism to an effective single channel model for one specific spin state of atom and ion. The validity of this model, which depends on the actual values of the singlet and triplet scattering lengths, was discussed. Where applicable, our effective single channel model can be implemented in calculations regarding ultracold chemistry as well as atom-ion scattering

physics. A single channel model was already discussed in [10], with the difference that the spin state of atom and ion was not included (in other words, a quantum defect parameter was assigned to each spin state separately). In our present approach we can describe relations between these quantum-defect parameters, because all single channel models originate from the same multichannel formalism. Therefore, we can apply the model for quantum computation schemes which store qubits in internal spin states of atom and ion.

Our idea of the phase gate process makes use of trap-induced resonances. Atom and ion are prepared in the trap vibrational ground state. By bringing the traps close together we let the particles interact ad finally separate them, obtaining the motional ground state again. In doing so we cross weaker resonances diabatically (remaining in a trap state) and then follow a strong resonance adiabatically to a molecular bound state, where a two-qubit phase is accumulated. Since the positions of the resonances are different for each spin combination, the accumulated phase is different for each qubit channel and we are able to control the trap distance in such a way that a two-qubit phase gate is realized. This phase gate, in combination with single qubit rotations, is a universal gate for quantum computation.

We performed numerical simulations of the essential features of the controlled collision specifically for a $^{135}Ba^{+}$ ion interacting with a ^{87}Rb atom, each guided by spherically symmetric harmonic traps with $\omega_{i,a} \approx 2\pi \times 27\text{kHz}$. For this, we assumed similar singlet and triplet scattering lengths of 4435 and 5544 Bohr radii respectively, which allows the application of a single channel model. For this situation we have chosen hyperfine-qubit states to obtain the four qubit-channels $00, 01, 10, 11$. In contrast, opposite scattering lengths exclude a single channel description. In this framework we found a two-qubit phase gate gate process entangling atom and ion. We thereby showed that trap-induced resonances can be used to control the interaction of atom and ion. Assuming the correctness of our model, the fidelity for our gate process is $1 - 2.5 \times 10^{-4}$ and in this case the gate time is 1.7ms. Using optimal control techniques we were able accelerate the process to 0.58ms. In future work we plan to decrease the gate time by tightening the traps (higher trapping frequency) and by further optimizing the process.

We estimated the validity of our specific single channel model to 0.985, which can be increased by assuming a different combination of singlet and triplet scattering lengths that are more similar, thus for which a single channel model is more applicable. On the other hand, this would require longer gate times. Moreover, we can perform full multichannel calculations to overcome this problem.

The numerical simulation of the collision within the multichannel formalism is desirable because it allows general combinations of the scattering lengths. In this context the scattering lengths of the channels can differ more greatly, which not only includes a more general description of the atom-ion system, but also would allow possibly much faster quantum gates.

In our model, we assumed harmonic trapping potentials, and the oscillator frequencies were equal for atom and ion. More general situations, like cigar-shaped trapping potentials, are expected to allow an application of the basic ideas developed in this thesis. In the context of this generalization, it is also desirable to consider particular experimental realizations in order to describe them with our theory and compare the results.

So far, we did not use external magnetic fields in order to manipulate the interaction. Magnetic induced Feshbach resonances have been applied very successfully in this context. Future investigations will include magnetic fields to control the atom-ion interaction even more efficiently and possibly combine trap-induced resonances and Feshbach resonances for this purpose. Our work can be seen as a principle investigation of a new, interesting physical system and can be extended in many directions.

A Numerical Methods

A.1 The Renormalized Numerov Method

The Numerov method is a numerical method for solving one dimensional second order differential equations that do not contain a first order derivative. It is is especially useful in quantum mechanics for determining bound states of a given potential. The methods we present here are based on [25]. The Schrödinger equation is denoted as

$$\left[\frac{\mathrm{d}^2}{\mathrm{d}x^2} + Q(x)\right]\psi(x) = 0, \tag{A.1}$$

where

$$Q(x) = \frac{2\mu}{\hbar^2}\left(E - V(x)\right), \tag{A.2}$$

with $V(x)$ as the potential.

A.1.1 The Numerov Formula

In this section, we perform a discretization of the problem and derive a three-point iteration formula (Numerov formula) for the discretized wavefunction. The x-axis is divided into small intervals of length h starting at the value x_0 and ending at x_N. The discretized wavefunction reads

$$\psi_n = \psi(x_n) = \psi(x_0 + nh). \tag{A.3}$$

Starting at the Taylor expansion

$$\psi(x_n + h) = \sum_k \frac{h^k}{k!}\psi^{(k)}(x_n), \tag{A.4}$$

we obtain

$$\frac{1}{2}\left(\psi_{n+1}\right) = \psi_n + \frac{h^2}{2!}\psi_n^{(2)} + \frac{h^4}{4!}\psi_n^{(4)} + \frac{h^6}{6!}\psi_n^{(6)}. \tag{A.5}$$

We differentiate this equation twice to get

$$\frac{1}{2}\left(\psi_{n+1}^{(2)}\right) = \psi_n^{(2)} + \frac{h^2}{2!}\psi_n^{(4)} + \frac{h^4}{4!}\psi_n^{(6)}. \tag{A.6}$$

Equation (A.6) is multiplied by the factor $h^2/12$ and the result is subtracted from Equation (A.5). This eliminates the fourth order term. Wherever it occurs, we eliminate the second derivative by the original differential equation $\psi_n^{(2)} = -Q_n\psi_n$.

$$\left(1 + \frac{h^2}{12}Q_{n+1}\right)\psi_{n+1} + \left(1 + \frac{h^2}{12}Q_{n-1}\right)\psi_{n-1} - \left(2 - \frac{5h^2}{6}Q_n\right)\psi_n = -\frac{h^6}{240}\psi_n^{(6)}. \tag{A.7}$$

To obtain the Numerov formula, we set the right hand side to zero. The truncation error is of sixth order in h. It is now possible to calculate $\psi_{n+1}$from ψ_n and ψ_{n-1}. Q_n of course is known.

Numerical calculations can be more precise if the values of the functions are not too large compared to one. Therefore it is convenient to calculate the ratio

$$R_n = \frac{\psi_{n+1}}{\psi_n}. \tag{A.8}$$

of the wavefunction at certain x_n and the function of the next step. This quantity is of the order of one in most cases. In the vicinity of nodes, R obviously can have large values, because of division by a small number. Furthermore, the ratio R_n is negative if and only if the wavefunction $\psi(x)$ has a node between x_n and x_{n+1}, which can be used to count the nodes of the wavefunction. Using Equation (A.8) in the Numerov formula Equation (A.7), one can derive a two point iteration formula for R_n:

$$R_n = \left(1 + \frac{h^2}{12}Q_{n+1}\right)^{-1}\left[\left(2 - \frac{5h^2}{6}Q_n\right) - \left(1 + \frac{h^2}{12}Q_{n-1}\right)R_{n-1}^{-1}\right]. \tag{A.9}$$

This formula works for forward iteration, starting at $R_0 = \psi_1/\psi_0$. The quantity Q is known at all points of the x-axis. If the recursion should start at the maximum value of x, namely x_N, another formulation is slightly more convenient. The ratio

$$\tilde{R}_n = \frac{\psi_{n-1}}{\psi_n} \tag{A.10}$$

is defined for that purpose. The corresponding iteration formula runs backwards on the x-axis and the final value is assigned to $\tilde{R}_N$ at x_N, so that we have

$$\tilde{R}_n = \left(1 + \frac{h^2}{12}Q_{n-1}\right)^{-1}\left[\left(2 - \frac{5h^2}{6}Q_n\right) - \left(1 + \frac{h^2}{12}Q_{n+1}\right)R_{n+1}^{-1}\right]. \tag{A.11}$$

A.1.2 Construction of the Wavefunction

In a stable implementation of the Numerov method, the integration of Schrödinger's equation goes up to a matching point r_M from the left side with Numerov-forward R iteration, Equation (A.9), and from the right side with Numerov backward $\tilde{R}$ iteration, Equation (A.11). In the case of the trapped atom-ion potential (Equation (3.41)), the initial condition on the right side is
$\tilde{R}(r_{\max} + h) = \psi(r_{\max})/\psi(r_{\max} + h) = \infty$, and on the left side
$R(r_{\min}) = \psi_{\text{asymp}}(r_{\min} + h)/\psi_{\text{asymp}}(r_{\min})$, using the asymptotic analytic solution of the Schrödinger equation. If an eigenfunction is calculated, left and right side match (see Section 3.4.4). The ratios R_i and $\tilde{R}_i$ are known numerically and are stored. Now the wavefunction is constructed. We start in the middle, at r_M, by setting $\psi(r_M) = 1$. The value is arbitrary, but convenient, because in any case $\psi(r)$ has to be normalized afterwards. From Equation (A.10) we find the formula

$$\psi_i = \frac{\psi_{i-1}}{\tilde{R}_i} \qquad i = M+1, M+2 \ldots, N \;, \tag{A.12}$$

for the right side, and from Equation (A.8) we obtain

$$\psi_i = \frac{\psi_{i+1}}{R_i} \qquad i = M-1, M-2 \ldots, 1 \;, \tag{A.13}$$

for the left side respectively. Since the wavefunction oscillates very fast for small r, the grid is to be adapted to the problem. This requires to derive an interpolation formula and include a changing of the step size during the Numerov iteration, which is done in the following sections. Assuming that the step size is changed in the left side integration at the point r_n, one has to take care of how to iterate over this point. The ratio $R_n = \psi(r_n + h)/\psi(r_n)$ is defined with a certain step size h. Let the step size on the right hand side of r_n be h, and on the left hand side let it be $h' < h$. One runs into trouble if R_n is defined as $R_n = \psi(r_n + h')/\psi(r_n)$ with step size from the left hand side, because the point $r_n + h'$ is not in the grid (compare Figure A.1). Instead, the next value in the grid is $r_{n+1} = r_n + h$. It follows that defining $R_n = \psi(r_n + h)/\psi(r_n)$ avoids problems and one can use Equation (A.13) without restrictions.

An equivalent argument requires $\tilde{R}_n = \psi(r_n - h')/\psi(r_n)$ with the same definitions for h and h' as for the left-side case.

A.1.3 Interpolation Formula

For some problems it is necessary to know the wavefunction at a point that is not on the grid. Halving of the step size during the calculation is one example. For that purpose one needs an interpolation formula that makes it possible to calculate the function on a point between two grid points just as accurately as it is known on the grid points themselves.

The value of the wavefunction at a point x_α that lies between the two grid points x_{i-1} and x_i is to be computed. We have

$$x_i = x_\alpha + (1-\alpha)h \;, \tag{A.14}$$

$$x_{i-1} = x_\alpha - \alpha h \;, \tag{A.15}$$

where $h = x_i - x_{i-1}$ and $0 \leq \alpha \leq 1$. For convenience, we define $\beta = (1-\alpha)$. Making a Taylor expansion of the wavefunction around the point x_α we get

$$\psi_i = \psi_\alpha + (\beta h)\psi'_\alpha + (\beta^2 h^2/2)\psi''_\alpha + (\beta^3 h^3/6)\psi'''_\alpha + O(h^4)\psi^{(\mathrm{IV})}_\alpha \;, \tag{A.16}$$

$$\psi_{i-1} = \psi_\alpha - (\alpha h)\psi'_\alpha + (\alpha^2 h^2/2)\psi''_\alpha - (\alpha^3 h^3/6)\psi'''_\alpha + O(h^4)\psi^{(\mathrm{IV})}_\alpha \;, \tag{A.17}$$

Here $O(h^4)$ represents a term of order h^4. After multiplying Equation (A.16) by β^{-1} and Equation (A.17) by α^{-1}, we sum them and find

$$\beta^{-1}\psi_i + \alpha^{-1}\psi_{i-1} = (\alpha\beta)^{-1}\psi_\alpha + (h^2/2)\psi''_\alpha + (\beta-\alpha)(h^3/6)\psi'''_\alpha + O(h^4)\psi^{(\mathrm{IV})}_\alpha, \tag{A.18}$$

where we made use of the identities

$$\begin{aligned} \alpha + \beta &= 1 \\ \frac{1}{\alpha} + \frac{1}{\beta} &= \frac{\beta+\alpha}{\alpha\beta} = \frac{1}{\alpha\beta} \\ (\alpha^2 - \beta^2) &= (\alpha^2 - (1-\alpha^2)) = (1-2\alpha) = (\beta-\alpha) \;. \end{aligned} \tag{A.19}$$

We differentiate Equations (A.16) and (A.17) twice, add the resulting equations and multiply by $h^2/6$ to obtain

$$(h^2/6)(\psi''_i + \psi''_{i-1}) = (h^2/3)\psi_\alpha + (\beta-\alpha)(h^3/6)\psi'''_\alpha + O(h^4)\psi^{(\mathrm{IV})}_\alpha \;. \tag{A.20}$$

We subtract this from Equation (A.18) to obtain

$$(\beta^{-1}\psi_i + \alpha^{-1}\psi_{i-1}) - h^2/6(\psi''_i + \psi''_{i-1}) = (\alpha\beta)^{-1}\psi_\alpha + (h^2/2 - h^2/3)\psi''_\alpha + O(h^4)\psi^{(\mathrm{IV})}_\alpha. \tag{A.21}$$

We use Schrödinger's equation to eliminate the second order derivative terms. The final expression for the interpolation formula is

$$\psi_\alpha = \left((\alpha\beta)^{-1} + \gamma_\alpha\right)^{-1} \left((\beta^{-1} - \gamma_i)\psi_i + (\alpha^{-1} - \gamma_{i-1})\psi_{i-1}\right) \ , \tag{A.22}$$

with a truncation error of the order h^4, where

$$\gamma_n = -(h^2/6)Q(x_n). \tag{A.23}$$

This formula is as accurate as the renormalized Numerov method, which has a cumulative error of the order of h^4, according to [25]. Thus the function can be evaluated at each point of the x-axis with this precision.

A.1.4 Step Size Doubling

It is possible to double the step size during iteration. The ratio R_n is based on the previous R_{n-i}. The new iteration formula is defined with a double step size $h' = 2 \cdot h$. The iteration starts at the grid point n with the value R_n, which is calculated based on Equation (A.9), such that

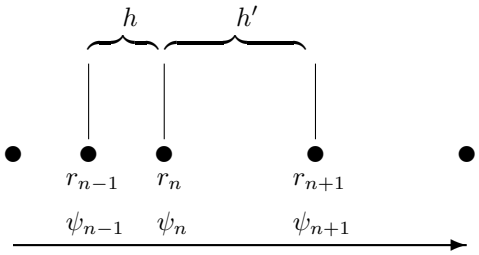

Figure A.1: Doubling of the step size, iterating from the left to the right hand side.

$$R_n = \left(1 + \frac{h'^2}{12}Q_{n+1}\right)^{-1} \left[\left(2 - \frac{5h'^2}{6}Q_n\right) - \left(1 + \frac{h'^2}{12}Q_{n-1}\right) R_0^{-1}\right], \tag{A.24}$$

where

$$R_0 = \frac{\psi_n}{\psi_{n-2}} = \frac{\psi_n}{\psi_{n-1}}\frac{\psi_{n-1}}{\psi_{n-2}} = R(n-1) \cdot R(n-2). \tag{A.25}$$

is obtained for R_0 (see Figure A.1). R_n can directly be calculated from the previous values. It is of course possible to double the step size more than once or increase the step size by an integer factor larger than two.

A.1.5 Step Size Halving

In order to halve the step size one needs to know the wavefunction at a point in between two grid points to find the starting value for a new calculation with a smaller step size. A useful fourth order interpolation formula is derived in

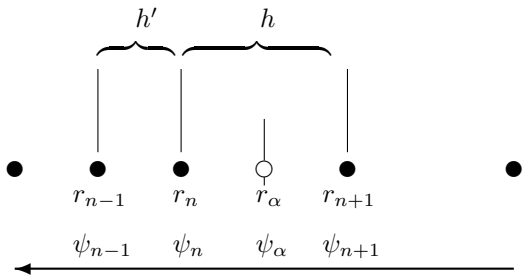

Figure A.2: Halving of the step size, iterating from right to left. The intermediate value of the wavefunction ψ_α is obtained by interpolation.

Section A.1.3. In Figure A.2, step size halving is illustrated for backward iteration of $\tilde{R}_n$. On the right side of x_n, the step size is h; on the left side it is halved to $h' = h/2$. The value of ψ_α in the middle of x_n and x_{n+1} is needed, because the ratio $R_0 = \psi_n/\psi_\alpha$ serves as an initial value for the backwards iteration:

$$\tilde{R}_n = \left(1 + \frac{h'^2}{12}Q_{n-1}\right)^{-1} \left[\left(2 - \frac{5h'^2}{6}Q_n\right) - \left(1 + \frac{h'^2}{12}Q_{n+1}\right)\tilde{R}_0^{-1}\right]. \tag{A.26}$$

Once the initial R_n is calculated, the usual iteration with Equation (A.11) using step size h' is applicable.

The intermediate value of the wavefunction ψ_α is obtained by specifying the interpolation formula (Equation (A.22)) $\alpha = \beta = 1/2$ and $\gamma_i = -(h'^2/6)Q(x_i)$:

$$\psi_\alpha = \left(4 - \frac{h'^2}{6}Q(x_\alpha)\right)^{-1} \left[\left(2 + \frac{h'^2}{6}Q(x_{n+1})\right)\psi_{n+1} + \left(2 + \frac{h'^2}{6}Q(x_n)\right)\psi_n\right]. \tag{A.27}$$

Dividing by ψ_n gives the desired result

$$\frac{\psi_\alpha}{\psi_n} = \left(4 - \frac{h'^2}{6}Q(x_\alpha)\right)^{-1} \left[\left(2 + \frac{h'^2}{6}Q(x_{n+1})\right)\frac{\psi_{n+1}}{\psi_n} + \left(2 + \frac{h'^2}{6}Q(x_n)\right)\right], \tag{A.28}$$

where $\frac{\psi_{n+1}}{\psi_n} = 1/\tilde{R}_{n+1}$ is available from the previous iteration step. The step size halving can be repeated several times. In principle it is also possible to divide h by a number larger than two.

A.2 Numerical Integration

Integrals of the type

$$\int_a^b f(x)\,\mathrm{d}x \tag{A.29}$$

are calculated numerically on a discrete x-axis with the points $x_1 = a, x2, \ldots, x_N = b$. The integrated function must be evaluated at these points. If the points are chosen to be equidistant, the following sum can approximate the integral:

$$\int_{x_1}^{x_N} f(x)\,\mathrm{d}x = h\left[\frac{3}{8}f(x_1) + \frac{7}{8}f(x_2) + \frac{23}{24}f(x_3) + f(x_4) + f(x_5) + \ldots \right.$$
$$\left. + f(x_{N-3}) + \frac{23}{24}f(x_{N-2}) + \frac{7}{8}f(x_{N-1}) + \frac{3}{8}f(x_N)\right] + O(h^4). \tag{A.30}$$

This equation can be found in [26], it is constructed by fitting cubic polynomials through successive groups of four points. The error term is of fourth order in the step size h. We apply this formula to calculate the normalization integral

$$\int_0^\infty |\psi(r)|^2\,\mathrm{d}r \approx \int_{r_{\min}}^{r_{\max}} |\psi(r)|^2\,\mathrm{d}r, \tag{A.31}$$

where the lower limit has to be replaced by $r_{\min}$ since the wave function is singular at $r = 0$. We see that $r_{\min}$ must be small enough to make the error of this truncation small. The wavefunction decays exponentially for $r \to \infty$ and therefore the integral can be truncated at $r_{\max}$. In the normalization integrals we calculate in this thesis, the r axis points are not equidistant, but separated in J sections with different stepsize. This is because the grid is adapted to the period of oscillation of the wavefunctions. In each section the stepsize h_j is kept constant. Consequently, the normalization integral is split into J integrals. Each integral is then calculated with Equation (A.30).

This formula requires at least five points in order to approximate the integral. If ever a part of the x-axis has fewer points, the integral between these points is

approximated with the trapezium rule

$$\int f(x)\mathrm{d}x = \sum_n \frac{f(x_{(n+1)}) + f(x_n)}{2} \cdot h + O(h^2). \tag{A.32}$$

The error term of this formula is of the order of h^2, which is less accurate then Equation (A.30).

A.3 Crank-Nicholson Method

In this section the Crank-Nicholson (or Cayley's) method is introduced in order to numerically solve the time dependent Schrödinger equation. We use this method for time evolution in Section 5 because it is both stable and unitary.

In dimensionless units Schrödinger's equation can be written as

$$i\frac{\mathrm{d}}{\mathrm{d}t}\psi(t) = H(t)\,\psi(t). \tag{A.33}$$

Its formal solution is

$$\psi(t) = e^{-i\int_{t_0}^{t} H(\tau)\,\mathrm{d}\tau}\,\psi(t_0). \tag{A.34}$$

The initial condition $\psi(t_0)$ is given at the time t_0.

Numerically, Equation (A.33) is solved by dividing the time axis between initial time t_0 and final time T into small time intervals of size Δt. Then $\psi(t)$ is propagated step by step, so that at time $t + \Delta t$ we have

$$\psi(t + \Delta t) = e^{-i\int_{t}^{t+\Delta t} H(\tau)\,\mathrm{d}\tau}\,\psi(t). \tag{A.35}$$

First, the integral is approximated as $\int_t^{t+\Delta t} H(\tau)\,\mathrm{d}\tau \approx H(t)\,\Delta t$ to obtain

$$\psi(t + \Delta t) = e^{-iH(t)\,\Delta t}\,\psi(t). \tag{A.36}$$

Written in a basis representation (e.g. harmonic oscillator states, truncated at N), H is an $N \times N$ matrix, and $\psi(t)$ is a vector of N complex numbers. The exponential of a matrix can be calculated, but for large matrices this is very CPU time consuming. A good approximation for the time evolution operator for one time step is the Crank-Nicholson form introduced in [26]:

$$e^{-i\int_{t}^{t+\Delta t} H(\tau)\,\mathrm{d}\tau} \approx \frac{1 - i\,\Delta t\,H(t)}{1 + i\,\Delta t\,H(t)} \tag{A.37}$$

or

$$[1 + i\,\Delta t\,H(t)]\;\psi(t + \Delta t) = [1 - i\,\Delta t\,H(t)]\;\psi(t). \tag{A.38}$$

The method is second order accurate in time (the error term is proportional to $(\Delta t)^2$) and unitary; that is, the normalization of ψ is conserved for each time step.

This equation allows to propagate the wave function $\psi(t)$ one time step forward. Starting at the initial condition at $t = t_0$ and propagating step by step the final wave function $\psi(T)$ can be calculated. The availability of the wavefunction at each time step makes optimal control algorithms possible. One optimal control algorithm is presented in Appendix B and applied in Chapter 5.

A.4 Accuracy of the Crank Nicholson Method, Time Steps and Basis Size

This section is about the numerical accuracy of the time evolution. Two principal error sources exist. On the one hand the accuracy of the Crank-Nicholson method is increased by increasing the number of time steps per process, but this also is more CPU time consuming. On the other hand the more basis functions are used, the smaller is the truncation error, but the computational time increases as well.

Particularly for the optimal control algorithms the computation time must be reasonable small, because many iterations have to be performed. Table A.1 shows that for the adiabatic gate 20000 time steps make sense to achieve an accuracy of 10^{-3}. This corresponds to a time step of the length $\Delta t = 6 \times 10^{-4}$. The Crank-Nicholson method is compared to the Matlab routine *ode45* with a adjusted relative error tolerance of 10^{-5}. The number of basis vectors used has an influence on the computational time as well, so it should be kept low. Table A.2 shows a variation of the basis size for a fast process. According to that a basis size of at least 200 makes sense to achieve an accuracy of 10^{-3}. More than 250 basis states lead to an accuracy of $\approx 10^{-4}$. It is important to note that the process one-channel-phase converges to the value obtained with 1000 basis vectors calculated with the *ode45* method, but it is slightly shifted using the Crank-Nicholson method. This phase shift can possibly be explained by a too small number of Crank-Nicholson-time

time steps C-N	$\frac{\text{FidelityC}-\text{N}}{\text{Fidelity}ode45}$	$\frac{\text{PhaseC}-\text{N}}{\text{Phase}ode45}$	comput. time
2500	0.945644	1.09746	
5000	0.982608	1.02705	
10000	0.990721	1.00682	
20000	0.997411	1.00169	1400sec
30000	0.998830	1.00075	
70000	0.999782	1.00014	5000sec

Table A.1: Test Of the Accuracy of the Crank-Nicholson method by comparing to the Matlab routine *ode45*. The relative error tolerance of ode45 is set to 10^{-5} and the $d(t)$ function depicted in Figure 5.2a is used for both methods. The Number of basis states is 300. The method *ode45* takes 92737 time steps for the time interval of the length of $T = 11.959\hbar/E^*$. One can observe that a accuracy of 10^{-3} is reached with about 20000 time steps for the Crank-Nicholson method. The computation time is measured using two CPUs

steps, but with 10000 time steps the maximal tolerated computational time for reasonably applying optimal control is already reached. The fidelity is equally increasing for *ode45* and Crank-Nicholson method.

Basis Size	time steps	Fidelity *ode45*	phase *ode45*	phase CN
150	18481	0.98886	0.92216	0.92842
200	19155	0.99891	0.99210	0.99553
250	20363	0.99948	0.99779	1.00609
300	21457	0.999472	0.99861	1.00696
1000	38027	1	1	1.00801

Table A.2: Variation of the basis size used for numerical time evolution. The Matlab routine *ode45* is used with a relative error tolerance of 10^{-6}. The simulated process uses the time $T = 3.42$ and is performed for the 00 channel. For the comparison we normalize the calculations to the *ode45* case of 1000 basis vectors. One can observe that between 250 and 300 basis functions the results are accurate up to 10^{-4}. Compared to the Crank-Nicholson method with 10000 time steps, it is remarkable that the phase shows a slight shift which probably is due to a too large time step.

B Optimal Control Techniques

B.1 Introduction to Quantum Optimal Control

In many quantum mechanical systems the dynamics can be controlled by an external field. This control parameter is denominated as $u(t)$ here and is an explicit function of time. The Hamiltonian of the system then depends on the control function. Time evolution of the quantum state $|\psi(t)\rangle$ is given by the Schrödinger equation

$$i\hbar|\dot{\psi}(t)\rangle = H(u(t))\,|\psi(t)\rangle. \tag{B.1}$$

We want to control an ultracold atom-ion collision in this thesis, using trap-induced shape resonances. Here, $u(t)$ is the trap separation $d(t)$, and the Hamiltonian is

$$H = H^{(0)} + \frac{1}{2}\mu\omega^2 d(t)^2 - \mu\omega^2 d(t) z \tag{B.2}$$

as introduced in Equation (2.3). Optimal control theory is about finding the optimal $u(t)$ function that causes the system to evolve from a given initial state $|\psi(t=0)\rangle = |\psi_0\rangle$ to a desired final state $|\psi(T)\rangle = |\psi_f\rangle$ within the fixed time T. The Schrödinger equation for $\psi(t)$ must be fulfilled at all times during the process. The problem can be mathematically formulated by constructing a cost functional (or objective) J that depends on the reached state at the time T. This Functional must be maximized under the constraint of fulfilling Schrödinger's equation.

Such an objective could be the fidelity $|\langle\psi_f|\psi(T)\rangle|^2$, the real part of the overlap $\mathrm{Re}\{\langle\psi_f|\psi(T)\rangle\}$ or the norm of the difference $|\psi(T)\rangle - |\psi_f\rangle$. The most appropriate method must be chosen to fit the specific problem. The optimal solution $u(t)$ can be found by constructing a Lagrange functional L

$$L[\psi,\chi,u] = J[\psi(T)] + 2\mathrm{Re}\left\{\int_0^T \mathrm{d}t\,\left(\langle\dot{\psi}| - \langle\psi|\frac{i}{\hbar}H(u(t))\right)\,|\chi(t)\rangle\right\}. \tag{B.3}$$

that depends on the wavefunction $|\psi(t)\rangle$, the control $u(t)$ and an auxiliary state $|\chi(t)\rangle$. The functions that make J extremal under the constraint of fulfilling the Schrödinger equation have the property that the first derivatives of L with respect to ψ, χ and u vanish. Technically, the variation $\delta_{f_i} F$ of the functional $F[f_i]$ in the argument function f_i replaces the derivative ´$\partial F/\partial f_i$'. Optimal control techniques are further detailed in [36],[37] and [38]. In particular one can prove the existence of an optimal solution.

B.2 Basic Equations

In this section we derive the basic equations for the optimal solutions $\psi(t)$, $\chi(t)$ and $u(t)$ by a variation of the Lagrange functional L. The variation of a functional F is

$$\delta_f F[f] = F[f + \delta f] - F[f]. \tag{B.4}$$

Here, only linear terms in δf must be taken into account. Equating each derivative(variation) to zero leads to equations for the optimal solution.

Variation of $|\psi\rangle$

Taking the variation of L with respect to ψ, we have

$$\begin{aligned}
&\delta_\psi L[\psi, \chi, u] \\
&\quad = L[\psi + \delta\psi, \chi, u] - L[\psi, \chi, u] && \text{(B.5)} \\
&\quad = \delta_{\psi(T)} J[\psi(T)] - 2\mathrm{Re}\left\{ \int_0^T \mathrm{d}t \, \langle\chi(t)| \left(\frac{i}{\hbar} H(u(t)) + \frac{\mathrm{d}}{\mathrm{d}t} \right) |\psi(t) + \delta\psi(t)\rangle \right\} \\
&\qquad + 2\mathrm{Re}\left\{ \int_0^T \mathrm{d}t \langle\chi(t)| \left(\frac{i}{\hbar} H(u(t)) + \frac{\mathrm{d}}{\mathrm{d}t} \right) |\psi(t)\rangle \right\} && \text{(B.6)} \\
&\quad = \delta_{\psi(T)} J[\psi(T)] \\
&\qquad - 2\mathrm{Re}\left\{ \int_0^T \mathrm{d}t \, \left(\langle\chi(t)| \frac{i}{\hbar} H(u(t)) \, |\delta\psi(t)\rangle + \langle\chi(t)|\dot{\delta\psi}(t)\rangle \right) \right\} && \text{(B.7)}
\end{aligned}$$

$$= \delta_{\psi(T)} J[\psi(T)] - 2\mathrm{Re}\left\{ \int_0^T \mathrm{d}t \, \langle \chi(t)| \frac{i}{\hbar} H(u(t)) \, |\delta\psi(t)\rangle + \langle \chi(t)|\delta\psi(t)\rangle \Big|_0^T - \int_0^T \mathrm{d}t \langle \dot{\chi}(t)|\delta\psi(t)\rangle \right\} \tag{B.8}$$

$$= \delta_{\psi(T)} J[\psi(T)] - 2\mathrm{Re}\left\{ \langle \chi(T)|\delta\psi(T)\rangle + \int_0^T \mathrm{d}t \left(\langle \chi(t)| \frac{i}{\hbar} H(u(t)) - \langle \dot{\chi}(t)| \right) |\delta\psi(t)\rangle \right\}. \tag{B.9}$$

In the last step, after the integration by parts, we used the fact that the variation of $|\psi\rangle$ should not affect the initial state, i.e. $|\delta\psi(0)\rangle = 0$. Because the variation $|\delta\psi(t)\rangle$ is arbitrary, $\delta_\psi L$ in the last line of Equation (B.9) can only vanish if the integrand vanishes. That means $|\chi(t)\rangle$ fulfills the Schrödinger equation

$$i\hbar|\dot{\chi}(t)\rangle = H(u(t)) \, |\chi(t)\rangle \tag{B.10}$$

for all times, with the end-condition

$$0 = \delta_{\psi(T)} J[\psi(T)] - 2\mathrm{Re}\left\{ \langle \chi(T)|\delta\psi(T)\rangle \right\}. \tag{B.11}$$

The condition of Equation (B.11) in the following is specified for two examples for when J is the fidelity, and when J is the real part of the overlap. For the application in this thesis, the choice $J = 2\mathrm{Re}\langle\psi_f|\psi(T)\rangle$ is more relevant, since for the phase gate we need phase information, which is lost by taking the absolute value of the fidelity. The fidelity can be used for other applications and is found as an objective in literature, and so we will derive the equations for both cases.

a) Fidelity: $J[\psi(T)] = |\langle\psi_f|\psi(T)\rangle|^2$ substituted in Equation (B.11) yields

$$0 = J[\psi(T) + \delta\psi(T)] - J[\psi(T)] - 2\mathrm{Re}\left\{ \langle \chi(T)|\delta\psi(T)\rangle \right\} \tag{B.12}$$

$$= \langle\psi_f| \left(|\psi(T)\rangle + |\delta\psi(T)\rangle \right) \left(\langle\psi(T)| + \langle\delta\psi(T)| \right) |\psi_f\rangle - \langle\psi_f|\psi(T)\rangle\langle\psi(T)|\psi_f\rangle - 2\mathrm{Re}\left\{ \langle \chi(T)|\delta\psi(T)\rangle \right\} \tag{B.13}$$

$$= \left(\langle\psi_f|\psi(T)\rangle + \langle\psi_f|\delta\psi(T)\rangle \right) + \left(\langle\psi(T)|\psi_f\rangle + \langle\delta\psi(T)|\psi_f\rangle \right) - \langle\psi_f|\psi(T)\rangle\langle\psi(T)|\psi_f\rangle - 2\mathrm{Re}\left\{ \langle \chi(T)|\delta\psi(T)\rangle \right\} \tag{B.14}$$

$$= \langle\psi_f|\psi(T)\rangle\langle|\delta\psi(T)|\psi_f\rangle + \langle\psi_f|\delta\psi(T)\rangle\langle\psi(T)|\psi_f\rangle + \underline{\langle\delta\psi(T)|\psi_f\rangle\langle\delta\psi(T)|\psi_f\rangle} - 2\mathrm{Re}\left\{\langle\chi(T)|\delta\psi(T)\rangle\right\} \tag{B.15}$$

Here, we neglect the marked term, because it is second order in $\delta\psi(T)$. We arrive at

$$0 = 2\mathrm{Re}\left\{\langle\psi(T)|\psi_f\rangle\langle\psi_f|\delta\psi(T)\rangle\right\} - 2\mathrm{Re}\left\{\langle\chi(T)|\delta\psi(T)\rangle\right\} \tag{B.16}$$

For arbitrary $\delta\psi(T)$, we find an end value condition for $\chi(T)$

$$0 = \langle\psi_f|\langle\psi(T)|\psi_f\rangle - \langle\chi(T)|, \tag{B.17}$$

or

$$|\chi(T)\rangle = \langle\psi_f|\psi(T)\rangle|\psi_f\rangle, \tag{B.18}$$

which can be interpreted as the part of $|\psi\rangle$ that reached $|\psi_f\rangle$.

b) Real part of the overlap: $J[\psi(T)] = 2\mathrm{Re}\{\langle\psi_f|\psi(T)\rangle\}$ substituted in Equation B.11 yields:

$$\begin{aligned} 0 &= J[\psi(T) + \delta\psi(T)] - J[\psi(T)] - 2\mathrm{Re}\left\{\langle\chi(T)|\delta\psi(T)\rangle\right\} \\ &= 2\mathrm{Re}\left\{\langle\psi_f|\delta\psi(T)\rangle - \langle\chi(T)|\delta\psi(T)\rangle\right\}. \end{aligned} \tag{B.19}$$

For arbitrary small variation $\delta\psi(T)$ the end value condition in this case reads

$$|\chi(T)\rangle = |\psi_f\rangle. \tag{B.20}$$

The end value condition for $|\chi\rangle$ is the objective state.

Variation of $|\chi\rangle$

The calculation of $\delta_\chi L$ is similar to $\delta_\psi L$, only more straightforward. We find that the variation of χ yields the constraint, as expected for the Lagrange-multiplier-like method, $\psi(t)$ must satisfy the Schrödinger equation

$$i\hbar|\dot{\psi}(t)\rangle = H(u(t))\,|\psi(t)\rangle, \tag{B.21}$$

for all times t, with the initial condition

$$|\psi(0)\rangle = |\psi_0\rangle. \tag{B.22}$$

Variation of u(t)

The variation of L with respect to the control $u(t)$ yields:

$$\begin{aligned}\delta_u L[\psi,\chi,u] &= L[\psi,\chi,u+\delta u] - L[\psi,\chi,u] \\ &= 2\mathrm{Re}\left\{\int_0^T \mathrm{d}t\langle\chi|\,\frac{i}{\hbar}\frac{\partial H}{\partial u}(t)\,\delta u(t)\,|\psi(t)\rangle\right\}.\end{aligned} \tag{B.23}$$

For arbitrary variation $\delta u(t)$

$$0 = -2\mathrm{Im}\left\{\langle\chi|\,\frac{\partial H}{\hbar\partial u}(t)\,|\psi(t)\rangle\right\} \tag{B.24}$$

must hold for all times. The derivative $\partial H/\partial u$ is an operator. It sometimes is easy to determine, e.g. in the linear case $H(u(t)) = H_0 + u(t)H_1$, the derivative is H_1. In the atom-ion control of Chapter 5 the derivative reads

$$\left(\frac{\partial H}{\partial d}\right)_{\mathrm{ai}} = \mu\omega^2 d(t) - \mu\omega^2 z. \tag{B.25}$$

Summary

We summarize the equations for the state and the optimal control functions for the objective of maximizing $J = 2\mathrm{Re}\,\{\langle\psi_f|\psi(T)\rangle\}$.

a) The equation of motion for $\psi(t)$ is

$$i\hbar|\dot{\psi}(t)\rangle = H(u(t))\,|\psi(t)\rangle, \tag{B.26}$$

with the initial condition

$$|\psi(0)\rangle = |\psi_0\rangle. \tag{B.27}$$

b) the equation of motion for $\chi(t)$ is

$$i\hbar|\dot{\chi}(t)\rangle = H(u(t))\,|\chi(t)\rangle, \tag{B.28}$$

with end-value condition

$$|\chi(T)\rangle = |\psi_f\rangle. \tag{B.29}$$

c) The end-condition for $u(t)$ is

$$0 = -2\mathrm{Im}\,\{K(u(t))\}, \tag{B.30}$$

with

$$K(u(t)) = \langle\chi(t)|\,\frac{\partial H}{\hbar\,\partial u}(t)\,|\psi(t)\rangle. \tag{B.31}$$

B.2.1 Control of more than one State

The calculations above are valid for the case of one wavefunction to be controlled by one control function. The atom-ion quantum gate described in Chapter 5 requires the simultaneous control of four isolated qubit channels. For that purpose we extend the equations to a set of wavefunctions $\{\psi^A\}$, $A \in \{1, 2, ..\}$ and a set of control functions $\{u_j(t)\}$ $j \in \{1, 2, ..\}$. Time evolution is governed by a Schrödinger equation for each $\psi^A(t)$ with Hamilton operators $\{H^A\}$.

We formulated an objective as the sum of the single objectives.

$$J[\{\psi_A(T)\}] = \sum_A J_A[\psi_A(T)] \tag{B.32}$$

The Lagrange functional has the form

$$\begin{aligned} &L[\{\psi^A\}, \{\chi^A\}, \{u_j\}] = \\ &J[\{\psi_A(T)\}] + 2\mathrm{Re}\left\{\sum_A \int_0^T \mathrm{d}t \left(\langle\dot{\psi^A}| - \frac{i}{\hbar}\langle\psi|H^A\left(\{u_j(t)\}\right)\right)|\chi^A(t)\rangle\right\}. \end{aligned} \tag{B.33}$$

For specific objective $J^A[\psi^A(T)] = 2\mathrm{Re}\left\{\langle\psi_f^A|\psi^A(T)\rangle\right\}$ the resulting equations are summarized below.

a) Equations of motion for the $\{\psi^A(t)\}$ are:

$$i\hbar|\dot{\psi}^A(t)\rangle = H^A(\{u_j(t)\})\,|\psi^A(t)\rangle, \qquad A \in \{1, 2, ..\} \tag{B.34}$$

with the initial conditions

$$|\psi^A(0)\rangle = |\psi_0^A\rangle. \tag{B.35}$$

b) Equations of motion for $\{\chi^A(t)\}$ are:

$$i\hbar|\dot{\chi}^A(t)\rangle = H^A(\{u_j(t)\})\,|\chi^A(t)\rangle, \qquad A \in \{1, 2, ..\} \tag{B.36}$$

with end-value conditions

$$|\chi^A(T)\rangle = |\psi_f^A\rangle.. \tag{B.37}$$

c) Equations for $\{u_j(t)\}$:

$$0 = -2\mathrm{Im}\left\{\sum_A K_j^A(\{u_j(t)\})\right\}, \qquad j \in \{1, 2, ..\}, \tag{B.38}$$

where

$$K_j^A(\{u_j(t)\}) = \langle\chi^A(t)| \frac{\partial H^A(\{u_j(t)\})}{\hbar\, \partial u_j}(t) |\psi^A(t)\rangle. \tag{B.39}$$

B.3 Iterative Algorithm

The set of Equations (B.34, B.35, B.36, B.37, B.38, B.39) for the optimal solutions provides the basis for an an iterative algorithm for finding the optimal control functions $\{u_j(t)\}$. We solve Equations (B.34) and (B.36) numerically by discretizing the time axis with time step Δt and by using the Crank-Nicholson method (see Section A.3). We start with an initial guess for the control functions $\{u_j^{(0)}(t)\}$. In each iteration the controls are updated from $\{u_j^{(n)}(t)\}$ to $\{u_j^{(n+1)}(t)\}$ with the result that the objective is increased. The algorithm we use here is called intermediate feedback control (see [39]). The algorithm is initialized with a forwards propagation of the $\{|\psi^A(t)\rangle\}$ with the initial conditions from Equation (B.35) by using the initial guess controls $\{u_j^{(0)}(t)\}$.

At this point an iterative procedure can start. At the n-th iteration, the current controls are $\{u_j^{(n)}(t)\}$. The $\{|\chi^A(t)\rangle\}$ are propagated from $t = T$ to $t = 0$ backwards in time with the final conditions from Equation (B.37). Given the solutions $|\chi^A(0)\rangle$, the states $|\chi^A(t)\rangle$ and $|\psi^A(t)\rangle$ are now again evolved forwards in time with the initial conditions from Equation (B.35). For $|\chi^A(t)\rangle$, the old controls $\{u_j^{(n)}(t)\}$ are used. During each time step the controls are updated according to

$$u_j^{(n+1)}(t) = u_j^{(n)}(t) + \frac{2}{\lambda(t)}\mathrm{Im}\left\{\sum_A K_j^A(\{u_j^{(n)}(t)\})\right\}, \qquad j \in \{1, 2, ..\}. \tag{B.40}$$

These new controls are used to evolve $|\psi^A(t)\rangle$ forwards in time. The weight $\lambda(t)$ fixes the initial and final values of $\{u_j(t)\}$ and adjusts the magnitude of the update. Once the final time is reached and the update of the controls is complete, $|\psi(T)\rangle$ is calculated and the next iteration step can start. We stop the procedure as soon as a satisfying objective is reached.

K_j^A can be interpreted as the gradient of the objective with respect to the control functions. The expectation value is calculated with the backwards propagated $|\chi^A\rangle$, which represents the goal, and the forwards propagated $|\psi^A\rangle$ produced by the current control. Therefore K_j^A gives a direction in which the control must be updated to get closer to the objective. After the update, $\psi^A\rangle$ is propagated with the new controls.

Since the parameter space is huge, it can easily happen that a local extremal value is found by the algorithm. If the objective converges, but not to the optimal solution, a different initial guess may have better success. Another important issue is the magnitude of the control updates in Equation (B.40). The weight $\lambda(t)$ assures that the boundary conditions are fixed, but can also be used to adjust this magnitude. If λ is too big, the updates are small and convergence is slow. On the other hand, if λ is too small, the algorithm can miss the optimal solution because of too large an update, and the convergence is lost. This is schematically illustrated in Figure B.1.

In one of our optimization programs of the atom-ion gate, $\lambda(t)$ is exponentially increasing at the final and the initial time to values of the order of 10^{13}, and thereby fixes the initial and final values of the control function. For other times we require values of the order of 10^4. The control function takes values of the order of one in the dimensionless coordinates used, while the Hamiltonian can take values of the order of 10^2 to 10^3 in our example. The function $\lambda(t)$ regulates the updates to be smaller than one in this case.

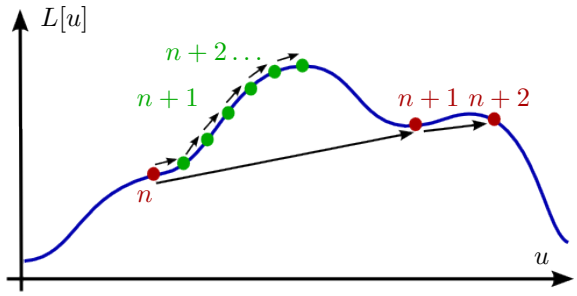

Figure B.1: Schematic depiction of updating the optimal control function in order to reach the maximum value of the cost functional. Steps that are too large can cause errors. Smaller steps can be more successful, but are also more time consuming.

Bibliography

[1] N. Schlosser, G. Reymond, I.E. Protsenko, and P. Grangier. Sub-poissonian loading of single atoms in a microscopic dipole trap. *Nature*, 411:1024, 2001.

[2] M. Greiner, O. Mandel, T. Esslinger, T.W. Hänsch, and I. Bloch. Quantum phase transition from a superfluid to a Mott insulator in a gas of ultracold atoms. *Nature*, 415:39, 2002.

[3] R. Folman, P. Krueger, J. Schmiedmayer, J. Denschlag, and C. Henkel. Microscopic atom optics: from wires to an atom chip. *Adv. At. Mol. Opt. Phys.*, 48:263, 2002.

[4] R. Dumke, M. Volk, T. Müther, F. B. J. Buchkremer, G. Birkl, and W. Ertmer. Micro-optical realization of arrays of selectively addressable dipole traps: A scalable configuration for quantum computation with atomic qubits. *Phys. Rev. Lett.*, 89(9):097903, Aug 2002.

[5] D. Leibfried, R. Blatt, C. Monroe, and D. Wineland. Quantum dynamics of single trapped ions. *Rev. Mod. Phys.*, 75(1):281–324, Mar 2003.

[6] Winthrop W. Smith and Jian Makarov, Oleg P.and Lin. Cold ion-neutral collision in a hybrid trap. *Journal of Modern Optics*, 52:2253.

[7] Zbigniew Idziaszek, Andrea Simoni, Paul S. Julienne, and Tommaso Calarco. Multichannel quantum-defect theory for ultracold atom-ion collisions. *submitted, arXiv:0806.4002v1*, Nov 2008.

[8] Fedja Oručević Andrew T. Grier, Marko Cetina and Vladan Vuletić. Observation of cold charge-exchange collisions between trapped ions and trapped atoms. *arXiv:0808.3620v1 [physics.atom-ph]*, Aug 2008.

[9] S. Schmid, A. Härter, J. Hecker Denschlag, and A. Frisch. Project BaRbI at the Institut für Experimentalphysik, University of Innsbruck.

[10] Zbigniew Idziaszek, Tommaso Calarco, and Peter Zoller. Controlled collisions of a single atom and an ion guided by movable trapping potentials. *Physical Review A (Atomic, Molecular, and Optical Physics)*, 76(3):033409, 2007.

[11] Z. Idziaszek, T. Calarco, and P. Zoller. *not yet published.*

[12] Oleg P. Makarov, R. Côté, H. Michels, and W. W. Smith. Radiative charge-transfer lifetime of the excited state of $(NaCa)^+$. *Phys. Rev. A*, 67(4):042705, Apr 2003.

[13] K. Mølhave and M. Drewsen. Formation of translationally cold MgH^+ and MgD^+ molecules in an ion trap. *Phys. Rev. A*, 62(1):011401, Jun 2000.

[14] C. Monroe, D. M. Meekhof, B. E. King, W. M. Itano, and D. J. Wineland. Demonstration of a fundamental quantum logic gate. *Phys. Rev. Lett.*, 75(25):4714–4717, Dec 1995.

[15] C. Cohen-Tannoudji, B. Diu, and F. Laloe. *Quantenmechanik, Tl.1 und Tl.2.* de Gruyter, 2., durchges. u. verb. edition, 1999.

[16] Adriano Barenco, David Deutsch, Artur Ekert, and Richard Jozsa. Conditional quantum dynamics and logic gates. *Phys. Rev. Lett.*, 74(20):4083–4086, May 1995.

[17] D. Jaksch, C. Bruder, J. I. Cirac, C. W. Gardiner, and P. Zoller. Cold bosonic atoms in optical lattices. *Phys. Rev. Lett.*, 81(15):3108–3111, Oct 1998.

[18] MichałKrych. Private communication.

[19] Thorsten Köhler, Krzysztof Góral, and Paul S. Julienne. Production of cold molecules via magnetically tunable Feshbach resonances. *Reviews of Modern Physics*, 78(4):1311, 2006.

[20] J. J. Sakurai. *Modern Quantum Mechanics (2nd Edition).* Addison Wesley, January.

[21] M. Born and V. Fock. Beweis des Adiabatensatzes. page 165, August 1928.

[22] Kurt Wittig. The Landau-Zener formula. *Journal of physical Chemestry B*, 109:8428, 2005.

[23] Frederick H. Mies. A multichannel quantum defect analysis of diatomic predissociation and inelastic atomic scattering. *J.Chem.Phys*, 80(6), March 1984.

[24] B Gao, E. Tiesinga, C.J. Williams, and P.S. Julienne. Multichannel quantum-defect theory for slow atomic collisions. *Phys. Rev. A*, 72:042719, 2005.

[25] B. R. Johnson. New numerical methods applied to solving the one-dimensional eigenvalue problem. *The Journal of Chemical Physics*, 67(9):4086–4093, 1977.

[26] William Press, Saul Teukolsky, William Vetterling, and Brian Flannery. *Numerical Recipes in C*. Cambridge University Press, Cambridge, UK, 2nd edition, 1992.

[27] I.N. Bronstein, K.A. Semendjajew, G. Musiol, and H. Mühlig. *Taschenbuch der Mathematik*. Verlag Harri Deutsch, Frankfurt am Main,Germany, 1st edition, 1993.

[28] O. H. Arroe. Hyperfine structure and isotope shift in Barium. *Phys. Rev.*, 79(5):836–838, Sep 1950.

[29] Guido Burkard, Daniel Loss, and David P. DiVincenzo. Coupled quantum dots as quantum gates. *Phys. Rev. B*, 59(3):2070–2078, Jan 1999.

[30] T. Calarco, J. I. Cirac, and P. Zoller. Entangling ions in arrays of microscopic traps. *Phys. Rev. A*, 63(6):062304, May 2001.

[31] T. Calarco, E. A. Hinds, D. Jaksch, J. Schmiedmayer, J. I. Cirac, and P. Zoller. Quantum gates with neutral atoms: Controlling collisional interactions in time-dependent traps. *Phys. Rev. A*, 61(2):022304, Jan 2000.

[32] A. Couvert, T. Kawalec, G. Reinaudi, and D. Guéry-Odelin. Optimal transport of ultracold atoms in the non-adiabatic regime. *EPL (Europhysics Letters)*, 83(1):13001 (4pp), 2008.

[33] G Huber, T Deuschle, W Schnitzler, R Reichle, K Singer, and F Schmidt-Kaler. Transport of ions in a segmented linear Paul trap in printed-circuit-board technology. *New Journal of Physics*, 10(1):013004 (15pp), 2008.

[34] Michael Murphy, Liang Jiang, Navin Khaneja, and Tommaso Calarco. arxiv:0810.2491v2 [quant-ph].

[35] Andrew M. Steane. Overhead and noise threshold of fault-tolerant quantum error correction. *Phys. Rev. A*, 68(4):042322, Oct 2003.

[36] Anthony P. Peirce, Mohammed A. Dahleh, and Herschel Rabitz. Optimal control of quantum-mechanical systems: Existence, numerical approximation, and applications. *Phys. Rev. A*, 37(12):4950–4964, Jun 1988.

[37] Shlomo E. Sklarz and David J. Tannor. Loading a Bose-Einstein condensate onto an optical lattice: An application of optimal control theory to the nonlinear Schrödinger equation. *Phys. Rev. A*, 66(5):053619, Nov 2002.

[38] Alfio Borzì, Georg Stadler, and Ulrich Hohenester. Optimal quantum control in nanostructures: Theory and application to a generic three-level system. *Phys. Rev. A*, 66(5):053811, Nov 2002.

[39] T. Calarco, U. Dorner, P. S. Julienne, C. J. Williams, and P. Zoller. Quantum computations with atoms in optical lattices: Marker qubits and molecular interactions. *Phys. Rev. A*, 70(1):012306, Jul 2004.